Lehrstuhl für Luftfahrtsysteme
Technische Universität München

Development of a Parametric Aircraft Design Tool for Design Iterations of a High-Capacity Turboprop Transport Aircraft

Martin Enno Kügler
LS-MA 14/10

LS-SA/DA lfd Nr.	Vertraulichkeit
LS-MA 14/10	Öffentlich
Titel (und Untertitel) Development of a Parametric Aircraft Design Tool for Design Iterations of a High-Capacity Turboprop Transport Aircraft	Autor Martin Enno Kügler Betreuer 1 Randt Technische Universität München Betreuer 2

Daten zur Abgabe und Korrektur der Studienarbeit:

22.09.2014	07.10.2014	21.10.2014
Abgabe der Erstfassung (Datum)	Rückgabe der korrigierten Erstfassung (Datum)	Abgabe der Endversion (Datum)

Bestätigung der Einreichung der abgeschlossenen Studienarbeit durch den Betreuer:

Ort, Datum	Unterschrift des Betreuers am LLS (Randt)

Anmerkungen:

Danksagung

Zunächst bedanke ich mich bei Prof. Dr. Mirko Hornung und seinem Lehrstuhl für Luftfahrtsysteme für die Voraussetzungen zur Masterarbeit und die angenehme und produktive Atmosphäre, die ich während meiner Tätigkeit miterleben durfte.

Mein besonderer Dank gilt meinem Betreuer Dipl.-Ing. Niclas P. Randt für die interessante Aufgabenstellung, für die Unterstützung sowie für die konstruktiven Diskussionen und die gute Betreuung während meiner Arbeit.
Dieser Dank gilt in gleicher Weise Dipl.-Ing. Thomas Lampl, der mich insbesondere in der Anfangsphase der Arbeit unterstützt hat.

Bei allen Studierenden, die während meiner Arbeit ebenfalls im Studentenraum des Lehrstuhls für Luftfahrtsysteme tätig waren, insbesondere bei Dipl.-Ing. Adam Latzke, Lennart Wache, B.Sc. und Iñaki González, bedanke ich mich herzlich für die angenehme Zusammenarbeit, die Unterstützung sowie für die interessanten und lehrreichen Diskussionen.

Des Weiteren bedanke ich mich bei Dipl.-Ing. Jens Feger für die Hilfe bei Schwierigkeiten und Problemen mit der Rechnerumgebung am Lehrstuhl für Luftfahrtsysteme.

Für sein Interesse an meiner Arbeit und insbesondere für seine Ratschläge und Hinweise zur Modellierung von Turboprop-Triebwerken im Flugzeugentwurf sowie für die Zurverfügungstellung von Triebwerksdaten danke ich Dr.-Ing. Andreas Hupfer vom Lehrstuhl für Flugantriebe der Technischen Universität München.

Kurzzusammenfassung

Aufgrund des stetig steigenden Luftverkehrsaufkommens hat sich die Abwicklung von Flugbewegungen, sowohl am Boden als auch in der Luft, in einigen Regionen zu einem Kapazitätsengpass entwickelt, der zukünftiges Wachstum der zivilen Verkehrsluftfahrt zunehmend gefährdet. Um diesem Problem zu begegnen, wurde am Lehrstuhl für Luftfahrtsysteme der Technischen Universität München ein Turboprop-getriebenes Großraumflugzeug für den Einsatz auf Kurz- und Mittelstrecken entwickelt.

Im Rahmen dieser Arbeit wird ein Flugzeugentwurfsprogramm für die Untersuchung und Weiterentwicklung dieses Flugzeugkonzepts erarbeitet. Das Programm beinhaltet Berechnungsmodule für Aerodynamik, Massenabschätzung und Triebwerksmodellierung des untersuchten Flugzeugkonzepts. Unter Verwendung der Ergebnisse dieser Module werden weiterhin Analysen zu Flug- und Missionsleistungen durchgeführt.

Mit den Ergebnissen zum Turboprop-getriebenen Großraumflugzeug für Kurz- / Mittelstrecken werden Vorentwurfsdaten aktualisiert. Durch den Vergleich der Ergebnisse mit Zulassungsvorschriften und Entwicklungszielen werden kritische Entwurfsaspekte identifiziert. Es zeigt sich, dass die Basisversion des Flugzeugkonzepts nicht zulassungsfähig ist, da eine Anforderung an die Steigleistung beim Start mit einem ausgefallenen Triebwerk nicht erfüllt ist.

Mit einem Fokus auf der Triebwerkscharakteristik und den Missionsleistung wird das Flugzeugkonzept in einem iterativen Designprozess unter Verwendung des Flugzeugentwurfsprogramms weiterentwickelt. Das überarbeitete Konzept erfüllt alle Zulassungs- und Entwurfsanforderungen und weist außerdem einen niedrigeren Treibstoffverbrauch auf als die heutige Luftverkehrsflotte. Dieser Vorteil ist dabei alleine auf den spezifischen Entwurf des Großraumflugzeugs für den Einsatz auf Kurz- und Mittelstrecken zurückzuführen. Zusätzliches Potential besteht durch technologische Innovationen wie effizientere Triebwerke, verbesserte Aerodynamik oder leichtere Werkstoffe.

Abstract

In some regions, congestion of both air and ground capacities for handling aircraft movements increasingly constrains the future growth of the air transport industry. In order to overcome this bottleneck, a turboprop-powered high-capacity aircraft concept has been developed at the Institute of Aircraft Design of the Technische Universität München for operation on short- to medium-range routes.

Within the scope of this work, a parametric aircraft design tool is developed for the recalculation and redesign of this concept. The tool contains calculation modules for predicting aerodynamic characteristics, masses, and propulsion properties. By combining the results of these modules, the tool calculates performance characteristics of the aircraft concept with regard to operating limitations and mission performance.

With the obtained results, data from the conceptual design phase of the high-capacity short-/medium-range concept is updated. Critical aspects and design drivers of the concept are identified by comparing the results to design requirements and certification constraints. It is found that the baseline version of the aircraft cannot be certified, as it fails a climb requirement for take-off with one engine inoperative.

In an iterative process the baseline concept is redesigned with the aircraft design tool, at which a focus lies on propulsion characteristics and mission performance. The revised concept meets all certification constraints and design requirements. Moreover, it provides superior fuel efficiency compared to the current airline fleet. This advantage arises solely from the specific design as a high-capacity aircraft for short- to medium-range operations. Technological innovations such as more fuel-efficient engines, improved aerodynamics or lightweight structures remain complementary.

Contents

List of Figures

List of Tables

Nomenclature

Coefficients and Parameters

A	Aspect ratio
A_f	Airfoil factor
a	Speed of sound, coefficient of the engine power model
$\overline{a}$	Average deceleration during braking after touchdown
B_p	Number of propeller blades
C_D	Drag coefficient of the whole aircraft
C_d	Drag coefficient of the airfoil
C_{Di}	Drag-due-to-lift coefficient
C_{D0}	Zero-lift drag coefficient
$C_{D,L\&P}$	Drag coefficient of leakages and protuberances
$C_{D,misc}$	Drag coefficient of miscellaneous special features, e.g., an upswept aft fuselage
C_f	Flat-plate skin-friction coefficient
C_{fe}	Equivalent skin-friction coefficient
C_L	Lift coefficient of the whole aircraft
C_l	Lift coefficient of the airfoil
$C_{L\alpha}$	Slope of the lift curve of the whole aircraft
$C_{l\alpha}$	Slope of the lift curve of the airfoil
$C_{L\,max}$	Maximum lift coefficient of the whole aircraft

$C_{l\,max}$	Maximum lift coefficient of the airfoil
C_m	Pitching-moment coefficient of the airfoil
c	Length of the chord of wing, horizontal or vertical tail
c_{lam}	Chord fraction with laminar flow
c_{flap}/c	Flap chord to wing chord length
c'/c	Wing chord with extended high-lift devices to clean chord length ratio
D	Drag force of the whole aircraft
D_P	Propeller diameter
d_{eng}	Maximum diameter of the engine nacelle
d_h	Maximum horizontal diameter of the fuselage
d_v	Maximum vertical diameter of the fuselage
e	Oswald span-efficiency factor
F	Fuselage-lift factor
F_{flap}	Zero-lift flap drag increment factor
FF_c	Component form factor
f	Geometric factor
g	Gravitational acceleration
h	Height of the aircraft above ground
h_{TR}	Height at the end of the transition arc
J	Propeller advance ratio
K	Drag-due-to-lift factor
K_A	Take-off acceleration parameter
K_T	Take-off acceleration parameter
K_{UC}	Undercarriage coefficient
k	Skin roughness value
k_{flap}	Flap drag-due-to-lift increment factor
$k_{0\ldots5}$	Coefficients of the specific fuel consumption model of the engine
L	Lift force of the whole aircraft
L/D	Aerodynamic efficiency, i.e., lift-to-drag ratio
l	Characteristic length

l_{eng}	Length of the engine nacelle
l_f	Fuselage length
M	Mach number
M_{DD}	Drag-divergent Mach number
M_{final}	Mach number at the end of acceleration
M_{tip}	Mach number of the propeller blade tip
$\dot{m}_{fuel}$	Fuel mass flow rate
n	Rotational speed of the propeller
n_{eng}	Number of engines
P	Power
P_{av}	Available power
P_{eq}	Equivalent power
P_{MSL}	Static power rating
q	Dynamic pressure
R	Range
R_F	Radius of the flare arc
R_{TR}	Radius of the transition arc
R_W	Ratio of the wetted area to the reference area of the wing
Re	Reynolds number
S	Grade of leading-edge suction
S_{AS}	Accelerate-stop distance
S_a	Approach distance
S_B	Braking distance
S_C	Climb distance
$S_{exposed}$	Exposed wing planform area, i.e., not covered by fuselage
S_F	Flare distance
$S_{flapped}$	Part of the wing planform area affected by flaps
S_{FR}	Free roll distance
S_G	Ground roll distance

S_{LDG}	Total landing distance
$S_{nacelle}$	Maximum cross section of the engine nacelle
S_R	Rotation distance
S_{ref}	Wing reference area
$S_{slipstream}$	Wing planform area in propeller slipstream
S_{TO}	Total take-off distance
S_{TR}	Transition to climb distance
S_{wet}	Wetted area
T	Thrust
T_S	Static thrust
T_f	Aircraft type factor
t/c	Thickness to chord ratio of wing, horizontal or vertical tail
$(t/c)_P$	Thickness to chord ratio of the propeller blades
u	Upsweep angle of fuselage centerline
V	Velocity
V_a	Velocity during approach
V_{CL}	Velocity during climb
V_F	Velocity on flare arc
V_i	Initial velocity at the beginning of take-off acceleration
V_R	Velocity of rotation
V_S	Velocity of stall
V_{TD}	Velocity at touchdown
V_{TR}	Velocity on transition arc
V_2	Velocity in second segment climb
W	Weight, i.e., mass times gravitational acceleration
$(x/c)_{max\ thickness}$	Relative chordwise position of the maximum thickness of the airfoil
z_P	Number of propeller blades

Greek Letters

$\alpha_{C_{L\,max}}$	Maximum-lift angle of attack
α_{0L}	Zero-lift angle of attack
β	Prandtl-Glauert factor
δ_{flap}	Flap deflection angle
η	Efficiency
$\eta_{airfoil}$	Airfoil efficiency
$\overline{\gamma}$	Mean descent angle between approach and touchdown
γ_a	Approach angle of descent
γ_{climb}	Climb angle
γ_{min}	Minimum required climb angle
γ_{TO}	Climb angle after liftoff
γ_2	Climb angle in second segment climb
Λ_{LE}	Leading-edge sweep angle of wing, horizontal or vertical tail
$\Lambda_{max\ thickness}$	Sweep angle of the chordwise position of the maximum thickness of the airfoil
$\Lambda_{1/4}$	Quarter-chord sweep angle of wing, horizontal or vertical tail
λ	Taper ratio of wing, horizontal or vertical tail
μ	Ground rolling resistance
μ’	Corrected ground rolling resistance
ν	Kinematic air viscosity
ρ	Air density
σ	Relative air density, i.e., ρ/ρ_{MSL}

Abbreviations and Acronyms

AR	Aspect Ratio
ARC	Aerodrome Reference Code
BFL	Balanced Field Length
CAS	Calibrated Airspeed
EAS	Equivalent Airspeed
FAA	Federal Aviation Administration
FAR	Federal Aviation Regulations
GTF	Geared Turbofan
ICAO	International Civil Aviation Organization
IDT	Integrated Design Tool
LE	Leading Edge
MAC	Mean Aerodynamic Chord
MSL	Mean Sea Level
MTOM	Maximum Take-Off Mass
MZFM	Maximum Zero-Fuel Mass
NACA	National Advisory Committee for Aeronautics
OEI	One Engine Inoperative
OME	Operating Mass Empty
SAWE	Society of Allied Weights Engineers
SEP	Specific Excess Power
SPP	Standard-Passenger Payload
TFE	Theoretical Fuel Efficiency
TOC	Top Of Climb

1 Introduction

In recent decades, the worldwide demand for civil air transport has grown constantly. This has lead to a continuous increase in both passenger numbers and passenger-kilometers, resulting in comparably high growth rates within the whole civil aviation sector. (Sterzenbach et al. 2009, p.10) According to corresponding market analyses and forecasts, the industry expects this trend to continue within the next decades. (ICAO Economic and Policy Section 2014; AIRBUS S.A.S. 2013b, p.44)

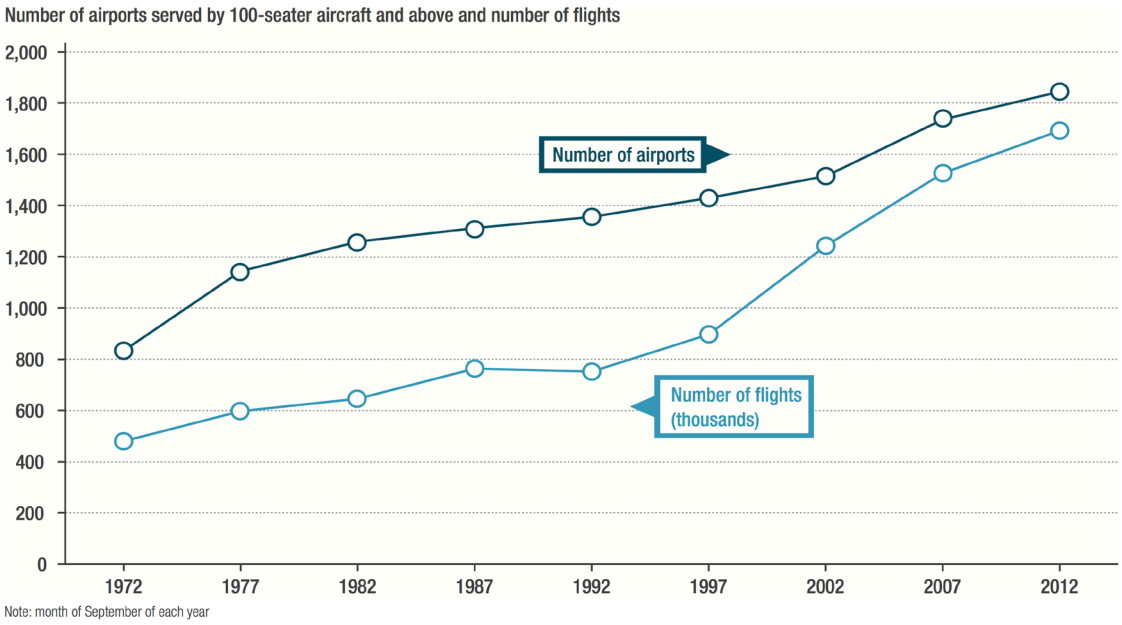

Figure 1.1: Evolution of the worldwide number of airports served by aircraft with 100 seats or more and of the corresponding number of flights for the timespan from 1972 to 2012 (AIRBUS S.A.S. 2013b)

However, the demand for air transport is not distributed evenly around the different regions of the world. More than 80% of the global air transport takes place in Asia/Pacific, Europe and North America. (ICAO Economic and Policy Section 2014) It

is especially in these regions that air traffic growth is increasingly constrained by both air and ground capacity constraints. (Sterzenbach et al. 2009, p.171) In the last two decades, the increase in the total number of flights has been almost twice as high as the growth in the number of airports (Figure 1.1). (AIRBUS S.A.S. 2013b, p.32) Hence, the shortage in capacity to handle more aircraft movements presents a bottleneck for further growth of the aviation economy.

1.1 Short- to Medium-Range Operation of High-Capacity Aircraft

Constantly growing demand for air transport in combination with continuing urbanization concentrates air traffic flows, especially between already congested major hubs. In order to meet the market demand, some airlines operate high-capacity long-range aircraft on short- and medium-range routes already today. For example, Air Canada performs flights from Toronto to Montreal (280 NM (519 km)) with an Airbus A330 (Air Canada 2014, p.214) and Korean Air serves the route from Seoul to Jeju (250 NM (463 km)) with a Boeing 747 (Korean Air 2014, p.7). Airbus statistics prove a general trend towards larger aircraft in the last two decades: The average capacity per aircraft has grown by more than 25%. For airlines, this is a way to meet growing demand on served routes and to reduce costs per seat. (AIRBUS S.A.S. 2013b, p.8) The development shows that in some cases a saturation limit in terms of the achievable transport capacity is in fact being approached already today. (AIRBUS S.A.S. 2013b, p.65)

In this context, the ecological impact is an equally important consideration compared to the growth limitation. Today's high-capacity aircraft are generally designed for long-range operation and are thus less fuel efficient on short- and medium-range missions. Considering the challenging environmental goals the aviation industry is facing, e.g., the European Union's Flightpath 2050 (European Commission High Level Group on Aviation Research 2011), this provides an opportunity for improvement. Kenway et al. have shown that by designing a large aircraft specifically for short ranges, its environmental impact can be considerably reduced. Using today's level of technology, the fuel efficiency of such an aircraft can be significantly higher than the ones of both lower-capacity single-aisle aircraft and short-range-operating long-haul aircraft. (Kenway et al. 2010) The reduced fuel burn in turn reduces the greenhouse gas emissions of the aircraft.

Considering the rising fuel price (AIRBUS S.A.S. 2013b, p.22) and the increasing percentage of airline costs that fuel accounts for (Boeing Commercial Airplanes 2013, p.7), a higher fuel efficiency also provides an economic advantage for the aircraft opera-

tors. According to Kenway et al., there is a potential to reduce cash operating costs by roughly 10%.

The major airframers have realized the current situation and started to address the topic. At the Aviation Expo China 2013 (Beijing Airshow), Airbus has announced to develop a lower-weight variant of the A330 for regional operations. (AIRBUS S.A.S. Press Department 2013; AIRBUS S.A.S. 2013a) Boeing reportedly considers developing a medium-range aircraft of 787-size as a successor to the discontinued 757. (Ng 2014)

At the Institute of Aircraft Design of the Technische Universität München, research is conducted in order to investigate the potential of a high-capacity aircraft specifically designed for operation on short- to medium-range routes. Based on today's level of technology, Iwanizki et al. have developed a novel concept of a transport aircraft that is designed to carry 420 passengers and five tons of cargo over a distance of roughly 1.900 NM (3.500 km). (Iwanizki et al. 2014; Iwanizki 2013) A rendered visualization of the proposed concept is shown in Figure 1.2. In order to maximize the ecological benefit, the aircraft was designed with turboprop engines. In combination with a slightly reduced cruising speed, this type of engine promises higher fuel efficiency than can be attained with turbofan engines. (Howe 2000, p.62) Besides ecological and economic advantages, operational flexibility was emphasized during the concept phase. Aircraft dimensions, take-off and landing performance and boarding and deboarding facilities were designed to enable the aircraft to operate at smaller airfields without jet bridges. A detailed description of this baseline aircraft concept is given in Chapter 2.

Figure 1.2: Computer aided design visualization of the developed high-capacity aircraft concept for short- to medium-range operations (Iwanizki 2013)

1.2 Research Objectives and Methodological Approach

Within the scope of this work, the proposed aircraft concept is analyzed, recalculated, and redesigned. Both elementary initial design techniques as well as more sophisticated detailed aircraft analysis methods are integrated in a comprehensive aircraft design tool that is developed specifically for the application to the aircraft concept to be evaluated. Based on a predefined set of parameters describing the aircraft configuration, the tool carries out calculations covering aerodynamics, masses, propulsion characteristics, and aircraft performance.

The aerodynamic investigation includes a prediction of two-dimensional and three-dimensional lift, estimations for zero-lift drag and drag due to lift as well as appraisals of the effect of high-lift devices.

The topic of mass estimation aims at giving a realistic prediction of the operating mass empty of the aircraft and hence its maximum take-off mass. This in turn is a major driver for the required aerodynamic and propulsive performance.

In conceptual civil aircraft design, the required knowledge of the propulsion characteristics is primarily a question of available thrust and fuel consumption within the entire flight envelope of the aircraft. If existing engines are to be used, the engine manufacturer generally provides these data. In the case of the considered aircraft concept, specifically designed engines are needed, which demands an independent engine performance model. As mentioned above, turboprop engines are selected. Thus, a performance model is developed that consists of a separate part for the gas-turbine core engine, i.e., its power output and fuel consumption, and another part for the propeller, i.e., its propulsive efficiency and attainable thrust.

Conclusively, the developed design tool contains an aircraft performance module. By combining the results for aerodynamics, masses, and propulsion, the attainable operational performance is predicted. In particular this comprises the payload-range, climb performance, take-off and landing capabilities, operating limitations, and the total fuel consumption on a specified design mission.

The determined performance capability is evaluated with regard to the predefined requirements and constraints. Critical design parameters of the concept are identified, and the corresponding requirements and constraints are reappraised. Redesign possibilities of the aircraft concept are evaluated and assessed through an iterative design process.

The parametric approach of the integrated design tool is developed to provide a convenient way of redefining and recalculating the aircraft concept in the process of design optimization.

1.3 Structure of this Thesis

In this thesis, a comprehensive analysis of the high-capacity short- to medium-range aircraft concept of Iwanizki et al. is presented. A parametric integrated design tool is elaborated, with which conceptual aircraft design methodology is applied to the aircraft concept. Its performance capabilities are estimated and the accomplishment of design requirements and constraints is assessed. Crucial aspects of the design are identified and evaluated. The concept is then revised.

Chapter 2 contains a description of the baseline aircraft concept that is investigated in this work. The derivation of the design requirements is explained, and a description of the key features of the configuration is given. In Chapter 3, the applied aircraft analysis methodology is presented. This includes the methods of calculation in the fields of aerodynamics, masses, and propulsion, as well as the integration into the developed design tool and the structure thereof. Chapter 4 deals with the results obtained for the baseline concept and the corresponding performance analysis. The findings are discussed and redesign possibilities are developed. As part of Chapter 5, the baseline concept is revised and refined with regard to the performance requirements. In Chapter 6, important results of the analysis carried-out and refinement are summarized. Finally, possible starting points for future work are suggested.

2 Baseline Aircraft Concept and its Features

Within the scope of research on possibilities to reduce the environmental impact of commercial air transport at the Institute of Aircraft Design of the Technische Universität München, the ecological benefit of a high-capacity aircraft designed specifically for the operation on short- to medium-range routes is investigated. In this context Iwanizki et al. have developed a turboprop-powered double-deck concept aircraft designed to carry 420 passengers over a design range of approximately 1.900 NM (3.500 km). (Iwanizki et al. 2014; Iwanizki 2013) In this chapter a detailed description of the concept is given as well as a summary of the market analysis that lead to the specification of the design requirements.

2.1 Design Requirements and Constraints

The derivation of requirements for the novel short- to medium-range high-capacity aircraft concept performed by Iwanizki et al. (2014) was based on three different resources:

- The global market forecasts provided by the airframe companies Airbus and Boeing (current editions can be found under AIRBUS S.A.S. (2013b) and Boeing Commercial Airplanes (2013), respectively),
- an analysis of flight data collected in the OAG database of worldwide flights (OAG 2014) exemplary for the month of June 2008 and
- a comparison with historical and currently existing aircraft and engines of a similar category.

Findings of the market forecast analysis include the following key points: The volume of global air transport is expected to grow rather continuously, while the demand for new aircraft is further driven by the need to replace old aircraft and to increase efficien-

cy. The Asia/Pacific region will remain the world's largest air traffic market. (ICAO Economic and Policy Section 2014) Even though the majority of regional routes worldwide will be served by single-aisle aircraft, it is especially in Asia where high-capacity aircraft are demanded to handle concentrated intra-regional traffic. Already today, the average aircraft capacity on intra-regional routes is higher in Asia than in any other region worldwide. (AIRBUS S.A.S. 2013b, p.62) However, also in other regions, a demand for high-capacity regional transport is seen, especially in Europe with its hub-and-spoke structured transport networks. (AIRBUS S.A.S. 2013b, p.65) Regardless of this, conventional twin-aisle aircraft are further needed for long-haul operations. In summary, forecast trends of the air traffic market revealed a demand for high-capacity aircraft designed for regional operation, which was the starting point for the development of an appropriate aircraft concept.

Besides the market forecast, the structure of current flight operations was evaluated based on the OAG database of worldwide scheduled flights, that was available for the month of June in 2008. Four regions were distinguished: North America (NA), Europe (EU), Africa/Middle East (AF) and Asia/Pacific (AS). In order to examine regional operations, long-range and inter-regional flights were excluded from the analysis. It was found that roughly 90% of all flights cover distances of less than 1.620 NM (3.000 km) (Figure 2.1). Single-aisle aircraft performed the majority of these flights, whereas long-range aircraft were operated on such routes more often especially in Asia.

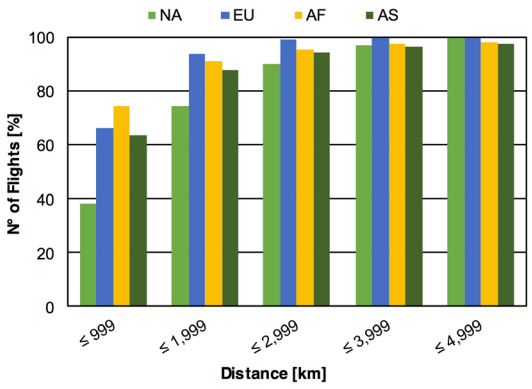

Figure 2.1: Percentage of total number of scheduled regional flights in June 2008 against distance covered, adapted from Iwanizki et al. (2014)

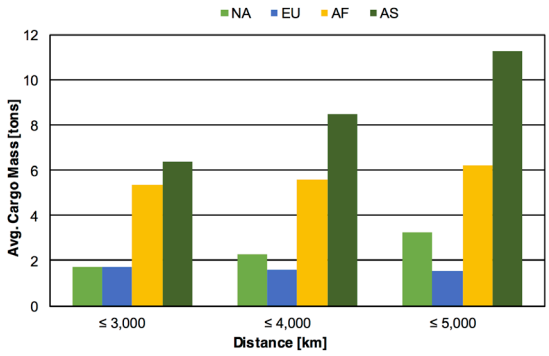

Figure 2.2: Average cargo mass transported per scheduled regional flight in June 2008, adapted from Iwanizki et al. (2014)

Furthermore, an evaluation of the average cargo mass per flight, transported in addition to passengers and their luggage, has been carried out. The results illustrated in Figure 2.2 show that in Africa/Middle East and Asia/Pacific, the average amount of

cargo is more than double compared to North America and Europe. Generally, the cargo mass per flight increases with distance flown. For distances of less than 1.620 NM (3.000 km), the average transported cargo mass ranges from roughly two tons in North America and Europe to about six tons in Asia.

As a basis for comparison as well as for a feasibility analysis, data of existing high-capacity propeller aircraft were gathered. Both historical and current configurations were analyzed, including the Canadair CL-44, Tupolev Tu-114, Lockheed L-188, and Antonov An-10 as passenger transports plus the Antonov An-70 and Airbus A400M as current military transport configurations. In addition, turboprop engines in the presumably needed equivalent take-off power range of roughly 10 MW were examined. In this category, only Russian and Ukrainian engines exist, the most modern of which is the Iwtschenko Progress D-27 power plant of the Antonov An-70 aircraft. The most powerful Western turboprop is the engine of the Airbus A400M, the Europrop International TP400 with 8.2 MW shaft power. (Bräunling 2009, p.67) The feasibility study of both existing aircraft and engines did not reveal an obstacle for the proposed concept. Merely the engine could turn out to be challenging, as there is no existing Western power plant in the required power category. Yet, Russian and Ukrainian models prove the general feasibility.

Based on the above-mentioned aspects, Iwanizki et al. specified quantitative design requirements for the high-capacity turboprop aircraft. In order to enable the concept to replace two of today's common mid-range aircraft, i.e., Airbus A320 or Boeing 737, a minimum passenger capacity of 300 in an all-economy-class configuration was stated. An upper limit of 500 seats was drawn to distinguish the concept from current high-capacity long-range aircraft like the Airbus A380 or the Boeing 747 that offer considerably higher passenger capacities in an all-yield-class configuration. The design mission range was specified to be not less than 1.620 NM (3.000 km), which enables the concept to perform 90% of all currently operated regional flights. Considering the relatively great variation in cargo mass transported, a minimum capacity of five tons was defined as a compromise.

In order to benefit from the superior efficiency of turboprop engines compared to turbofans, cruising speed has to be slightly reduced. (Howe 2000, p.62) A goal of 380 kts (195 m/s) of true airspeed was set, which was derived from the performance of the Antonov An-70.

Aircraft dimensions are constrained by the ICAO Aerodrome Reference Code (ARC) (ICAO 2013, p.1-12) and the FAA Airport Index (Federal Aviation Administration 2011, p.4), which are both decisive for the number of airports the aircraft can be operated at. As a high application potential for the aircraft concept was seen in Asia, especially airports in this region were considered in the constraint analysis. In China, development and construction of airports is governmentally controlled and promoted, and hence, most of them are comparably modern and well equipped. (Wolf 2007; cited after Iwanizki 2013) India, however, presents a more difficult environment. Despite growing demand for air transport, infrastructure is out of date and many airports are inoperative. (Chapelon 2006; cited after Iwanizki 2013) As the operation of the aircraft concept should be enabled on the greatest possible number of airfields, an ICAO ARC of 3D and an FAA Airport Index of C were specified as ambitious goals. The ARC category limits the wingspan to 52 m and the runway field length to 1.8 km. The Airport Index restricts the fuselage length to 48.46 m (159 ft). An overview of the specified quantitative design requirements is given in Table 2.1.
Further qualitative requirements include easy ground accessibility, simple manufacturing methods, low maintenance costs and constructive noise mitigation.

Table 2.1: Quantitative design requirements for the high-capacity turboprop aircraft concept (Iwanizki et al. 2014)

Passenger capacity	300 – 500
Cargo capacity	≥ 5 tons
Design range	≥ 3,000 km
ICAO Aerodrome Reference Code	3D
Wingspan	< 52 m
Runway field length	1.2 – 1.8 km
FAA Airport Index	C
Fuselage length	< 48.46 m

2.2 Summary of the Baseline Aircraft Concept

Based on the above-presented requirements and constraints, Iwanizki et al. (Iwanizki et al. 2014; Iwanizki 2013) have developed the aircraft concept that is evaluated in this thesis and named it ‘Propcraft P-420/A.’ It is based on currently available technology so as to make an entry into service in the year 2025 possible. Hence, the potential of high-capacity aircraft for short-/mid-range can be evaluated independent of other effects. Yet, technological innovations remain complementary.

2.2.1 General Layout

The P-420/A concept possesses a conventional layout with fuselage, low wings and tail (cf. Figure 1.2 and the three-view drawing shown in Figure 2.3). The aircraft is powered by four turboprop-engines with tractor propellers. In order to ensure the ground clearance of the propellers, the inner engine nacelles are mounted on top of the wing, whereas the outer nacelles are directly attached to wing from underneath. The wingspan is set to 51.65 m to comply with the ICAO ARC 3D requirement.

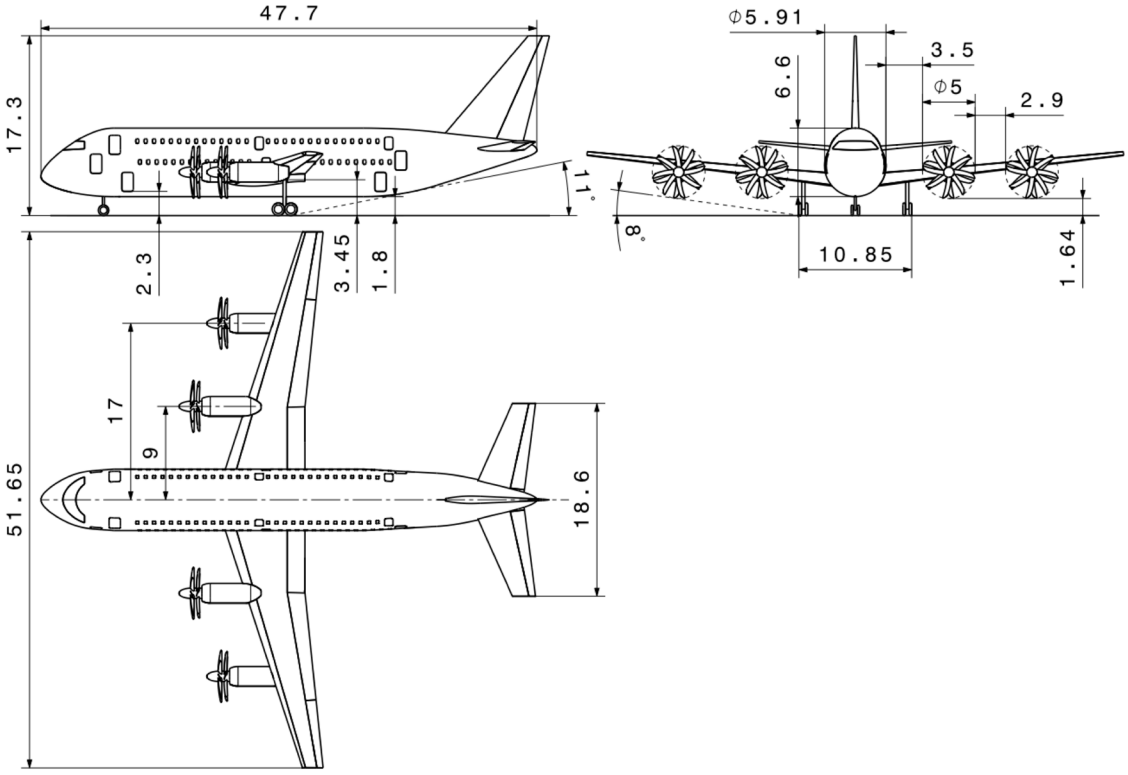

Figure 2.3: Three-view drawing of the baseline high-capacity aircraft concept Propcraft P-420/A (Iwanizki et al. 2014)

With 47.7 m, the fuselage length satisfies the constraint of the FAA Airport Index C. The concept is capable of carrying 420 passengers in an economy-class configuration, which is enabled by a two-deck cabin layout over the entire fuselage length. Figure 2.4 shows the fuselage interior. The main deck features a twin-aisle layout with nine seats abreast, the upper deck six seats per row with a single aisle. Two doors and four emergency exits on the upper deck and four doors plus two emergency exits on the main deck allow for a fast boarding / deboarding and evacuation. Galleys, lavatories, and stairways to connect the decks are positioned at the front and rear of the cabin.

An additional cargo deck below the cabin accommodates the passengers' luggage and a maximum of 10 tons of further cargo in a total of 16 LD3 containers. It is divided into a

fore and aft section by the center wing box, because the wing-fuselage junction is positioned at the level of the cargo deck, so as not to interrupt the passenger cabin. Furthermore, there are four passenger doors with integrated stairs on the cargo deck, which enable aircraft boarding / deboarding independent from ground infrastructure.

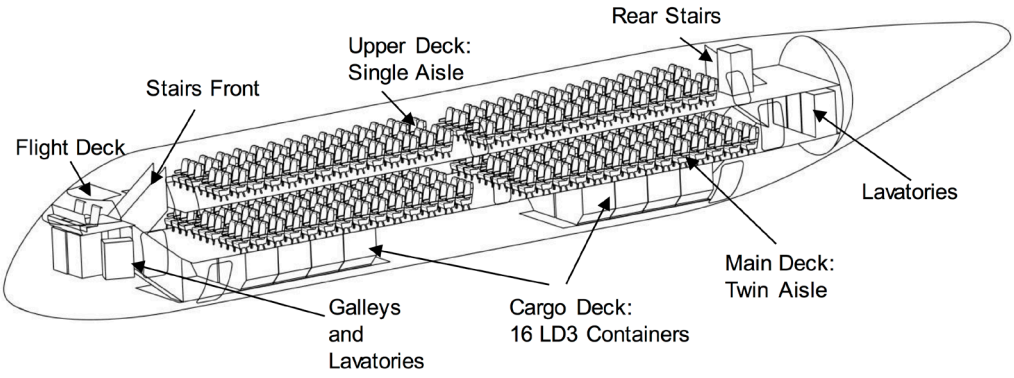

Figure 2.4: Fuselage interior layout of the baseline high-capacity aircraft concept Propcraft P-420/A (Iwanizki et al. 2014)

2.2.2 Technical Data

In addition to the dimensions shown in Figure 2.3, extensive data of the Propcraft P-420/A concept are needed as input for the analyses performed within the scope of this work. In Appendix A, relevant parameters and diagrams are provided after Iwanizki et al. covering geometrical data, aerodynamics, masses and capacities and propulsion characteristics. These data are recalculated and thus updated by this work.

2.2.3 Design Mission and Aircraft Performance

The operational performance of the Propcraft P-420/A concept is evaluated on the basis of a design mission that was specified by Iwanizki et al. as shown in Figure 2.5. It includes a standard-passenger-payload mission (SPP) covering the design range with a design payload plus an additional diversion flight and loiter profile, which is required by certification specifications. (Torenbeek 2013, p.387) In order to enable a comparison of the results of the analyses carried out in this work with the previous estimations, an overview of the design mission specification and the predicted aircraft performance is given in the following.

As depicted in Figure 2.5, the design cruise flight is performed at FL290 at a Mach number of 0.64, which is equivalent to an airspeed of 380 kts (195 m/s). Calculation of the total SPP-range including climb and descent resulted in 1,868 NM (3,460 km). The total fuel mass burned during the SPP mission was estimated with 20.9 tons, an additional 7 tons is required for the diversion / loiter profile and as reserve.

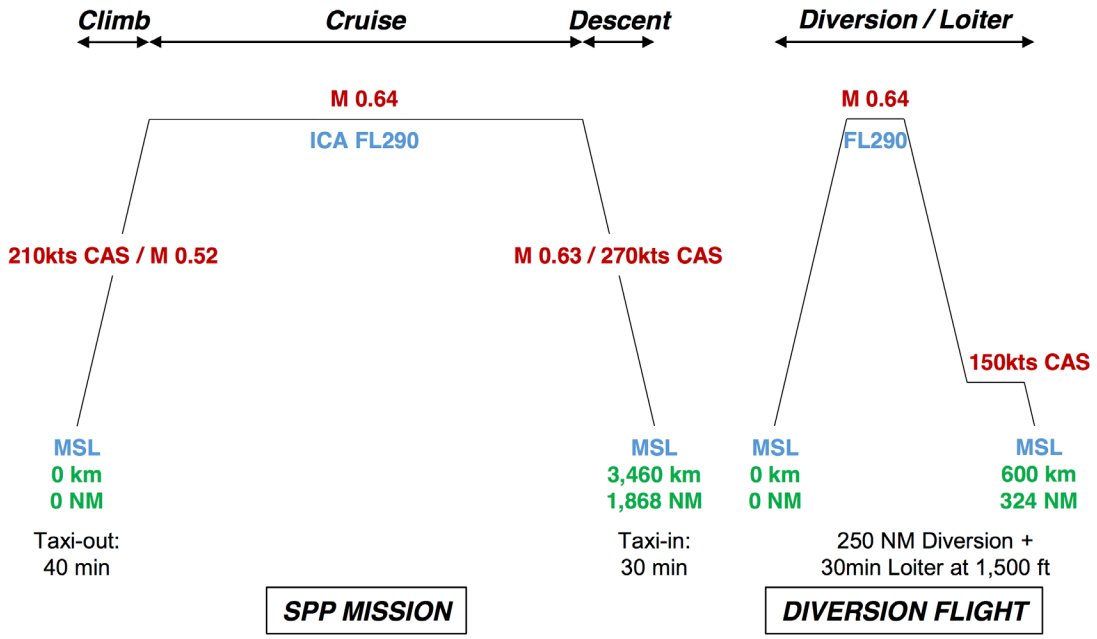

Figure 2.5: Design mission of the baseline high-capacity short-/medium-range aircraft concept Propcraft P-420/A (Randt 2014b)

In order to evaluate and compare the fuel efficiency of the Propcraft P-420/A concept with other aircraft types independent of specific airline operation and passenger load factor, a so-called theoretical fuel efficiency was suggested by Randt (2014b). Data on the actual fuel consumption of aircraft are generally undisclosed. However, the maximum take-off mass *MTOM* and the maximum zero-fuel mass *MZFM* are usually available. Randt assumes that the difference between the *MTOM* and the *MZFM* is the fuel available for a mission with maximum payload (including reserves). The theoretical fuel efficiency *TFE* is then defined as this amount of fuel (in liters) divided by the maximum payload and the attainable range at maximum payload, as shown in Equation (2.1). Both of these values are again generally available for civil aircraft. A value of 0.212 l/t/km was elaborated for the baseline high-capacity short-/medium-range aircraft concept.

$$TFE = \frac{\left(MTOM - MZFM\right) / \rho_{fuel}}{Max.Payload \cdot Range\big|_{at\ Max.Payload}} \qquad \left[\frac{l}{t \cdot km}\right] \tag{2.1}$$

An overview of the performance data is given in Table 2.2. The payload-range diagram shown in Figure 2.6 further describes the estimated transport characteristics of the concept.

Another aspect of aircraft performance is the operating limitations, a summary of which is given in Table 2.3. A maximum operating Mach number of 0.7 was determined as well as a maximum operating altitude of 32,000 ft.

Table 2.2: Performance data of the baseline high-capacity short-/medium-range aircraft concept Propcraft P-420/A (Randt 2014b)

Performance	
True airspeed in cruise flight	380 kts 195 m/s
Mach number in cruise flight	0.64
Initial cruise altitude	29,000 ft
Range (SPP mission)	1,868 NM 3,460 km
Fuel burn (SPP mission)	20,875 kg
Fuel reserves (design mission)	6,976 kg
Theoretical fuel efficiency (max.-payload range)	0.212 l/t/km

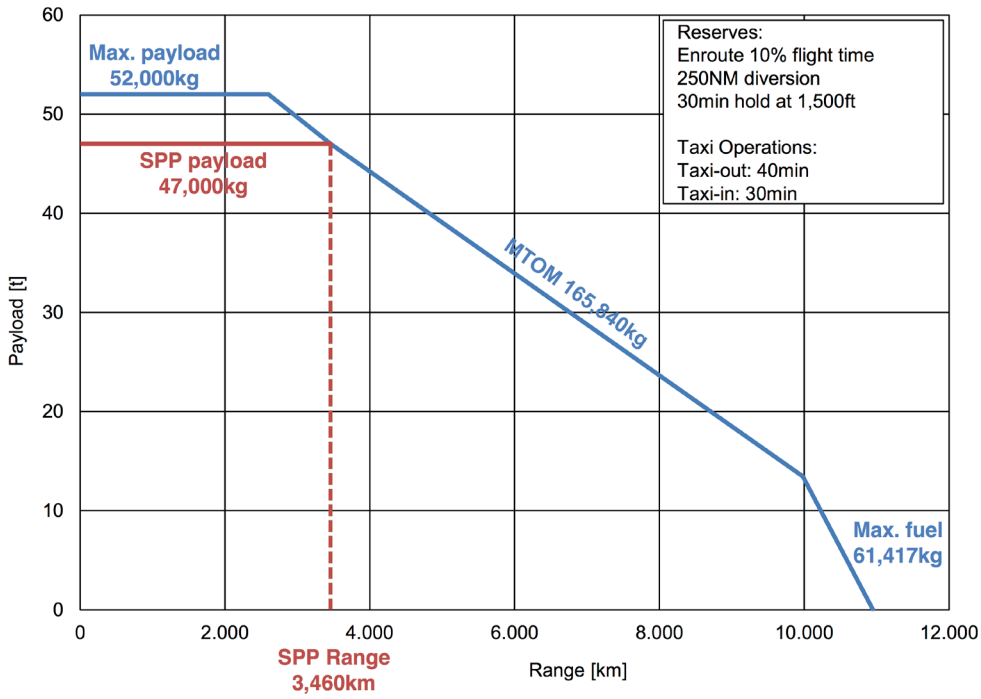

Figure 2.6: Payload-range diagram of the baseline high-capacity short-/medium-range aircraft concept Propcraft P-420/A (Randt 2014b), SPP mission shown in red

Take-off and landing performance is evaluated according to the US Federal Aviation Regulations for commercial aircraft FAR Part 25, cf. Raymer (2012, p.988). Balanced Field Length BFL is the take-off field length required with one engine inoperative OEI until an obstacle clearance height of 35 ft is reached.

The landing field length is measured from descending below a 50 ft obstacle clearance height until full stop on the ground. The FAR Part 25 regulations do not permit reverse thrust when evaluating the landing-distance requirements. Moreover, an additional two-

thirds has to be added to the determined field length as a safety margin that allows for pilot technique. Both balanced field length and landing distance were estimated to be less than 1,800 m, which complies with the ICAO ARC 3D requirement.

Table 2.3: Operating limitations of the baseline high-capacity short-/medium-range aircraft concept Propcraft P-420/A (Randt 2014b)

Operating limitations	
ICAO Aerodrome Reference Code	3D
FAA Airport Index	C
Balanced field length (FAR25)	1,625 m
Landing distance (FAR25)	1,673 m
Maximum operating Mach number	0.7
Maximum operating altitude	32,000 ft

3 Aircraft Concept Analysis Methodology and Integrated Design Tool

The baseline high-capacity aircraft concept for short-/medium-range as presented in Chapter 2 is analyzed and recalculated within the scope of this work. In a comprehensive approach, an integrated design tool (IDT) is developed specifically for the application case of the high-capacity turboprop concept. Starting from a set of elementary input parameters, the tool computes aerodynamic properties, estimates masses, and models propulsion characteristics, which finally enables substantiated statements on the estimated aircraft performance.

In this chapter, the developed design tool and the contained conceptual aircraft analysis methodology are presented in detail. The application case, required input parameters, and the workflow of the IDT are illustrated. Calculation methods of the different sections of the tool are explained and references to their sources are given.

3.1 Approach to the Aircraft Design Process

Torenbeek names the initial design phase of a novel aircraft concept “configuration development.” (Torenbeek 1982, p.4) As shown in Figure 3.1, he subdivides this process into a “conceptual phase” and a “preliminary phase.” During the conceptual phase, requirements and constraints are evaluated, and from these, a design concept is derived, resulting in the initial baseline design. In the case of the high-capacity short-/medium-range aircraft concept, this has been carried out by Iwanizki et al., cf. Chapter 2. The preliminary phase proceeds from the baseline design with a detailed analysis of the concept’s properties and estimated performance. In the form of design cycles, the con-

cept is developed further until a stage is reached where it is considered sufficiently conceived. The configuration development can then be concluded with a technical description of the concept, and the detailed design phase can be commenced.

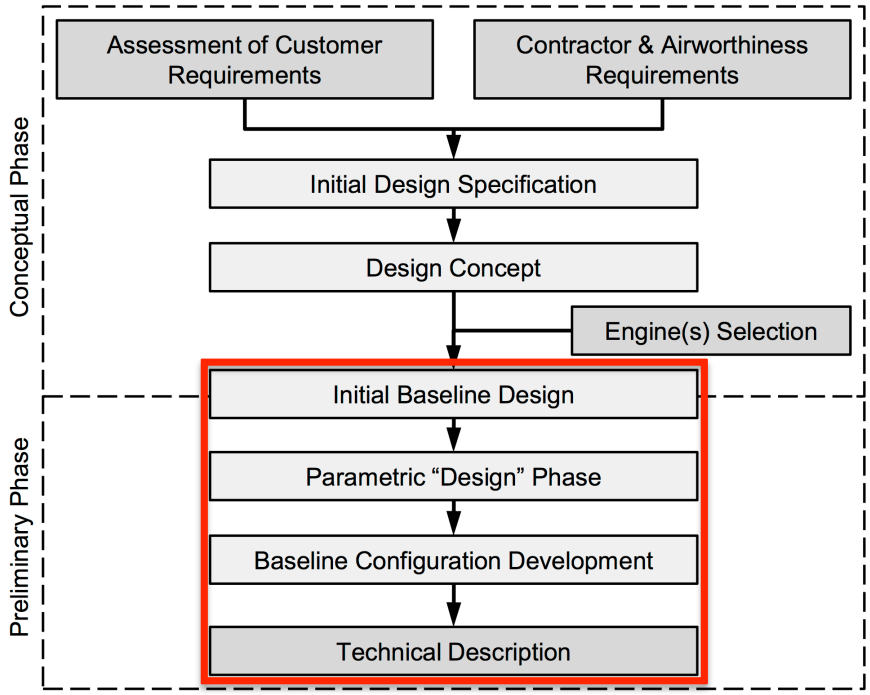

Figure 3.1: Structure of the aircraft configuration development process after Torenbeek (1982, p.5), cited after Seitz (2011, p.6), the part of the process that is covered within the scope of this work is marked in red

The IDT proposed with this thesis is developed to quickly, yet comprehensively analyze elementary properties of an existing baseline aircraft concept and to provide technical and performance data. The tool can be utilized to easily perform parametric analyses and design cycles. The output of the tool can be used for the technical description of the developed aircraft concept, which makes the tool applicable throughout the whole preliminary design phase as marked in red in Figure 3.1.

3.1.1 Structure and Modules of the Integrated Design Tool

The IDT is implemented in the MATLAB environment (release 2013a) (The MathWorks Inc. 2014). This enables its application on any system that supports MATLAB and, moreover, provides direct source code accessibility.

The file 'design_tool.m' is the main script of the IDT, which comprises the code for most of the performed calculations. Some extensive or repeatedly needed algorithms are implemented in separate '~.m'-files as subfunctions and are run from the main script. In

order to structure the roughly 5,500 lines of code, the IDT is subdivided into different modules:

- Aircraft concept definition: Firstly, the aircraft concept to be investigated is specified with a comprehensive set of parameters, see Section 3.2. This includes geometrical and mission parameters. In a second step, the tool computes further parameters from these, e.g., aspect ratio and mean aerodynamic chord.
- Mass estimation: The second module of the IDT comprises four different detailed aircraft mass estimation methods published by Raymer (2012), Torenbeek (1982), Torenbeek (2013), and Howe (2000). Because each of these methods consists of an extensive set of equations, the calculations are carried out in subfunctions 'mass_raymer.m', 'mass_torenbeek.m' and 'mass_howe.m.' Further information on the mass estimation is given in Section 3.4.
- Aerodynamics: The computations carried out in this module cover the estimation of lift and drag in all relevant flight regimes including the effect of high-lift devices. Again, methods of various authors are employed. A detailed description follows in Section 3.3.
- Propulsion: The methodology applied in this module is based on both published modeling practices as well as an analysis of existing engine data. Section 3.5 covers the developed propulsion model in detail. As some propulsion aspects are needed for several calculations, they are implemented as separate subfunctions that can be run from the main script, i.e., 'engine_power.m', 'engine_fuel_consumption.m' and 'propeller_efficiency.m.'
- Aircraft performance analysis: In this final module of the IDT, aircraft performance characteristics are elaborated both in general and with regard to the design mission (cf. Section 2.2.3). Furthermore, operating limitations are evaluated. The calculations are presented in detail together with the corresponding results in Section 4.4.

The output of the IDT analysis results is realized in two ways. Numerical values are arranged in the MATLAB Command Window according to the module subdivision as described. Besides, plots and diagrams are created, each of which opens in a separate window. Proper identification of these is ensured through window titles and legends.

A schematic visualization of the workflow of the IDT is shown in Figure 3.2 including the possibility to perform design cycles and the interfaces to the configuration development process as introduced in Section 3.1.

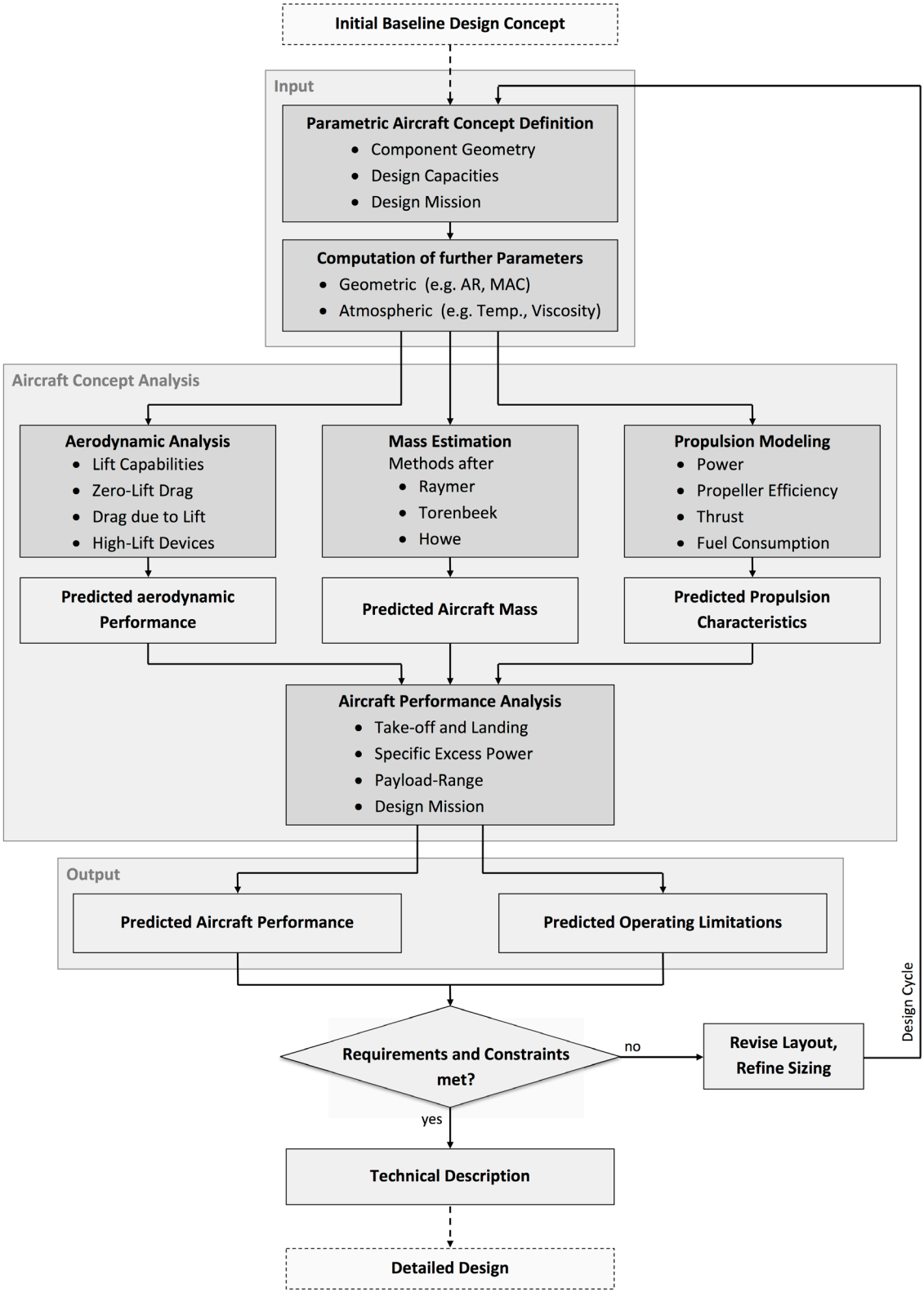

Figure 3.2: Flow chart of the IDT and its application to the preliminary design of the high-capacity short-/medium-range aircraft concept Propcraft P-420/A

3.1.2 Application Case Limitation

An important restriction of the IDT has to be pointed out regarding its applicability. The tool has been developed to analyze the high-capacity short- to medium-range aircraft concept investigated within the scope of this work. In the current version, it is not a universal aircraft design application, but specifically tailored to the present application case.

However, through its parametric approach, the IDT enables configuration variation within well-defined limits:

- The general layout of the investigated configuration has to be the one of a conventional transport aircraft consisting of a fuselage, low wings with a high aspect ratio (i.e., at least greater than three), wing-mounted engines, and empennage. The corresponding geometric parameters can be varied freely. Special or unconventional features such as canards or winglets cannot be modeled.
- Aircraft operation is assumed to occur only in a subsonic flight regime, i.e., below the drag-divergence and the critical Mach number. Transonic or supersonic effects are not included in the aerodynamic calculations.
- The propulsion module of the IDT models the characteristics of a turboprop engine. Other types of propulsion are not accounted for. The number of engines and the engine properties can be edited though.
- The general profile of the design mission is specified according to Section 2.2.3 as a typical transport mission including a range flight plus a diversion. Yet, parameters such as altitudes or airspeeds of the different segments are editable.

To summarize, the IDT allows for sizing, revision or refinement, and trade studies of a conventional turboprop-powered transport aircraft at subsonic speeds. Other configurations cannot be dealt with unless significant enhancements to the tool are made.

3.2 Required Input Parameters

Before running the IDT, all required input parameters have to be specified in the first section of the ‘design_tool.m’-source code. There, they are grouped in the sections general, wing, horizontal tail, vertical tail, fuselage, landing gear, cabin and propulsion. In Appendix 0, all parameters are listed and short explanations are given where necessary.

3.3 Aerodynamics Analysis Module

Based on the parameters presented above, the IDT performs various analyses. In accordance with the arrangement in pertinent aircraft design literature, the aerodynamic analysis is presented first in this thesis, although it is implemented as the second module of the IDT.

Key aspects covered are the determination of lift, drag, and high-lift device characteristics. For most of these, several calculation methods are implemented that were developed by different authors in order to allow for an assessment of the accuracy and for comparison purposes.

3.3.1 Lift Curve

Uncambered wings produce no lift at zero angle of attack while a negative angle of attack is required to obtain zero lift with cambered wings. The zero-lift angle of attack of the wing α_{0L} can be considered approximately equal to the zero-lift angle of the airfoil. (Raymer 2012, p.418) Separate values for slow, low flight, and cruise flight are input parameters of the IDT, cf. Appendix B.2.

Starting from the zero-lift angle, the slope of the lift curve is essentially linear until the stall angle is approached. Maximum lift is obtained at the stall angle, while lift decreases rapidly at even higher angles of attack, because the airflow over the wing has separated.

3.3.1.1 Lift Curve Slope

Generally, normal aircraft operation only takes place in the linear part of the lift curve, which allows for easy calculation of lift according to Equation (3.1). The slope of the lift curve $C_{L\alpha}$, however, is dependent on the airfoil's (two-dimensional) lift-curve slope, the wing geometry, and the flight Mach number.

$$C_L = C_{L\alpha}\left(\alpha - \alpha_{0L}\right) \tag{3.1}$$

Lowry and Polhamus (1957) (cited after Raymer 2012, p.412) have developed a semi-empirical formula for the wing lift-curve slope, Equation (3.2), that is implemented in the IDT.

$$C_{L\alpha} = \frac{2\pi A}{2 + \sqrt{4 + \frac{A^2\beta^2}{\eta_{airfoil}^{\ 2}}\left(1 + \frac{\tan^2 \Lambda_{max\,thickness}}{\beta^2}\right)}} \frac{S_{exposed}}{S_{ref}} F \tag{3.2}$$

with

$$\beta^2 = 1 - M^2 \tag{3.3}$$

$$\eta_{airfoil} = \frac{C_{l\alpha}}{2\pi / \beta} \tag{3.4}$$

$$F = 1.07(1 + d_h / b)^2 \tag{3.5}$$

where A is the aspect ratio, $\eta_{airfoil}$ the airfoil efficiency factor, and C_{l_α} the lift-curve slope of the airfoil. $\Lambda_{max\ thickness}$ is the wing sweep angle at the chord location where the airfoil is thickest. The exposed wing planform area $S_{exposed}$ is the wing reference area S_{ref} less the part covered by the fuselage. d_h is the horizontal fuselage diameter and b the wingspan. As Equation (3.2) is dependent on the Mach number M, it is evaluated for both the design Mach numbers for slow, low, and for cruise flight, cf. Appendix B.1.

3.3.1.2 Maximum Lift

Because of the non-linearity of the lift curve near the stall angle, the maximum attainable lift occurs at a greater angle of attack than the corresponding linear value. Finck et al. (1978) (cited after Raymer 2012, p.417) have developed a method for estimating maximum lift and stall angle for high-aspect-ratio wings including Mach number effects, cf. Equations (3.6) and (3.7). Hence, separate values are elaborated again for slow, low, and for cruise flight.

$$C_{L\,max} = C_{l\,max}\left(\frac{C_{L\,max}}{C_{l\,max}}\right) + \Delta C_{L\,max} \tag{3.6}$$

$$\alpha_{C_{L\,max}} = \frac{C_{L\,max}}{C_{L\alpha}} + \alpha_{0L} + \Delta\alpha_{C_{L\,max}} \tag{3.7}$$

$C_{l\,max}$ is the airfoil's maximum lift coefficient at $M = 0.2$. The term $(C_{L\,max} / C_{l\,max})$ corrects this value for wing geometry effects, while $\Delta C_{L\,max}$ is a Mach number correction. $\Delta\alpha_{C_{L\,max}}$ is the angle-of-attack increment of the stall angle compared to the linear value. All of these parameters have to be derived graphically from corresponding diagrams and are thus required as input parameters of the IDT, cf. Appendix B.2.

3.3.1.3 Propeller Effect on Lift

As suggested by Iwanizki (2013, p.45), an attempt is made to include the effect of the propeller slipstream acting on the wing in the lift analysis. Roskam (1990, p.286) presents an equation to estimate the lift increase due to the increased dynamic pressure behind the propellers, cf. Equation (3.8).

$$\Delta C_{L,prop} = \sum_{i=1}^{n_{eng}} \frac{S_{slipstream,i}}{S_{ref}} C_L \frac{2200 P_{av,i}}{q V \pi D_{p,i}^{\ 2}} \tag{3.8}$$

where n_{eng} is the number of engines, $S_{slipstream}$ the part of the wing reference area affected by the propeller slipstream, C_L the lift coefficient at which the wing is operated, P_{av} the available engine power, q the free stream dynamic pressure, V the corresponding velocity and D_p the propeller diameter. Note that the equation has to be applied in Anglo-American units, however, the IDT performs the necessary conversions automatically.

3.3.2 Drag

Drag analysis is split into the analysis of zero-lift (parasite) drag and drag due to lift.

3.3.2.1 Zero-Lift Drag

Parasite or zero-lift drag C_{D0} is independent of the aircraft's production of lift and is (in subsonic flight) mainly caused by skin friction and flow separation. (Raymer 2012, p.429) As the estimation of this drag is crucial to the presumed aircraft efficiency, several different estimation methods are used in the IDT to allow for comparison.

Equivalent Skin-Friction Method:

The equivalent skin-friction method after Raymer (2012, p.429) provides an easy initial estimate of the parasite drag based on the assumption that separation drag is a consistent percentage of skin-friction drag for a specific class of aircraft. According to Equation (3.9) the zero-lift drag coefficient can thus be calculated with the equivalent skin-friction coefficient C_{fe} of the aircraft's category and the ratio of wetted area S_{wet} to reference area.

$$C_{D0} = C_{fe} \frac{S_{wet}}{S_{ref}} \tag{3.9}$$

As the IDT is developed for the analysis of transport category aircraft, the corresponding value C_{fe} = 0.0026 is implemented in the source code of the IDT.

Component Buildup Method:

Raymer (2012, p.429) presents a more detailed approach with the component buildup method. The subsonic parasite drag of each component of the aircraft is estimated with a flat-plate skin-friction drag coefficient C_f and a component form factor FF to account for separation drag. Multiplied with an interference factor Q and the corresponding

wetted area, the total component drag is determined and summed over all components, as shown in Equation (3.10).

$$C_{D0} = \frac{\sum_{c} C_{f,c} FF_c Q_c S_{wet,c}}{S_{ref}} + C_{D,misc} + C_{D,L\&P} \tag{3.10}$$

Additionally, $C_{D,misc}$ covers the drag of miscellaneous special features such as an up-swept aft fuselage or special items such as flaps or an extended landing gear. $C_{D,L\&P}$ is an estimation of the contribution of leakages and protuberances.

The component breakdown realized in the IDT considers fuselage, wing outside the propeller slipstream, wing in slipstream, horizontal tail, vertical tail, and engine nacelles separately.

The skin-friction coefficients are mainly affected by the extent of laminar flow over the surface of the respective component. Typically, most of the airflow over the wetted surface of an aircraft is turbulent. However, some laminar flow occurs especially in the front part of components. As the turbulent flow produces a much higher skin-friction drag than a laminar flow, an estimation of the attainable part of laminar flow over the surface of the components has to be made. In accordance with Raymer (2012, p.432), the following assumptions are implemented in the IDT, see Table 3.1. As laminar flow is unlikely to occur downstream of a spanwise crack, the flow over the wing is considered turbulent downstream of the position where the slats meet the wing.

Depending on the Reynolds number (Equation (3.11)), flat-plate skin-friction coefficients can be calculated for laminar and for turbulent regime according to Equations (3.12) and (3.13), respectively.

Table 3.1: Attainable laminar flow over the aircraft components as percentage of the respective wetted area

Laminar flow percentages	
Fuselage	10%
Wing (outside of propeller slipstream)	Area from leading edge (LE) to crack of slats
Wing (in propeller slipstream)	80% of area from LE to crack of slats
Horizontal tail	20%
Vertical tail	20%
Engine nacelles	0%

Reynolds number as a function of velocity V, characteristic length l and kinematic viscosity ν:

$$Re = \frac{Vl}{\nu} \tag{3.11}$$

Laminar:

$$C_f = \frac{1.328}{\sqrt{Re}} \tag{3.12}$$

Turbulent:

$$C_f = \frac{0.455}{(\log_{10} Re)^{2.58}(1+0.144M^2)^{0.65}} \tag{3.13}$$

In addition to the above considerations regarding laminar flow, a constraint has to be set that accounts for the effect of skin surface roughness. A flow over a relatively rough surface will be turbulent and produces an even higher skin-friction coefficient than indicated by Equation (3.13). This influence is modeled with a fictitious "cutoff Reynolds number" that is calculated for subsonic regime from Equation (3.14) with the skin roughness value k. For a smoothly painted surface, this value is taken as $k = 0.634 \cdot 10^{-5} m$. If the calculated cutoff Reynolds number is lower than the actual Reynolds number, skin roughness increases drag and hence the cutoff Reynolds number is used in Equation (3.13).

$$Re_{cutoff} = 38.21\left(\frac{l}{k}\right)^{1.053} \tag{3.14}$$

Finally, the total flat-plate skin-friction coefficient is the weighted average of the laminar and turbulent coefficients corresponding to the laminar flow percentage from Table 3.1.

Component form factors FF correct the flat-plate skin-friction coefficients for pressure drag caused by flow separation. After Raymer (2012, p.435), the following estimations are employed.

Fuselage:

$$FF = \left(1 + \frac{60}{f^3} + \frac{f}{400}\right) \tag{3.15}$$

with

$$f = \frac{l_f}{(d_h + d_v)/2} \tag{3.16}$$

where l_f is the fuselage length, d_h the horizontal and d_v the vertical fuselage diameter.

Wing, horizontal and vertical tail:

$$FF = \left[1 + \frac{0.6}{(x/c)_{max\ thickness}}\left(\frac{t}{c}\right) + 100\left(\frac{t}{c}\right)^4\right]\left[1.34\,M^{0.18}(\cos\Lambda_{max\ thickness})^{0.28}\right] \quad (3.17)$$

where $(x/c)_{max\ thickness}$ is the relative chordwise position of the maximum thickness of the airfoil, (t/c) the relative maximum thickness and $\Lambda_{max\ thickness}$ the sweep angle of the wing at the chord location where the airfoil is thickest.

Nacelles:

$$FF = 1 + (0.35/f) \quad (3.18)$$

with

$$f = \frac{l_{eng}}{d_{eng}} \quad (3.19)$$

where l_{eng} is the nacelle length and d_{eng} the nacelle diameter.

Component interference factors Q are employed as listed in Table 3.2. (Raymer 2012, p.437) The wetted areas of the aircraft components are estimated from the corresponding geometric parameters, cf. Section 3.2.

In the drag category of miscellaneous special features $C_{D,misc}$, the drag of additional flow separation due to the upsweep of the aft fuselage is evaluated with Equation (3.20).

$$C_{D,misc,aft\,fuselage} = 3.83u^{2.5}\frac{\pi}{4}\left(\frac{d_h + d_v}{2}\right)^2 \Big/ S_{ref} \quad (3.20)$$

where u is the upsweep angle in radians of the fuselage centerline.

Table 3.2: Component interference factors for zero-lift drag component buildup method

Component interference factors		
Fuselage	1	
Wing (outside of propeller slipstream)	1	
Wing (in propeller slipstream)	1	
Horizontal tail	1.05	
Vertical tail	1.05	
Engine nacelles	1.5	For nacelles mounted directly to the wing without pylons

The influence of leakages and protuberances is difficult to predict in detail and thus their drag increment $C_{D,L\&P}$ is estimated as percentage of the total parasite drag. According to Raymer (2012, p.444) a value of 5% is applied for propeller aircraft.

Method after Howe:

A third approach to estimate the zero-lift drag implemented in the IDT is the semi-empirical method after Howe (2000, p.147).

$$C_{D0} = 0.005\left(1-\frac{2c_{lam}}{R_W}\right)\overline{\tau}\left[1-0.2M+0.12\left\{\frac{M(\cos\Lambda_{1/4})^{0.5}}{(A_f - t/c)}\right\}^{20}\right]R_W T_f S_{ref}{}^{-0.1} \quad (3.21)$$

with

$$\overline{\tau} = \left[\frac{R_W - 2}{R_W} + \frac{1.9}{R_W}\left\{1+0.526\left(\frac{t}{c}\Big/0.25\right)^3\right\}\right] \quad (3.22)$$

where c_{lam} is the chord fraction of the wing with laminar flow, $R_W = S_{wet}/S_{ref}$, $\Lambda_{1/4}$ is the quarter-chord wing sweep, $A_f = 0.85$ is an airfoil factor and $T_f = 1.4$ an aircraft type factor for turboprop airliners.

Drag of Special Items:

In addition to the zero-lift drag coefficient of the whole aircraft, drag contributions of special single items are of interest. For a propeller transport configuration, these are in particular the extended landing gear, deployed speed brakes, and an inoperative engine.

Compared to other aircraft components, the derivation of an accurate prediction of the drag of an extended landing gear is difficult. One approach is a comprehensive procedure of adding up drag values for individual landing gear components such as struts, bogeys, and wheels. A description of this method and the corresponding component drag values can be found in Raymer (2012, p.442).

A closer look reveals, however, that landing gear drag is not a constant value, but dependent on the local flow condition. (Mair and Birdsall 1992, p.124; Torenbeek 1982, p.550) Therefore, the landing gear drag coefficient is dependent on the angle of attack and flap setting of the aircraft. An empirical equation taken from Mair and Birdsall (1992, p.124) is implemented in the IDT that provides landing gear drag as a function of flap setting and maximum take-off mass *MTOM*, cf. Equation (3.23).

$$\Delta C_{D0,landing\,gear} = \frac{MTOMg}{S_{ref}} K_{UC} MTOM^{-0.215} \quad (3.23)$$

with

$$K_{UC} = \begin{cases} 5.81 \cdot 10^{-5} & \text{for zero flap deflection} \\ 4.485 \cdot 10^{-5} & \text{for take-off flap deflection} \\ 3.16 \cdot 10^{-5} & \text{for maximum flap deflection} \end{cases} \quad \left[\frac{\mathrm{m}^2}{\mathrm{N\,kg}^{-0.215}} \right] \tag{3.24}$$

The drag increase attainable with wing mounted speed brakes can be estimated with Equation (3.25) after Raymer (2012, p.442).

$$\Delta C_{D0,speed\ brakes} = 1.6 \frac{S_{speed\ brakes}}{S_{ref}} \tag{3.25}$$

where $S_{speed\ brakes}$ is the frontal area of the deployed brakes, which is estimated with half the area of wing flaps.

Finally, the drag of an inoperative engine needs to be evaluated, because the one-engine-inoperative case (OEI) is important for certification requirements. According to Torenbeek (1982, p.198), modern turboprop engines feature a blade control system that automatically feathers the propeller blades in case of engine failure. Additional drag of a stopped, feathered propeller is estimated with Equation (3.26). (Raymer 2012, p.445)

$$\Delta C_{D0,feathered\ prop} = 0.1 \frac{1}{\mathrm{m}^2} \cdot \frac{B_p}{8\pi} \frac{\pi}{4} D_p{}^2 \tag{3.26}$$

where B_p is the number of propeller blades and D_p the propeller's diameter.

3.3.2.2 Drag due to Lift

With the term "drag due to lift," all drag components are addressed that are a function of lift. This includes induced drag caused by pressure equalization of the airflows over and underneath the wing, e.g., the formation of tip vortices. Yet, other effects such as changes in viscous separation or changes in parasitic drag resulting from altered flow fields with varying lift are also covered by the term. (Raymer 2012, p.455)

In accordance with the theoretic induced drag in inviscid flows, drag due to lift is approximately proportional to the square of the lift coefficient. Therefore, the investigation of drag due to lift C_{Di} is essentially the estimation of the corresponding proportionality factor, also called drag-due-to-lift factor K, cf. Equation (3.27). Again, several methods are presented in the following and implemented in the IDT to allow for comparisons.

$$C_{Di} = K C_L{}^2 \tag{3.27}$$

Statistical Oswald Span-Efficiency Factor:

In an approach first presented by Oswald (1931), the theoretical inviscid proportionality, which is the inverse of the product of aspect ratio A and π, is corrected with a span-efficiency factor e as shown in Equation (3.28).

$$K = \frac{1}{\pi A e} \tag{3.28}$$

The span-efficiency factor is determined with a method that was statistically derived by Cavallo (1966) (cited here after Raymer 2012, p.456) and is based on wing geometry.

For straight-wing aircraft:

$$e = 1.78(1 - 0.045A^{0.68}) - 0.64 \tag{3.29}$$

For swept-wing aircraft:

$$e = 4.61(1 - 0.045A^{0.68})(\cos\Lambda_{LE})^{0.15} - 3.1 \qquad \text{for } \Lambda_{LE} > 30° \tag{3.30}$$

If the leading-edge wing sweep Λ_{LE} is between 0° and 30°, the span-efficiency factor e is linearly interpolated between the results of the two Equations (3.29) and (3.30).

Howe Method:

Another statistical method for estimating the drag-due-to-lift factor has been developed by Howe (2000, p.147) based on geometrical parameters and the Mach number, cf. Equation (3.31).

$$K = \frac{(1 + 0.12M^6)}{\pi A}\left[1 + \frac{(0.142 + f(\lambda)A(10t/c)^{0.33}}{(\cos\Lambda_{1/4})^2} + \frac{0.1(N_{eng\ over\ wing} + 1)}{(4 + A)^{0.8}}\right] \tag{3.31}$$

with

$$f(\lambda) = 0.005\left[1 + 1.5(\lambda - 0.6)^2\right] \tag{3.32}$$

where $N_{eng\ over\ wing}$ is the number of engines mounted over the wing and λ the wing's taper ratio. The IDT calculates the drag-due-to-lift factors for both design slow, low, and design cruise flight.

Nita and Scholz Method:

A third statistical estimation method for the K-factor is applied after Nita and Scholz (2012). In addition to planform geometric parameters and the Mach number, this method takes fuselage influence, zero-lift drag, and wing dihedral into account. The method is multistaged. Firstly, a theoretical Oswald span-efficiency factor is calculated based on taper ratio and wing sweep. This factor is then corrected for the influences of fuselage, zero-lift drag, and Mach number. Finally, effects of non-planarity are taken into

account, i.e., in the case of this work wing dihedral. Refer to the publication of Nita and Scholz for the corresponding equations. (Nita and Scholz 2012)

Leading-Edge-Suction Method:

A more refined approach than the statistical methods presented above is taken by the leading-edge-suction method as presented by Raymer (2012, p.458). The basic concept is that relatively thick airfoils allow streamlines to curve around the leading edge at angles of attack lower than the ones, at which considerable separation occurs. In this case, the airflow follows the leading-edge radius and the rapid curvature creates a pressure drop that exerts a suction force on the leading edge. This leading-edge suction force reduces drag as it "sucks" the airfoil in the direction of flight.

Two extremes can be distinguished. In an ideal two-dimensional case with no viscous separation, the leading-edge suction force produces a drag-free flow known as "d'Alembert's paradox" and called "100% leading-edge suction" here. In this case, the drag-due-to-lift factor K of a three-dimensional wing is the already-mentioned inverse of the product of aspect ratio A and π (Equation (3.33)).

$$K_{100\%} = \frac{1}{\pi A} \tag{3.33}$$

On the other hand, an airfoil with zero thickness (i.e., a flat plate) will experience no leading-edge suction, as there is no forward-facing area for pressure forces to act on. In this worst case (here called "0% leading-edge suction"), the K-factor is the inverse of the slope of the lift curve (Equation (3.34)).

$$K_{0\%} = \frac{1}{C_{L\alpha}} \tag{3.34}$$

In reality, the K-factor of a wing or an aircraft will have a value between these two limits, depending on the operating conditions. The estimation of drag due to lift is thus a question of the attainable percentage of leading-edge suction S, cf. Equation (3.35).

$$K = SK_{100\%} + (1-S)K_{0\%} \tag{3.35}$$

Generally, this percentage is at a maximum when a wing operates at its design lift coefficient. In this case, a typical Oswald span-efficiency factor of $e = 0.8$ can be assumed for subsonic high-aspect-ratio wings. (Raymer 2012, p.462; Torenbeek 1982, p.149) According to Equation (3.36), the corresponding percentage of leading-edge suction can be calculated with aspect ratio and lift-curve slope. This value can be attained from zero lift up to the design lift coefficient plus 0.1. For lift coefficients higher than this polar-break lift coefficient, leading-edge suction gradually decreases to a value of $S_{min} = 0.8 \cdot S_{max}$ at the stall lift coefficient.

$$S_{max} = \left(\frac{1}{e} - \frac{\pi A}{C_{L\alpha}} \right) \Bigg/ \left(1 - \frac{\pi A}{C_{L\alpha}} \right) \tag{3.36}$$

The IDT contains a subfunction 'LE_suction_K_factor.m' to calculate the *K*-factor as a function of the lift coefficient at which the wing operates as described above. Within the scope of this work, the leading-edge-suction method is considered the most realistic, because it is the only one of the presented methods that does not neglect the variation of the *K*-factor with lift coefficient. Raymer (2012, p.458) Further drag calculations in the IDT are therefore performed with this method while results of the other methods are calculated for comparison purposes.

Ground Effect:

If a wing is operated near the ground, i.e., at a height of less than half the wingspan, drag due to lift is significantly reduced. A theoretical explanation of this effect is that the induced downwash angle downstream of the wing is limited by the ground proximity. For wing-in-ground-effect operation, drag due to lift is thus estimated with a reduced *K*-factor, cf. Equation (3.37). (Hoerner and Borst 1975; cited after Raymer 2012, p.463)

$$\frac{K_{in\,ground\,effect}}{K} = \frac{33(h/b)^{1.5}}{1+33(h/b)^{1.5}} \tag{3.37}$$

where *h* is the height of the aircraft, i.e., the wing, above ground.

3.3.2.3 Subsonic-Flight-Regime Constraint

As mentioned in Section 3.1.2, it is important to note that transonic or supersonic effects are not included in the introduced drag prediction methods. Hence, all results are only accurate for Mach numbers below the drag-divergent Mach number M_{DD}. Raymer (2012, p.449) presents a method after Boeing to graphically derive a preliminary estimate of the drag-divergent Mach numbers separately for wing and fuselage. This allows for a check whether subsonic drag estimation methods can be applied accurately.

3.3.3 High-Lift Devices

In order to enable an adjustment of the aerodynamic characteristics of the wing to different flight situations, most aircraft today are equipped with high-lift devices. For take-off and landing, high lift is required, which demands a highly cambered airfoil and a low wing loading. In cruise flight, however, low camber and a high wing loading increase efficiency. To resolve this contradiction, high-lift flaps can be deployed from the wing for take-off and landing. These typically increase camber and in the case of Fowler-type flaps also increase the wing area.

Due to the variety and complexity of high-lift devices, the estimation of high-lift characteristics is difficult in the conceptual design phase, when the exact configuration is not yet known. In the following, empirical calculation methods for the effect of high-lift devices on lift and drag are presented. Leading-edge slats in combination with single- and double-slotted Fowler flaps (cf. Figure 3.3) are considered for the calculations in the IDT, as they are the most common types of high-lift devices employed in modern transport aircraft. (Rudolph 1996, p.117)

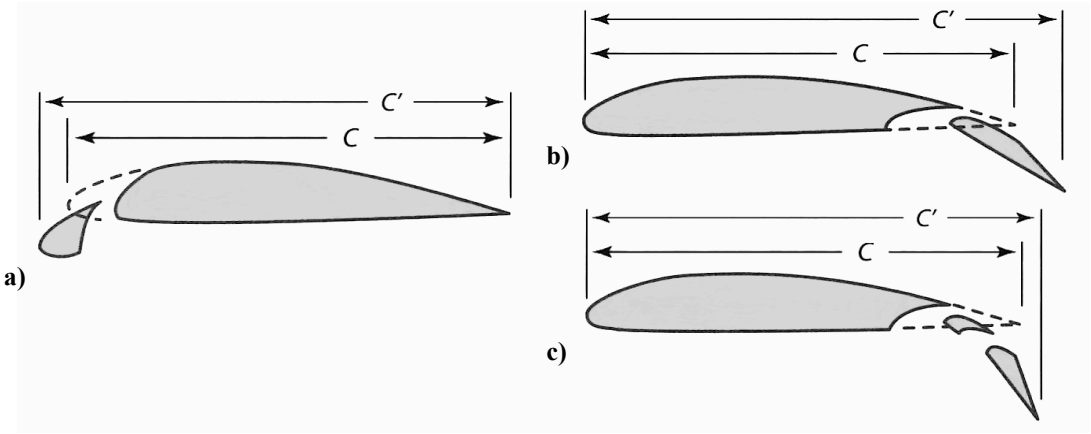

Figure 3.3: High-lift devices considered in the high-lift analysis of the IDT, a) slotted leading-edge flap (slat), b) single-slotted Fowler flap, c) double-slotted Fowler flap, original wing chord is marked with *c* and extended wing chord with *c'*, adapted from Raymer (2012, p.425)

3.3.3.1 High-Lift Effect on Lift

In principle, the above-mentioned high-lift devices have three effects on lift. Firstly, because of the increased camber, the zero-lift angle of attack is shifted towards more negative values. Secondly, the effective slope of the lift curve is greater than the original one, since the high-lift devices increase the total wing area (cf. the chord lengths depicted in Figure 3.3). Thirdly, the maximum attainable lift and the angle of attack at which it occurs are changed. All parameters are evaluated for a landing setting (flaps fully deployed) and for a reduced flap setting (take-off).

The change in the zero-lift angle of attack due to Fowler flaps is estimated with empirical Equation (3.38) after Raymer (2012, p.428). Slats have no effect on the zero-lift angle within the scope of this modeling.

$$\Delta\alpha_{0L} = (\Delta\alpha_{0L})_{airfoil}\left(\frac{S_{flapped}}{S_{ref}}\right)\cos\Lambda_{hingeline} \tag{3.38}$$

where $(\Delta\alpha_{0L})_{airfoil}$ is the change in zero-lift angle in the two-dimensional case. After Raymer, it is approximately -15° for the landing and -10° for the take-off setting. $S_{flapped}$ is the part of the wing planform area affected by the flaps. $\Lambda_{hinge\ line}$ is the sweep angle of the hinge line of the high-lift surface. The IDT calculates these parameters from the specified wing geometry.

Due to the extended wing chord (cf. Figure 3.3), high-lift devices increase the effective wing area. As the lift coefficient is referenced to the standard reference area of the wing, however, the slope of the lift curve increases. According to Roskam (1990, p.260), the altered lift-curve slope can be calculated from Equation (3.39).

$$C_{L\alpha,high\,lift} = C_{L\alpha}\left[1+\left(\frac{c'}{c}-1\right)\frac{S_{flapped}}{S_{ref}}\right] \tag{3.39}$$

where *c'/c* is the ratio of the original to the extended wing chord.

The increase in maximum attainable lift with different high-lift devices is calculated with an empirically derived formula after Raymer (2012, p.428), cf. Equation (3.40).

$$\Delta C_{L\,max} = 0.9\Delta C_{l\,max}\left(\frac{S_{flapped}}{S_{ref}}\right)\cos\Lambda_{hinge\,line} \tag{3.40}$$

where $\Delta C_{l\,max}$ is the two-dimensional lift increase due to the high-lift device, which can be estimated from Equation (3.41).

$$\Delta C_{l\,max} = \begin{cases} 0.4c'/c & \text{for leading-edge slats} \\ 1.3c'/c & \text{for single-slotted Fowler flaps} \\ 1.6c'/c & \text{for double-slotted Fowler flaps} \end{cases} \tag{3.41}$$

The angle of attack at which the maximum lift occurs is difficult to predict, as it strongly depends on the exact high-lift configuration characteristics. Therefore, no corresponding estimation method could be implemented in the IDT. This is not a severe drawback, however, as an aircraft is normally not operated with maximum lift for safety reasons.

3.3.3.2 High-Lift Effect on Drag

The deployment of high-lift devices has an influence on both zero-lift drag and drag due to lift. Additional parasite drag is estimated as an increment ΔC_{D0} according to Equation (3.42). (Raymer 2012, p.464)

$$\Delta C_{D0} = F_{flap} \frac{c_{flap}}{c} \frac{S_{flapped}}{S_{ref}} \left(\delta_{flap} - 10° \right) \tag{3.42}$$

where F_{flap} is 0.0074 for slotted flaps and c_{flap} is the chord length of the flap. δ_{flap} is the flap deflection angle. 20° for slats and 30° for Fowler flaps in take-off configuration and 60° in landing configuration are assumed as typical values.

High-lift devices also influence drag due to lift, because additional lift occurs in the part of the wing where the flap is present. This affects the spanwise lift distribution and hence induced drag. An approximation of the resulting drag increase is given by Equation (3.43) after Raymer (2012, p.464).

$$\Delta C_{Di} = k_{flap}{}^2 \Delta C_{L\,flap}{}^2 \cos \Lambda_{1/4} \tag{3.43}$$

where k_{flap} is 0.14 for full-span flaps and 0.28 for half-span flaps. This drag increment is added to the drag due to lift calculated with the clean *K*-factor and the total lift.

3.4 Mass Estimation Module

An accurate mass estimation is a crucial part of the aircraft design process as it significantly determines the viability of a concept. The mass estimation module of the IDT contains four mass estimation methods developed by three different authors to allow for comparisons. In the source code of the IDT, the mass estimation is implemented as the first analysis module. However, the calculations of the different estimation methods are performed in separate subfunctions, which are run from the main program.

All the methods were statistically derived through regression analyses by the corresponding authors. The common approach is a breakdown of the aircraft into components. The masses of these are predicted separately on the basis of varying parameters and are then added up to the operating mass empty (OME). The component breakdown varies among the different methods so that component masses cannot be compared directly. Typical accounting differences are the wing-fuselage intersection, retractable landing gear structures or equipment items. The summed up operating masses empty are comparable, however. (Torenbeek 1982, p.275)

Generally, the performed component weight breakdowns are very detailed in order to achieve greater prediction accuracies. However, components can be organized in a "Group Weight Statement" as specified by the Society of Allied Weights Engineers under SAWE-8. This consists of the groupings Structures, Propulsion, Systems / Equipment, and Operational Items. (Raymer 2012, p.579) The output of the IDT mass

estimation methods is arranged in a corresponding way. Additionally, pie charts are created for the different methods that visualize the mass distribution among the weight groups.

A common requirement of the mass prediction methods is that an initial estimate of the aircraft's design maximum take-off mass has to be available in advance. This is necessary, because the MTOM is a main driver of the weight of many single components, e.g., the wing structure or the landing gear. Hence, the initial mass estimate of the aircraft concept to be analyzed is required as an input parameter of the IDT, cf. Appendix B.1. In order to increase the accuracy of the respective weight estimation, it is recommended to iteratively adjust this input value of the initial mass estimate until it matches the result of the desired mass estimation method. The other methods, however, feature a greater error in this case, as all work with the same input parameters.

Raymer (2012, p.595) points out that for new aircraft designs, such as the one evaluated in this work, weight can be significantly reduced by using advanced composite materials instead of aluminum alloys for structural components. This is not accounted for, however, in the equations of the current mass estimation methods, as they are based on the statistics of existing aircraft configurations. Therefore, component-specific "fudge factors" are suggested that have to be multiplied with the respective estimated component mass to include the effect of advanced composites. The respective values of these fudge factors are listed in Table 3.3. Raymer (2012, p.595) presents fudge factors only in the context of his own mass estimation method. However, the other prediction methods after Torenbeek (1982) and Howe (2000) were developed earlier and must therefore be based on an even older group of reference aircraft. Within the scope of this work, fudge factors as in Table 3.3 are thus applied to all mass estimation methods. This also includes Torenbeek's revised method from 2013, as it does not specifically incorporate the effect of modern composites either (cf. Torenbeek 2013, p.237).

Table 3.3: Mass estimation fudge factors to allow for the application of advanced composite materials in structural components of new aircraft designs (Raymer 2012, p.595)

Advanced composite mass estimation fudge factors	
Fuselage	0.9
Wing	0.85
Horizontal and vertical tail	0.83
Landing gear	0.95
Nacelles	0.9

Each of the mass estimation methods employed in the IDT involves extensive calculations. Therefore, the author refrains from presenting each equation in this thesis and only references to the corresponding sources are given. Still, the following sections contain descriptions of the different methods, as especially the level of detail of the component breakdowns and the considered numbers of parameters vary greatly among the different methods.

3.4.1 Aircraft Statistical Weights Estimation Method after Raymer (2012)

Raymer's mass estimation method is based on a statistical regression analysis, but includes some physics-based models. The equations for cargo / transport aircraft can be found in Raymer (2012, p.589). The approach features a comparably detailed breakdown of components and systems and requires a relatively great number of parameters.

As the only one of the mass estimations implemented in the IDT, this method specifically addresses the topic of weight growth. On the basis of a statistical analysis, Raymer (2012, p.596) shows that it is common for produced aircraft to be heavier than the respective projected weight. Therefore, he suggests increasing the result of his empty mass estimation by 5% in order to account for this effect.

3.4.2 Empty Weight Prediction Method after Torenbeek (1982)

In his work from 1982, Torenbeek presents several ways of estimating the aircraft empty mass with a varying level of detail. In a simplistic approach, the total airframe structural mass is estimated with the concept of an aircraft specific density, i.e., the aircraft mass divided by its volume. (Torenbeek 1982, p.277) With just the fuselage dimensions and the desired load factor, an initial mass estimate can be derived with this method.

Additionally, a 'simple' estimation method is introduced, featuring a basic component breakdown and a limited number of parameters. The 'detailed' method includes an exhaustive component breakdown going as far as escape hatches or speed brakes. (Torenbeek 1982, p.451 and p.457) This is the most detailed of all mass estimation methods implemented in the IDT. However, Torenbeek points out that a greater number of input parameters does not generally increase the prediction accuracy, which he specifies with 5% to 10% standard error for his simple method. (Torenbeek 1982, p.275) Still, the detailed method provides the possibility to consider special features of an aircraft concept, e.g., the two-deck cabin layout of the concept analyzed in this work.

3.4.3 Transport Empty Weight Prediction Method after Torenbeek (2013)

Interestingly, the recent work of Torenbeek (2013) contains only one comparably basic mass prediction method with a standard component breakdown. Contrary to the detailed method presented in 1982, special features of the aircraft concept to be analyzed cannot be considered. Furthermore, Torenbeek states that his newly proposed equations should be verified with "in-house information." (Torenbeek 2013, p.234)

3.4.4 Mass Prediction Method after Howe (2000)

The basic 'simple' mass estimation method after Howe is the simplest one implemented in the IDT, requiring the least number of parameters, yet featuring a standard component breakdown. The corresponding equations are given in Howe (2000, p.153). Additionally, a more refined 'detailed' method is available at Howe (2000, p.339). This is based on a more detailed component breakdown. However, its set of equations still takes less aircraft features into account than the methods after Raymer (2012) and Torenbeek (1982).

3.5 Propulsion Modeling Module

In terms of aircraft propulsion, the IDT comprises a turboprop engine model, cf. Section 3.1.2. This covers the characteristics of turbine and propeller throughout the operating range. Parameters that need to be determined are the available turbine power with the corresponding fuel consumption, the propulsive efficiency of the propeller that is strongly affected by the flight speed in relation to the propeller's rotational speed, and the achievable thrust that advances the aircraft.

The engine that was chosen for the high-capacity short- to medium-range aircraft concept investigated in this work is based on the propulsion system of the Antonov An-70, cf. Appendix A.3. Still, deviating requirements would make a reengineering or even a redesign of the engine necessary. As sufficient data about the Antonov's engine were not available anyway, a generic description of the engine characteristics was derived by Iwanizki (2013, p.51).

The propulsion model implemented in the IDT is based on the work of Iwanizki and is a combination of general aircraft design practices, as can be found in literature, and empirical data. The following sections give detailed descriptions of the different aspects.

3.5.1 Available Engine Power

In the case of turboprop engines, one must generally distinguish between shaft and equivalent power. Shaft power is mechanically transmitted via the shaft of the engine and used to drive the propeller. Yet, in addition to the propeller, also the exhaust gases of the turbine engine contribute to forward thrust. This additional thrust is converted to an additional power and included in the equivalent engine power, which is thus commonly about 5% to 10% greater than the shaft power. (Torenbeek 1982, p.118; Bräunling 2009, p.494) From an aircraft design perspective, only the total attainable thrust is of interest and hence, the following considerations concern equivalent power.

Starting from a specified static equivalent engine power rating at MSL (cf. Appendix B.7), the purpose of the engine power model is to estimate the power that the engine delivers as a function of flight speed and altitude. Major influences that need to be considered are the ram effect that increases the turbine's overall pressure ratio and thus its power with growing flight speed and, moreover, the gradually decreasing air density at higher operating altitudes, which reduces engine power.

Nicolai and Carichner (2010, p.803) have published an engine power diagram for an Allison 501-M7 (T56-A-15) turboprop engine, which is the power plant of the Lockheed C-130H Hercules. With a regression analysis of this diagram, Iwanizki (2013, p.51) derived an analytic model for the equivalent shaft power as a function of flight Mach number and ambient air density with Equations (3.44) and (3.46).

$$P_{eq} = P_{eq,MSL}\sigma^{0.82}\left(1 + aM^{2.1}\right) \tag{3.44}$$

with

$$\sigma = \frac{\rho}{\rho_{MSL}} \tag{3.45}$$

$$a = -\frac{0.074}{\sigma} + 0.8787 \tag{3.46}$$

where ρ is the air density and σ is the relative density referenced to MSL. At low altitudes, the increase in engine power due to ram effects is limited by the maximum torque that the engine components can withstand. According to the source data of Nicolai and Carichner, at MSL, a power increase of roughly 10% is attainable before torque limits are reached. Unlike this, however, Iwanizki does not account for ram effects at MSL and limits engine power to the specified static value, cf. Figure A.2 a). Nonetheless, Iwanizki's engine power model is adopted in the IDT and initially remains unchanged. It is implemented in the subfunction 'engine_power.m.'

3.5.2 Engine Fuel Consumption

In accordance with the concept of equivalent power, the fuel consumption of a turboprop engine is expressed as equivalent power specific fuel consumption ESFC, as it is defined in Equation (3.47). (Howe 2000)

$$ESFC = \frac{\dot{m}_{fuel} g}{P_{eq}} \tag{3.47}$$

where $\dot{m}_{fuel}$ is the fuel mass flow rate and g the gravitational acceleration.

Iwanizki applied a constant value of the ESFC. (Iwanizki 2013, p.112; Randt 2014b, p.6) Data of the Allison 501-M7 (T56-A-15) provided correspondingly to the above-mentioned power characteristics by Nicolai and Carichner (2010, p.803) show, however, that specific fuel consumption varies considerably, cf. Figure 3.4.

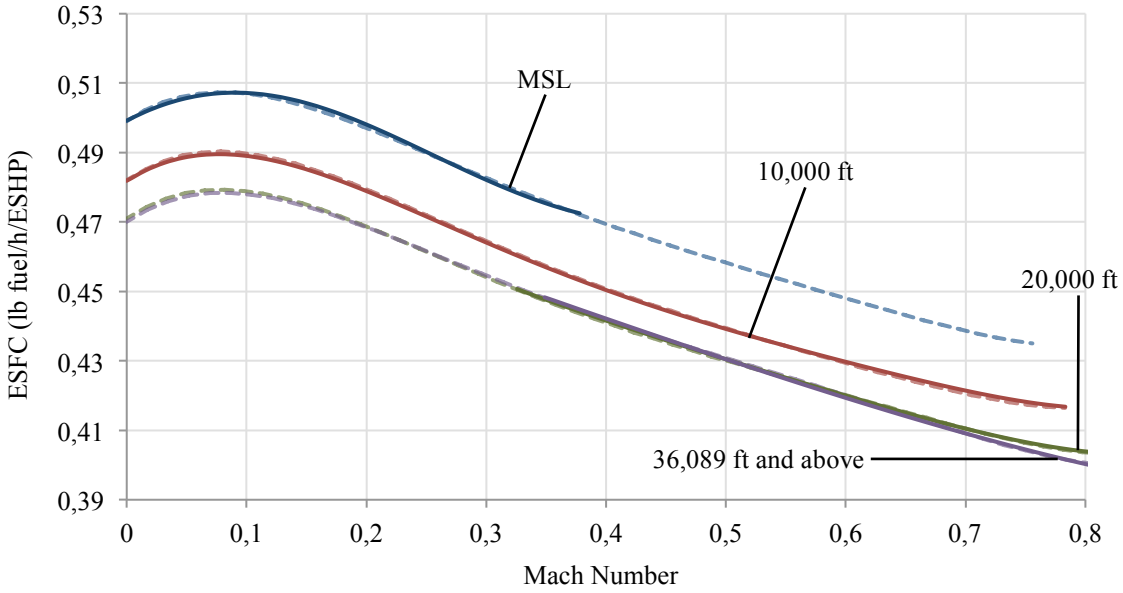

Figure 3.4: Equivalent specific fuel consumption characteristics of the Allison 501-M7 (T56-A-15) turboprop engine, source data after Nicolai and Carichner (2010, p.803) for different flight altitudes (solid lines) and corresponding curves of the developed model (dashed lines)

Within the scope of this work, a model for the fuel consumption characteristics is developed through a regression analysis, as shown in Figure 3.4. A fifth-order polynomial is applied to describe the change of fuel consumption with flight Mach number, cf. Equation (3.48). The coefficients of this polynomial are in turn specified with polynomials of third order, see Equations (3.49) to (3.54), and describe the influence of the flight altitude, i.e., the relative ambient air density.

$$ESFC = k_5 M^5 + k_4 M^4 + k_3 M^3 + k_2 M^2 + k_1 M + k_0 \tag{3.48}$$

with

$$k_0 = -0.1236\sigma^3 + 0.3054\sigma^2 - 0.1837\sigma + 0.5008 \tag{3.49}$$

$$k_1 = 0.238 \tag{3.50}$$

$$k_2 = 0.0643\sigma^3 + 0.0637\sigma^2 - 0.1888\sigma - 1.9672 \tag{3.51}$$

$$k_3 = 4.97 \tag{3.52}$$

$$k_4 = 1.6823\sigma^3 - 4.0466\sigma^2 + 2.9368\sigma - 6.1504 \tag{3.53}$$

$$k_5 = -2.3003\sigma^3 + 5.051\sigma^2 - 3.3365\sigma + 2.9737 \tag{3.54}$$

An additional offset allows for an adjustment of the absolute values of the specific fuel consumption to a desired level. Initially, this offset is specified so that Iwanizki's value for the fuel consumption in design cruise flight conditions is matched. (Iwanizki 2013, p.112) The above equations are implemented in the IDT as subfunction 'engine_fuel_consumption.m.'

3.5.3 Propulsive Efficiency of the Propeller

The propulsive efficiency quantifies the capability of the propeller to convert the shaft power delivered by the engine into thrust exerted on the aircraft. Propeller efficiency is difficult to predict, as it is affected by numerous influences of the propeller, engine, and aircraft configuration. Nonetheless, a reasonable estimation of the propeller efficiency is crucial to realistic aircraft performance and fuel efficiency predictions.

Best practice in aircraft design is to obtain experimental propeller data from the propeller manufacturer. (Raymer 2012, p.499) For the investigated high-capacity aircraft concept, however, no specific propeller is available to be taken off the shelf and sufficient data of comparable propellers, such as the Aerosila SV-27 (AEROSILA 2005) of the Antonov An-70 or the Ratier-Figeac FH385/386 (EASA 2013) of the Airbus A400M, are not accessible.

Instead, an estimation of the efficiency that is achievable with a generic propeller is carried out in a multistage process as suggested by Iwanizki (2013, p.52). Generally, the propeller efficiency is strongly dependent on the advance ratio *J*, which is defined in Equation (3.55).

$$J = \frac{V}{nD_P} \tag{3.55}$$

where n is the rotational speed of the propeller, for which a reasonable value has to be adopted. The product (nD_P) is limited by the tip Mach number and noise considerations.

According to Howe (2000, p.68), typical values for unducted propellers lie in the range of 60 m/s to 100 m/s, where the lower value applies to larger aircraft such as the high-capacity concept of this work. Hence, a value of 60 m/s for (nD_P) is implemented in the IDT so that the rotational speed of the propeller can be calculated with the specified propeller diameter, cf. Appendix B.7. As transport aircraft with turboprop engines are generally fitted with constant-speed propellers, variation of rotational speed does not need to be considered. (Torenbeek 1982, p.196)

Before the propeller efficiency can be calculated, the advance ratio as in Equation (3.55) must be corrected for blockage. (Raymer 2012, p.499) Because in a puller configuration, the nacelle is directly behind the propeller, it blocks the airflow and slows it down already before it reaches the propeller. This effect can be accounted for by adjusting the advance ratio according to Equation (3.56).

$$J_{corrected} = J\left(1 - 0.329\frac{S_{nacelle}}{D_p}\right) \tag{3.56}$$

where $S_{nacelle}$ is the maximum cross section of the nacelle directly behind the propeller plane.

With this corrected advance ratio, the achievable propeller efficiency is estimated with the following equations after Howe (2000, p.68):

For $0.4 \le J_{corrected} < 1.0$:

$$\eta = 0.82 J_{corrected}^{\ 0.4} \tag{3.57}$$

For $1.0 \le J_{corrected}$:

$$\eta = \frac{0.82 J_{corrected}^{\ 0.16}}{10^{j}} \tag{3.58}$$

with

$$j = 0.3\left(\log J_{corrected}\right)^{2.4} \tag{3.59}$$

Additionally, Howe points out that the achievable efficiency is sometimes limited by Equation (3.60), which is implemented in the IDT accordingly.

$$\eta_{LIMIT} = 1.8\rho z_P^{\ 0.15}\left(nD_P\right)^{3.7} J_{corrected} P_{MSL}^{\ 0.095} \times 10^{-7} \tag{3.60}$$

where z_P is the number of propeller blades and P_{MSL} the static shaft power rating of the engine.

Once a value for the propeller efficiency according to Equations (3.57) to (3.60) has been calculated, another correction is imposed. As mentioned above, due to noise considerations, the propeller rotational speed is chosen dependent on the diameter so as to enable low tip speeds. Still, especially for high-speed aircraft, the helical blade tip speed approaches the speed of sound in fast flight. The increased drag due to the formation of shocks at the propeller tips reduces thrust and increases the torque on the engine. The resulting deterioration of the propeller efficiency is modeled with Equation (3.61) after Raymer (2012, p.500).

For $M_{tip} > 0.89$:

$$\eta_{corrected} = \eta - \left(M_{tip} - 0.89 \right) \left(\frac{0.16}{0.48 - 3\left(t/c \right)_P} \right) \tag{3.61}$$

with

$$M_{tip} = \sqrt{V^2 + \left(\pi n D_P \right)^2} \Big/ a \tag{3.62}$$

where $(t/c)_P$ is the thickness-to-chord ratio of the propeller blade, for which a typical value of 0.06 is employed in the IDT, and a the speed of sound.

A third correction is to be considered for propeller efficiency estimation, the influence of scrubbing drag. The higher velocity and turbulence level of the propeller slipstream increase the drag experienced by aircraft components in propwash. Again, the propeller efficiency is adjusted to account for this effect as in Equation (3.63). (Raymer 2012, p.500)

$$\eta_{effective} = \eta_{corrected} \left[1 - \frac{1.558}{{D_P}^2} \frac{\rho}{\rho_{MSL}} \sum \left(C_{fe} S_{wet} \right)_{propwash} \right] \tag{3.63}$$

where C_{fe} is the equivalent skin-friction parasite drag coefficient and S_{wet} the corresponding wetted area of the aircraft components in propwash. Both values have already been determined in the context of predicting zero-lift drag with the component buildup method, cf. Section 3.3.2.1.

The process of estimating the propeller efficiency as described above is implemented in the IDT in the subfunction ‘propeller_efficiency.m.’

3.5.4 Achievable Thrust

When available engine power and propeller efficiency have been determined, the achievable thrust in a given flight condition with velocity V is calculated with Equation (3.64).

$$T = \frac{P_{eq}\eta_{effective}}{V} \tag{3.64}$$

A problem arises, though, when static thrust is of interest, because Equation (3.64) features a singularity for V equal to zero. According to Mattingly et al. (2002, p.607), a reasonable assumption to solve this issue is that for Mach numbers below 0.1 propeller thrust is taken to be equal to the thrust at $M = 0.1$, cf. Figure 3.5. This approach is implemented in the IDT.

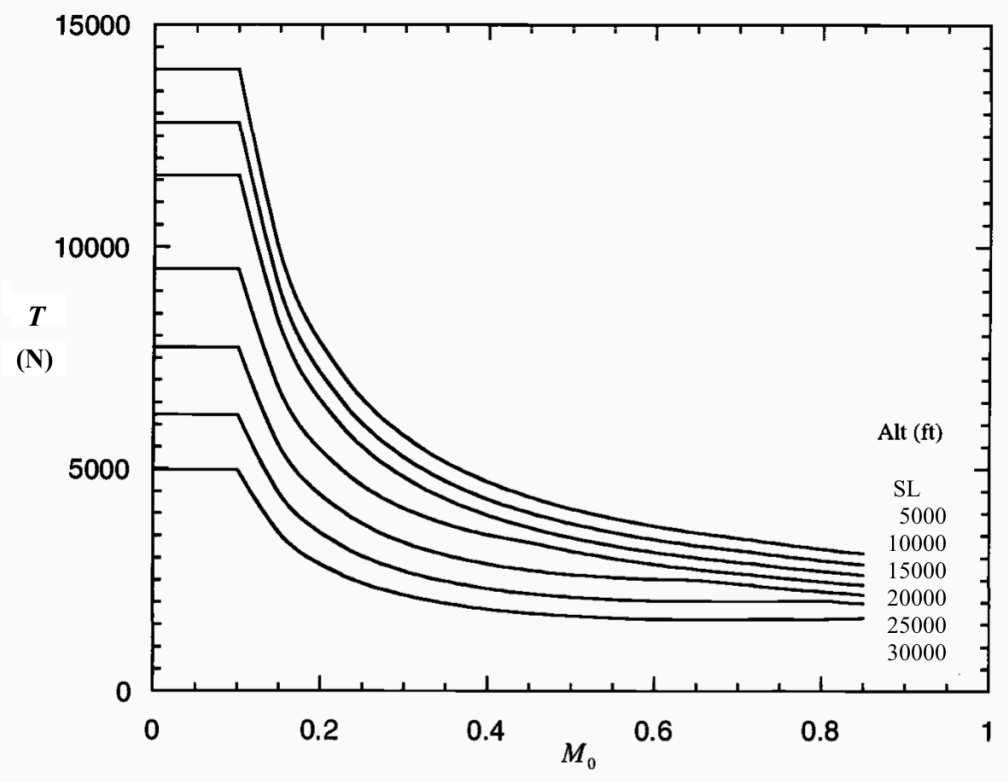

Figure 3.5: Exemplary turboprop thrust characteristic with thrust assumed constant below a Mach number of 0.1, adapted from Mattingly et al. (2002, p.607)

4 Recalculation of the Baseline Aircraft Concept Properties and Performance

The integrated design tool, described in Chapter 3, is applied to the baseline high-capacity short- to medium-range aircraft concept Propcraft P-420/A as presented in Chapter 2. By this, the proposed design is analyzed, previously estimated parameters are reviewed and recalculated.

The following sections cover the results of the various analyses performed by the IDT. Additionally, the aircraft performance module of the IDT is introduced that combines results of the other modules in order to derive statements on the achievable flight and mission performance. This enables an examination of the compliance of the concept with specified design requirements and the identification of critical design aspects.

4.1 Estimated Aerodynamic Characteristics

In the following, lift, drag, and high-lift characteristics of the baseline Propcraft P-420/A concept are presented that were elaborated with the methods presented in Section 3.3.

4.1.1 Lift Curve

To determine the lift curve of the aircraft, initially, two-dimensional airfoil characteristics are required as input parameters of the IDT, cf. Appendix B.2.

4.1.1.1 Two-dimensional Airfoil Lift

The tool XFOIL (Drela and Youngren 2013) is used to perform an aerodynamic analysis of the wing airfoil. XFOIL is an analysis and design tool for subsonic airfoils. Based on a specified airfoil shape, it applies a high-order panel method, taking Reynolds and

Mach number effects into account. The influences of viscosity, including transition and separation are also incorporated.

XFOIL is applied to the NACA SC(2)-0714 airfoil, that was selected for the wing by Iwanizki (2013, p.76). The design conditions of slow and low flight (Mach number 0.2 at MSL) and of cruise flight (Mach number 0.64 at FL290) are investigated separately with the corresponding Reynolds numbers. Figure 4.1 shows the predicted aerodynamic characteristics of the airfoil and Table 4.1 lists the corresponding parameters.

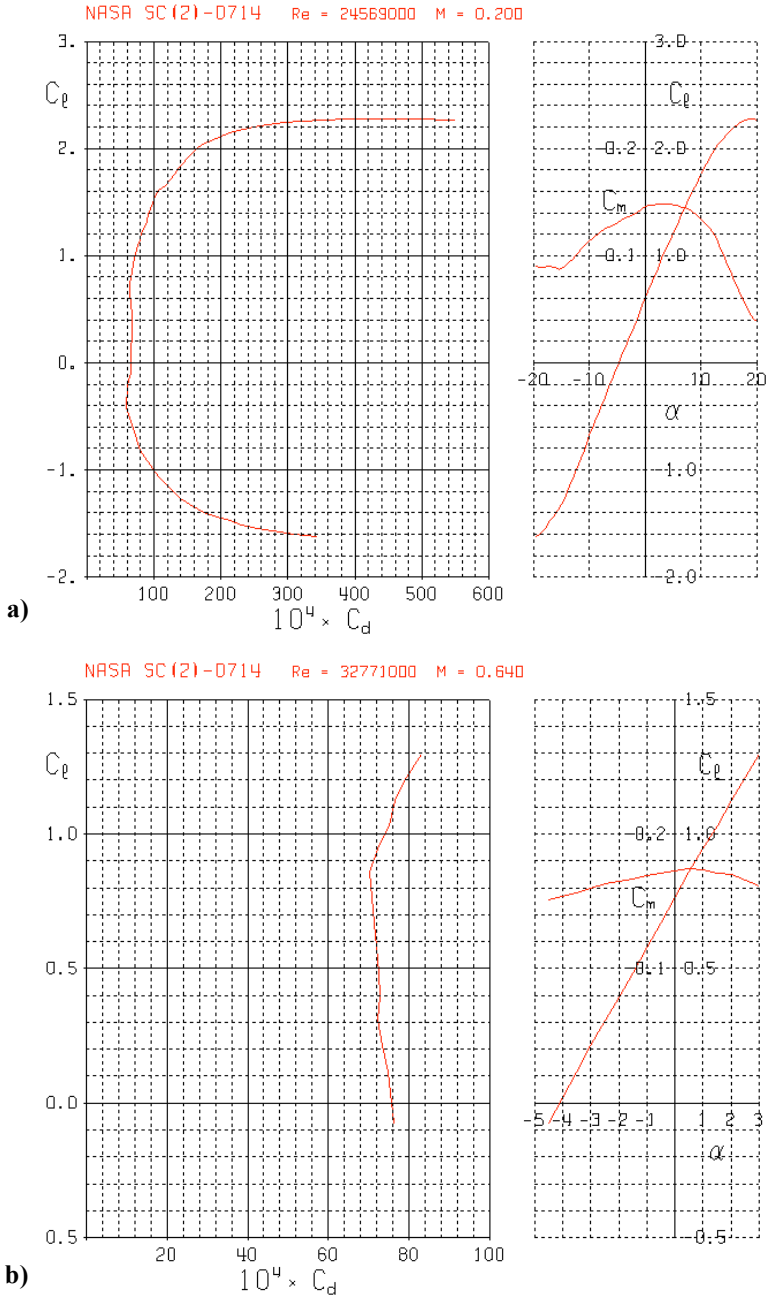

Figure 4.1: NASA SC(2)-0714 Airfoil aerodynamic characteristics in design conditions for slow and low flight (a) as well as cruise flight (b), determined with XFOIL (Drela and Youngren 2013)

Table 4.1: NASA SC(2)-0714 Airfoil aerodynamic parameters in design conditions for slow and low flight as well as cruise flight, determined with XFOIL (Drela and Youngren 2013)

Airfoil aerodynamic parameters	Slow and low flight,	Cruise flight
Mach number [-]	0.2	0.64
Reynolds number [-]	24.569×10^6	32.771×10^6
Zero-lift angle of attack [°]	-4.75	-4.15
Lift-curve slope [1/rad]	7.1734	10.4679
Maximum lift coefficient [-]	2.27	–

4.1.1.2 Aircraft Lift

From the two-dimensional lift-curve slope, the one of the aircraft is calculated with Equation (3.2) after Lowry and Polhamus (1957). Because this equation is dependent on the Mach number, a difference between the values for slow, low and for cruise flight persists. As mentioned in Section 3.3.1, zero-lift angles of attack of the wing are considered equal to the ones of the airfoil. The maximum attainable lift coefficients and the corresponding angles of attack for the two flight conditions are estimated with Equations (3.6) and (3.7), respectively. With these values the lift curves can be drawn from zero lift to maximum lift, which is shown in Figure 4.2 for slow and low flight in green and cruise flight in purple. Table 4.2 contains the corresponding numerical values.

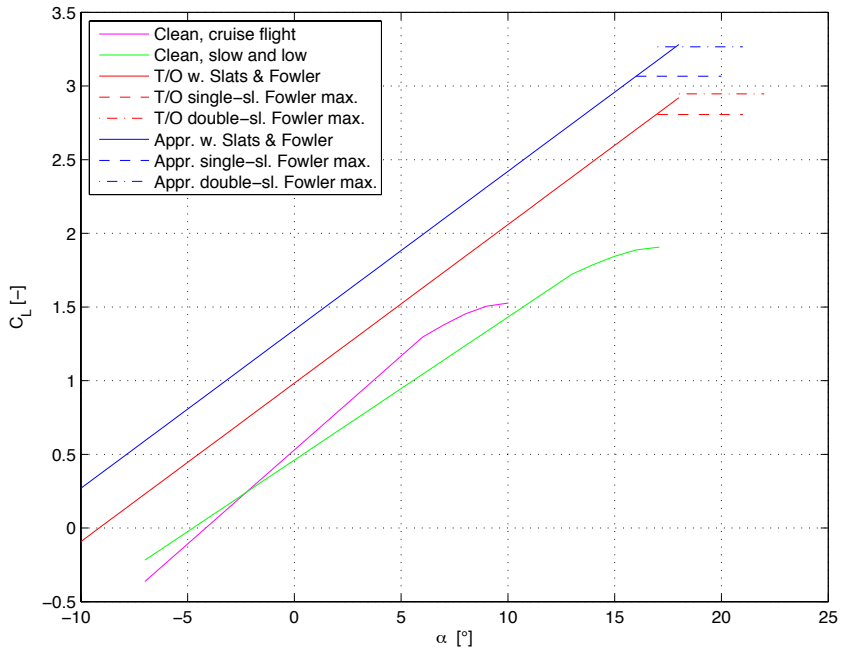

Figure 4.2: Lift curves of the baseline Propcraft P-420/A concept, clean configuration in slow and low flight (green) and in cruise flight (purple), with slats and Fowler flaps in take-off setting (red) and in approach setting (blue), maximum-lift level for single-slotted Fowler flaps (dashed) and for double-slotted Fowler flaps (dash-dotted)

4.1.1.3 High Lift

High-lift characteristics are considered for leading-edge slats and single- or double-slotted Fowler flaps, cf. Section 3.3.3. As these are extending high-lift devices, the lift-curve slope changes according to Equation (3.39). Furthermore, the zero-lift angle of attack is shifted towards more negative values depending on the grade of flap deployment, i.e., take-off or approach setting (cf. Figure 4.2 and the numerical values in Table 4.2). The maximum attainable lift with deployed high-lift devices is determined with Equation (3.40), but the IDT does not predict the angle of attack at which it occurs, cf. Section 3.3.3.1. Therefore, Figure 4.2 depicts the maximum lift with horizontal dashed and dash-dotted lines that resemble the expectable maximum angle-of-attack range for single- and double-slotted Fowler flaps, respectively. Within the scope of the modeling performed with the IDT, the configurations with single- and double-slotted Fowler flaps yield the same lift curve and differ only in the value of the maximum attainable lift.

Table 4.2: Lift curve parameters of the baseline Propcraft P-420/A concept, clean configuration in slow and low flight, in cruise flight, with slats and single-slotted as well as double-slotted Fowler flaps in take-off setting and in approach setting

Aircraft aerodynamic parameters	Clean, slow and low	Clean, cruise	High-lift, take-off	High-lift, approach
Zero-lift angle of attack [°]	-4.75	-4.15	-9.141	-12.503
Lift-curve slope [1/rad]	5.56	7.309	6.163	6.163
Maximum lift coefficient [-]	1.907	1.527	Single-sl.: 2.806 Double-sl.: 2.946	Single-sl.: 3.066 Double-sl.: 3.266
Maximum angle of attack [°]	17.1	10.02	–	–

4.1.1.4 Neglect of Propeller Effect on Lift

With Equation (3.8) after Roskam, the effect of the propeller slipstream on wing lift is estimated. As this equation is proportional to the lift coefficient the wing is operated with, it contributes little in cruise flight, but has a strong effect on the maximum attainable lift. When applied to the baseline Propcraft P-420/A concept, the equation yields increments in lift coefficient of around three for take-off and landing configuration (Table 4.3). Combined with the maximum lift coefficients stated in Table 4.2, this basically doubles lift and results in total lift coefficients of around six. For a transport aircraft, this value seams unrealistically high, especially as it can be found in literature that “maximum lift coefficients can range to as much as 5.0 for a wing with large flaps immersed in the propwash” (Raymer 2012, p.127) and it is not intended for the investi-

gated concept to be equipped with particularly large flaps. Howe (2000, p.142) points out that the propeller slipstream effect may increase lift by some 15% to 20%, but not double it. Neither Raymer nor Howe, however, provides a method or equation to incorporate the effect into conceptual aircraft design. In the absence of a suitable method, the propeller slipstream effect on lift is thus neglected in the IDT. One has to acknowledge, though, that in reality, an effect should be observable, especially as a relatively large part of the wing of the investigated concept is affected by the propeller slipstream.

Table 4.3: Propeller slipstream effect on the lift coefficient of the baseline Propcraft P-420/A concept, clean configuration in cruise flight, with slats and single-slotted as well as double-slotted Fowler flaps in take-off setting and in approach setting

Propeller slipstream effect on lift	Clean, cruise	High-lift, take-off	High-lift, approach
Lift coefficient increment in design cruise flight [-]	0.017	–	–
Increment in maximum attainable lift coefficient [-]	–	Single-slotted: 2.669 Double-slotted: 2.802	Single-slotted: 2.916 Double-slotted: 3.106

4.1.2 Drag Polar

Drag analysis consists of the prediction of zero-lift drag and of drag due to lift, cf. Section 3.3.2. Combining the two yields, the total drag and enables the creation of the drag polar as shown in Figure 4.3 for the baseline Propcraft P-420/A concept. The following sections deal with the different aspects of it. The concept complies with the subsonic-flight-regime constraint as described in Section 3.3.2.3, as the drag-divergent Mach number is predicted with 0.7 and nominal operation occurs at lower velocities.

4.1.2.1 Zero-Lift Drag

Three different methods are applied to estimate zero-lift drag, two of which feature a Mach number dependency, cf. Section 3.3.2.1. Table 4.4 lists the results.

Table 4.4: Zero-lift drag of the baseline Propcraft P-420/A concept, predicted with the equivalent skin-friction method, the component buildup method, and the method after Howe

Zero-lift drag coefficient	Clean, slow and low	Clean, cruise
Equivalent skin-friction method	0.0165	0.0165
Component buildup method	0.0251	0.0196
Method after Howe	0.0237	0.0218

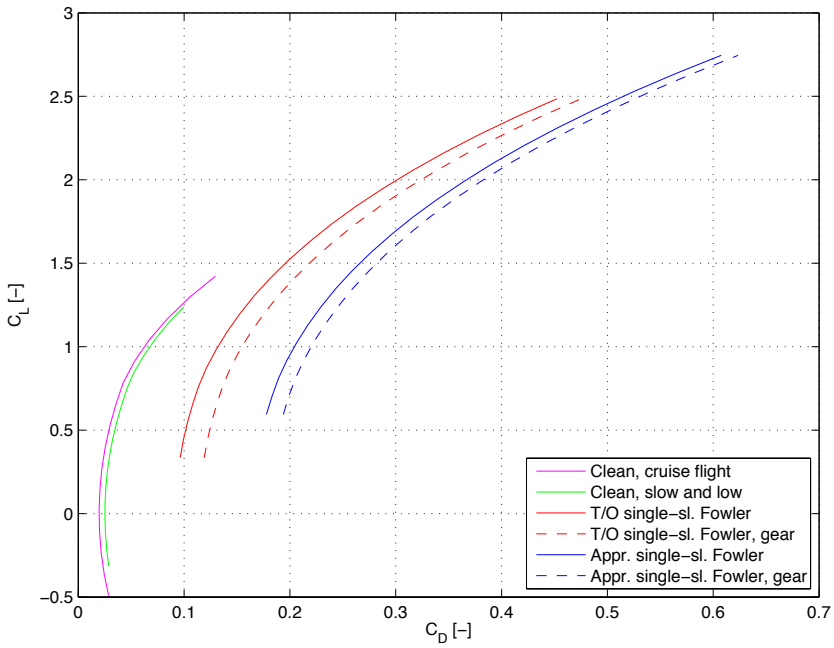

Figure 4.3: Drag polars of the baseline Propcraft P-420/A concept, clean configuration in slow and low flight (green), in cruise flight (purple), with slats and single-slotted Fowler flaps in take-off setting (red) and in approach setting (blue), additionally with deployed landing gear (dashed)

It can be observed that the rudimentary equivalent skin-friction method predicts a lower value than the component buildup method and the method after Howe. The latter two match comparably well, however. Only the influence of the Mach number is slightly lower in the method after Howe, but both predict a higher zero-lift drag in the slow and low flight condition compared to cruise flight. Due to the good accordance of the results of these two methods, the so-obtained value range is considered realistic within the scope of the modeling of the IDT. As the component buildup method accounts in more detail for the characteristics of the investigated concept, it is selected for all further calculations and its results are utilized in Figure 4.3.

Table 4.5: Zero-lift drag increments of special items of the baseline Propcraft P-420/A concept, landing gear drag after Raymer and after Mair and Birdsall as a function of high-lift devices setting, drag of speed brakes and of one inoperative feathered engine

Zero-lift drag coefficient increment of special items	Clean	High-lift, take-off	High-lift, approach
Landing gear (after Raymer)	0.0273	–	–
Landing gear (after Mair and Birdsall)	0.0294	0.0227	0.0160
Wing mounted speed brakes	0.1763	–	–
One engine inoperative (feathered)	0.0044	–	–

Additional drag increments of special items are given in Table 4.5. Due to its dependency on the flap setting, the landing gear drag estimation after Mair and Birdsall is employed in further calculations. Comparisons with the result after Raymer and literature values (0.03 after Howe (2000, p.150) or 0.015 to 0.02 after Torenbeek (1982, p.165)) show that the obtained values are reasonable.

4.1.2.2 Drag due to Lift

The prediction of drag due to lift is essentially a question of finding an accurate drag-due-to-lift factor, cf. Section 3.3.2.2. Four estimation methods are executed for comparison purposes, of which only the most refined leading-edge-suction method features a dependency on the lift coefficient, cf. the results in Table 4.6.

Table 4.6: Drag-due-to-lift factor of the baseline Propcraft P-420/A concept, predicted with the statistical Oswald span efficiency method, the method after Howe, the method after Nita and Scholz and the leading-edge-suction method

Drag-due-to-lift factor		
Statistical Oswald span efficiency method		0.0559
Method after Howe: Slow and low flight		0.0391
Cruise flight		0.0394
Method after Nita and Scholz: Slow and low flight		0.0404
Cruise flight		0.0383
Leading-edge-suction method:		
Slow and low flight	at or below design lift coefficient	0.0373
	at maximum lift coefficient	0.0658
On runway in ground effect	at or below design lift coefficient	0.0186
	at maximum lift coefficient	0.0328
Cruise flight	at or below design lift coefficient	0.0373
	at maximum lift coefficient	0.0572

Firstly, comparison among the results of the different methods shows similar value ranges, which is again an indicator for the general accuracy of the prediction. The methods after Howe and after Nita and Scholz yield very similar results and a weak influence of the Mach number. The leading-edge-suction method gives comparable results for operation at or below the design lift coefficient. However, when higher lift coefficients occur, the drag-due-to-lift factor increases significantly as the drag polar deviates from a purely parabolic shape. Here the K-factor almost doubles from design lift to maximum lift coefficient in both slow, low and cruise flight. Additionally, values for operation on the ground are given, where the ground effect reduces drag due to lift

considerably. As explained in Section 3.3.2.2, within the scope of the methods employed in this work, the leading-edge-suction method is considered most accurate and is thus selected for the calculation of the drag polars in Figure 4.3 as well as for the further calculations.

4.1.2.3 Drag of High-Lift Devices

Deployed high-lift devices contribute to both zero-lift drag and drag due to lift, cf. Section 3.3.3.2. Within the scope of the modeling applied with the IDT, drag increments are identified as tabulated in Table 4.7.

Table 4.7: Drag increments due to deployed high-lift devices of the baseline Propcraft P-420/A concept, additional zero-lift drag and drag due to lift for take-off and approach setting of the high-lift devices

Drag increments due to deployed high-lift devices	Take-off setting	Approach setting
Slats and single-slotted Fowler flaps:		
Zero-lift-drag increment	0.0375	0.0811
Drag-due-to-lift increment	0.0295	0.0584
Slats and double-slotted Fowler flaps:		
Zero-lift-drag increment	0.0375	0.0811
Drag-due-to-lift increment	0.0438	0.0877

It can be observed that the configuration with double-slotted Fowler flaps causes roughly double the drag of the single-slotted variant. However, within the scope of the performed lift analysis, double-slotted Fowler flaps only produce more lift at angles of attack that exceed the maximum angle reached with single-slotted Fowler flaps. As the aircraft is normally not operated at such high angles of attack, the double-slotted configuration has no benefit within this modeling. Therefore, the configuration with single-slotted Fowler flaps is selected for the further investigations and Figure 4.3 contains only the corresponding drag polars. This conclusion is in accordance with a currently observable trend towards more simple single-slotted high-lift systems for modern airliners (e.g., Airbus A380, Boeing 787, Airbus A350), cf. Rudolph (1996, p.137).

4.1.3 Aerodynamic Performance

On the basis of the carried out lift and drag predictions, statements about the aerodynamic performance of the aircraft concept can be derived. In the design cruise flight condition with a design lift coefficient of 0.7, a total drag coefficient of 0.038 is reached. This yields an aerodynamic efficiency L/D in cruise flight of 18.47. In relation

to existing propeller aircraft, which have lift to drag ratios of around 15, this value could be considered ambitious. However, modern transport aircraft feature aerodynamic efficiencies of around 20 and hence, the predicted value is realistic for the investigated transport aircraft concept. (Torenbeek 2013, p.47; Raymer 2012, p.39)

Aerodynamic performance at take-off is analyzed at the maximum safe angle of attack on the ground, which is set to 8°. This leaves a safety margin of 3° to the rotation angle of 11°, at which tail strike occurs, cf. Figure 2.3. In a take-off configuration with single-slotted Fowler flaps, a lift coefficient of 1.84 is attained at a drag coefficient of 0.2. The resulting aerodynamic efficiency at take-off is 9.22, which is a reasonable value for transport aircraft according to Gilman Jr. (1953, p.9).

For an evaluation of aerodynamics during approach and landing, the extreme case of a landing with maximum take-off mass is assumed. According to certification specifications, the approach is performed with 1.3 times the stall speed, while touchdown on the runway occurs at 1.15 times the stall speed. These values will be discussed further in the detailed landing analysis in Section 4.4. Under those assumptions, an approach with high-lift devices in approach setting requires a lift coefficient of 1.81, which accords to an angle of attack of 4.36°. A drag coefficient of 0.34 and with this an L/D-ratio of 5.33 is reached. At touchdown, the lower speed makes a lift coefficient of 2.32 and a corresponding angle of attack of 9.05° necessary. Even in this hypothetical situation of a landing with maximum take-off mass, the touchdown angle of attack is feasible, as it leaves a 2° margin to the tail strike. Due to the ground effect, drag at touchdown is reduced to a coefficient of 0.325 and the aerodynamic efficiency increases to 7.125. However, in this situation, speed brakes would be deployed to increase drag.

4.2 Predicted Mass and its Distribution

The mass prediction of the baseline Propcraft P-420/A concept is carried out with the different methods after Raymer, Torenbeek, and Howe, cf. Section 3.4. For each of the methods, the initial estimate of the maximum take-off mass is iteratively adjusted until it matches the respective estimated mass, thus gaining maximum accuracy from the prediction methodology.

Table 4.8 provides an overview of the basic results. As explained in Section 3.4, only the summarized operating mass empty or the maximum take-off mass are comparable, as mass breakdowns may differ among the methods. The fudge factors that are listed in Table 3.3 are applied to all methods alike.

Table 4.8: Mass prediction of the baseline Propcraft P-420/A concept, methods after Raymer, Torenbeek and Howe, fudge factors for advanced composites applied, results iterated for each method respectively

Aircraft mass prediction method after: All values in [kg]	**Raymer (2012)**	**Torenbeek (1982)**		**Torenbeek (2013)**	**Howe (2000)**	
		simple	**detailed**		**simple**	**detailed**
Structure	35,396	45,256	44,148	44,598	36,176	34,316
Propulsion	11,395	17,916	22,373	21,353	21,196	21,196
Systems	11,225	28,958	24,289	16,882	32,395	22,542
Miscellaneous	2,901	–	963	–	–	798
Operational items	–	–	5,531	14,990	5,890	5,890
Operating mass empty	60,917	92,130	97,305	97,823	95,656	84,741
Design passenger payload	———	———	———	42,000	———	———
Design cargo payload	———	———	———	5,000	———	———
Design fuel	———	———	———	27,900	———	———
Maximum take-off mass	136,817	167,030	172,205	172,723	170,556	159,641

Considerable differences in the predicted operating mass empty can be observed among the different methods. The values range from about 61 tons to 98 tons, while the maximum take-off masses vary correspondingly from roughly 137 tons to 173 tons. To explain where this great variation comes from and which method can be considered most realistic, the individual characteristics of each one are examined in the following.

4.2.1 Raymer's Mass Estimation

The mass predicted with Raymer's method is the lowest of all. Several reasons can be identified, however, because of which one can expect that in this case the real mass will be higher than the predicted one. Firstly, the estimation of the structural mass of the fuselage does not take the double-deck configuration into account, but is mainly based on the initial estimate of the maximum take-off mass and the wetted area of the fuselage that is relatively low, because of the double-deck layout. As a result, the fuselage structure mass is underpredicted. Furthermore, the propulsion group mass estimation does not adequately allow for the peculiarities of a turboprop engine. These are only taken into account with a correction factor of 1.4, multiplied with the engine mass. However, this cannot be considered sufficient for propeller, installation, gearbox and other additional systems. Finally, the estimation of the mass of cabin furnishings (part of 'Systems' in Table 3.3) does again not consider the double-deck layout, as it is only based on the parameters fuselage wetted area, cargo weight, and number of crew.

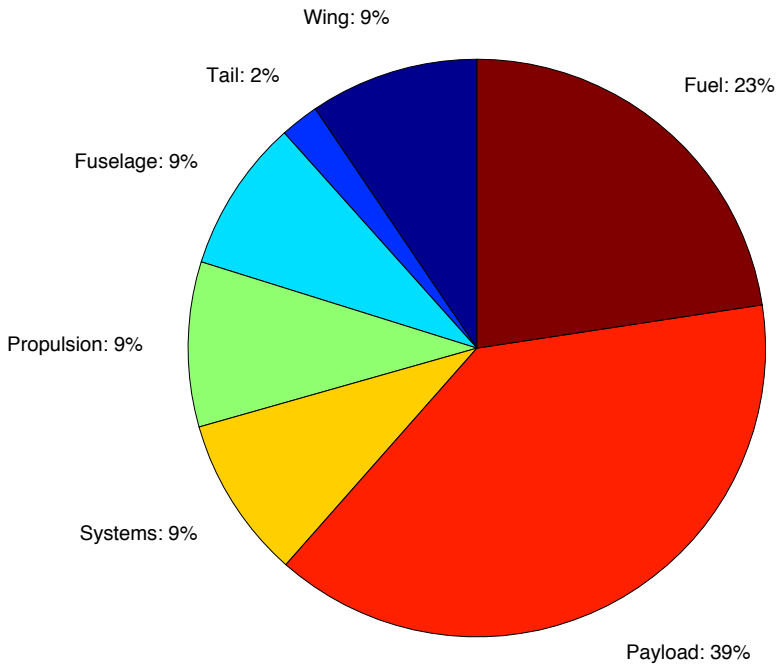

Figure 4.4: Pie chart of the mass distribution of the baseline Propcraft P-420/A concept as predicted with the method after Raymer, fudge factors for advanced composites applied, result iterated

In summary, the mass prediction method after Raymer does not satisfactorily represent the characteristics of the investigated aircraft concept and is expected to significantly underestimate its operating mass empty. This appraisal is supported by the visualization of the mass distribution depicted in Figure 4.4. It shows an empty mass fraction of the aircraft of just 38%, which is much too low, as for transport aircraft, a value of around 50% is reasonable. (Raymer 2012, p.30)

4.2.2 Mass Prediction after Torenbeek (1982) and Comparison to his new Method (2013)

In this section, only the 'detailed' method after Torenbeek (1982) is treated, as the corresponding 'simple' method is mainly intended for initial estimates and listed in Table 4.8 for reference purposes.

Torenbeek's 'detailed' method is the most refined one employed in the IDT. In addition to basic geometrical parameters of the main aircraft components, special items and features are considered in detail to estimate the mass increments they cause. That is, the wing structure mass is evaluated not only on the basis of the general wing geometry, but also considering the contributions of high-lift devices and speed brakes, calculated from the corresponding geometries.

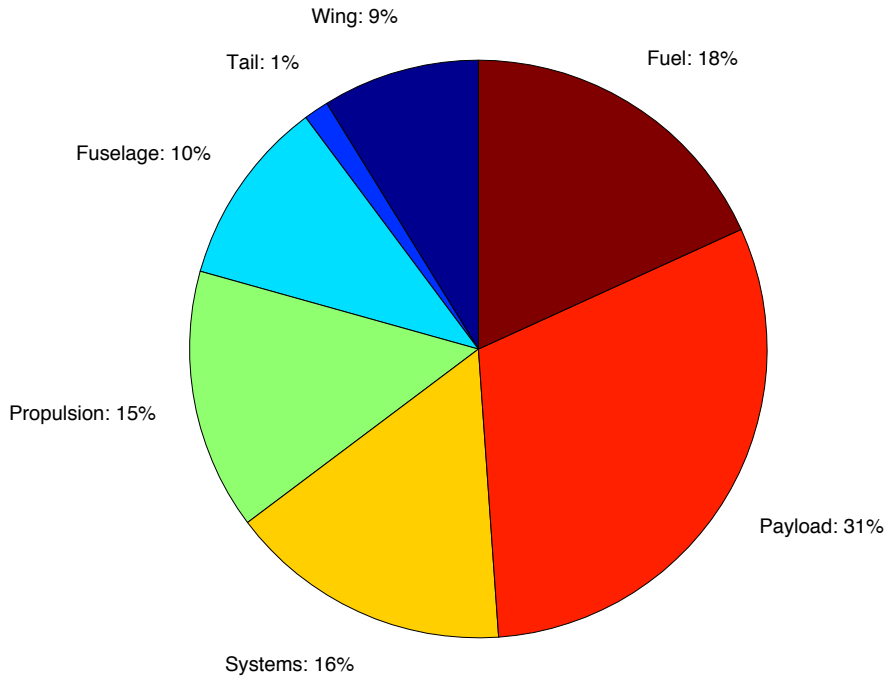

Figure 4.5: Pie chart of the mass distribution of the baseline Propcraft P-420/A concept as predicted with the method after Torenbeek (1982), fudge factors for advanced composites applied, result iterated

The fuselage mass is predicted taking shell area and structure into account while considering doors, windows, and escape hatches. The double-deck layout of the configuration is also incorporated, as the actual flooring areas of the passenger decks and cargo deck are evaluated. The Propulsion group mass is estimated with equations specific for turboprop engines, allowing for propeller, gearboxes, fuel and oil system, and more. Systems, furnishings, and operational items are considered at a similar level of detail.

Compared to the other methods, the mass prediction after Torenbeek (1982) predicts the highest value. However, this seems reasonable against the background of the above explanations. The predicted mass distribution as shown in Figure 4.5 reveals an empty mass fraction of 51%, which is realistic for transport aircraft, cf. Raymer (2012, p.30).

As described in Section 3.4.3, most of the detail of Torenbeek's mass prediction from 1982 has vanished in his newly published method from 2013. Nonetheless, the result for the operating mass empty is very similar. On the basis of the one investigated aircraft concept, it remains unclear, though, if this is more or less a coincidence or, if Torenbeek has managed to significantly simplify his mass estimation methodology while retaining its accuracy. In any case, the applied equations do not specifically take into account that the aircraft is turboprop-driven, whereas the double-deck cabin layout is reflected.

4.2.3 Howe's Mass Prediction

Even though the 'simple' method after Howe only relies on basic geometry and configuration parameters as well as statistical mass fractions, its predicted operating mass empty is close to the one predicted by Torenbeek's 1982 'detailed' method. Howe's comprehensive 'detailed' method features a relatively elaborate calculation of the structural masses of fuselage and wing. However, the mass estimation of other items such as landing gear or systems and equipment is only performed with statistical weight fractions. The distribution of the predicted masses is depicted in Figure 4.6. A realistic empty mass fraction of 49% is reached (cf. Raymer 2012, p.30).

4.2.4 Selection of a Mass Prediction Method for the Concept

On the basis of the above-presented analysis of the different mass estimation methods, Torenbeek's variant from 1982 is considered most realistic here. Due to its level of detail both in the component breakdown and in the extent of considered parameters, it is the method that best respects the special characteristics of the baseline Propcraft P-420/A concept. Therefore, its prediction of an operating mass empty of 97.3 tons and a

corresponding maximum take-off mass of 172.2 tons is employed for the further calculations within the IDT. For completeness, the entire mass breakdown with the single masses of all components is provided in Appendix A for this selected mass prediction method after Torenbeek and as well for the other methods.

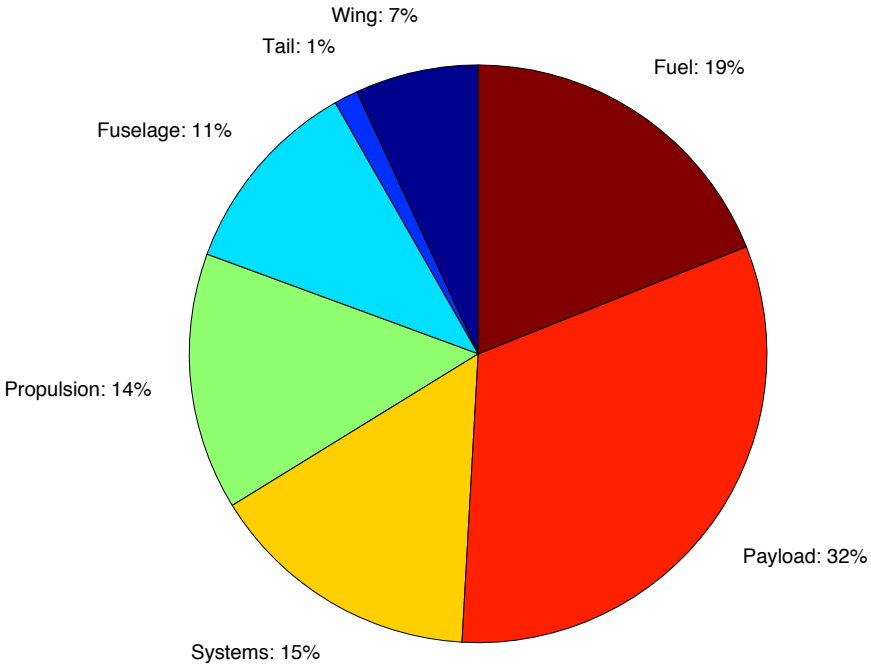

Figure 4.6: Pie chart of the mass distribution of the baseline Propcraft P-420/A concept as predicted with the method after Howe, fudge factors for advanced composites applied, result iterated

4.3 Modeled Propulsion Characteristics

In the context of the analysis of the baseline Propcraft P-420/A concept, the predicted propulsion characteristics cover engine power, fuel consumption, propeller efficiency, and thrust.

4.3.1 Engine Power

A static sea level equivalent power rating of 9,700 kW is adopted. With an assumed difference of 5% this leaves a shaft power of 9,238 kW. The flight Mach number and altitude dependency of the available equivalent engine power is predicted with Equations (3.44) to (3.46). The maximum engine power is limited to static sea level rating as suggested by Iwanizki (2013, p.55). In cruise flight an equivalent power of 5,667 kW remains with a corresponding shaft power of 5,398 kW. Figure 4.7 shows the predicted equivalent engine power over the range of flight Mach number and altitude.

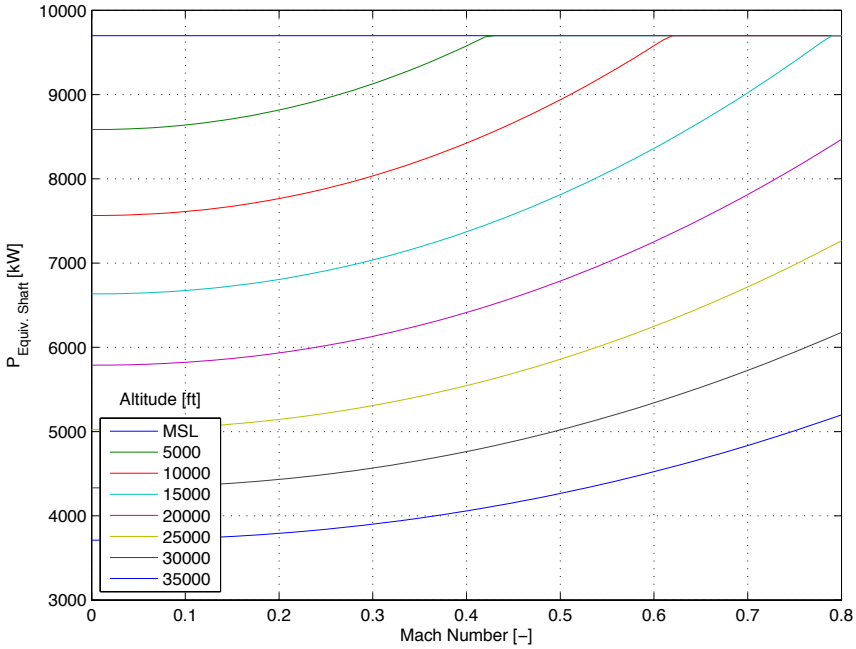

Figure 4.7: Predicted equivalent power of a single engine of the baseline Propcraft P-420/A concept as a function of flight Mach number and altitude

4.3.2 Engine Fuel Consumption

The predicted engine fuel consumption characteristic shown in Figure 4.8 is derived with the developed model as described in Section 3.5.2. The level of the absolute values is adjusted with an offset to match Iwanizki's design value of 1.7956 N/kW/h for cruise flight conditions. (Iwanizki 2013, p.112)

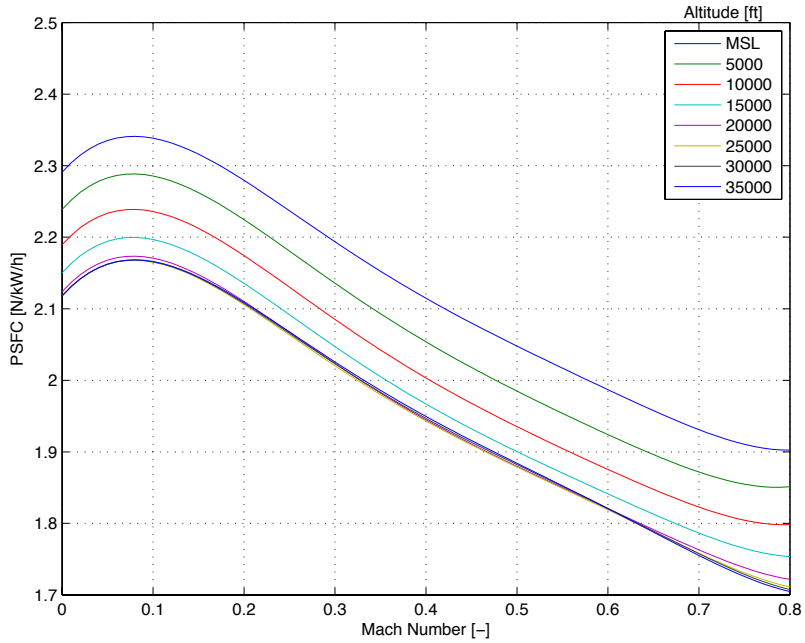

Figure 4.8: Predicted equivalent power-specific fuel consumption of a single engine of the baseline Propcraft P-420/A concept as a function of flight Mach number and altitude

The fuel consumption characteristic is used to predict the fuel consumption of the baseline Propcraft P-420/A concept during different flight phases and eventually over the entire design mission. Section 4.4 covers the aircraft performance as well as the design mission performance calculation in detail.

4.3.3 Propeller Efficiency

As described in Section 3.5.3, the propeller efficiency is estimated in a multistage process after Howe with corrections after Raymer. The rotational speed of the propeller is set to a value of 12 revolutions per second, which corresponds to the propeller diameter of 5 m of the baseline Propcraft P-420/A concept and the predefined 60 m/s for (nD_P).

With (nD_P) the advance ratio is calculated and then corrected for nacelle blockage. This corrected advance ratio is used for the initial propeller efficiency estimation after Howe. Its sectional definition depending on the advance ratio is the reason for the first bend in the efficiency characteristic of Figure 4.9 at Mach numbers slightly greater than 0.2. At Mach numbers lower than this, the characteristic for advance ratios less than one applies. At greater Mach numbers, the equation for advance ratios equal to or greater than one is used. The calculated efficiency is subsequently corrected for tip Mach effects and for increased propeller slipstream drag. The tip Mach correction causes the second bend starting at Mach numbers around 0.6, because it only applies to tip Mach numbers greater than 0.89 and deteriorates efficiency rapidly with increasing Mach numbers.

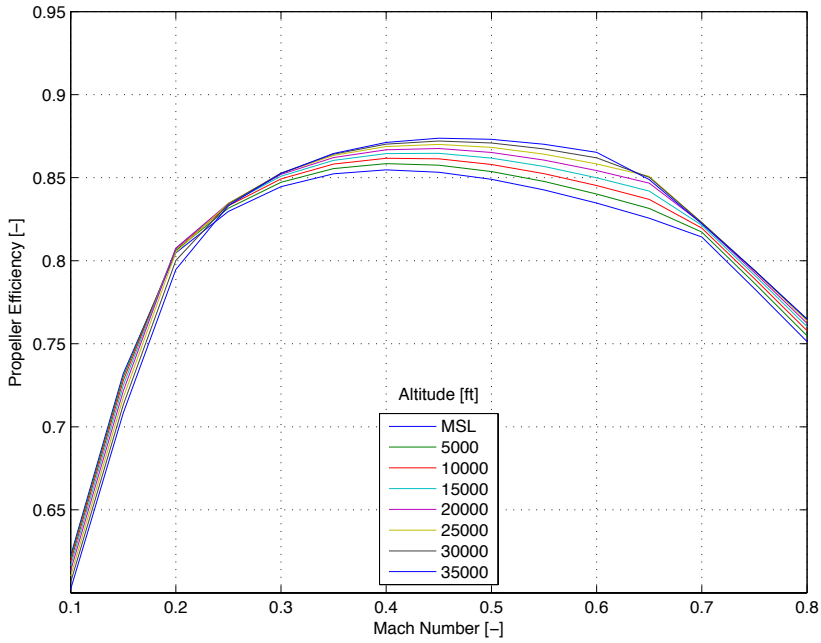

Figure 4.9: Predicted propulsive efficiency of the propeller of the baseline Propcraft P-420/A concept as a function of flight Mach number and altitude

In the design cruise condition, the method delivers a propeller efficiency of 0.856, which is a reasonable yet not very ambitious value. Typical efficiencies of modern propellers range from 0.85 to 0.92. (Torenbeek 1982, p.191; Bräunling 2009, p.502)

Unfortunately, the employed efficiency estimation methodology does not take into account that the propeller of the baseline Propcraft P-420/A concept is intended as a dual-stage counter-rotating configuration, which increases the efficiency compared to single-stage propellers. (Nicolai and Carichner 2010, p.456) To try and estimate the influence of counter-rotation on propeller efficiency, a graphical method is applied that was developed by Gilman Jr. (1953) for the NACA. However, this method is only calibrated for engine shaft power ratings up to about 7,500 kW and hence has to be extrapolated for an application to the engine of the baseline Propcraft P-420/A concept with an estimated shaft power of 9,238 kW. The result is an efficiency of 0.842 in cruise flight, which is even less than the previously predicted value. Thus, the result of this method is considered too low and not realistic, possibly due to the necessary extrapolation, or also because of technological advancement in propeller design since the 1950s.

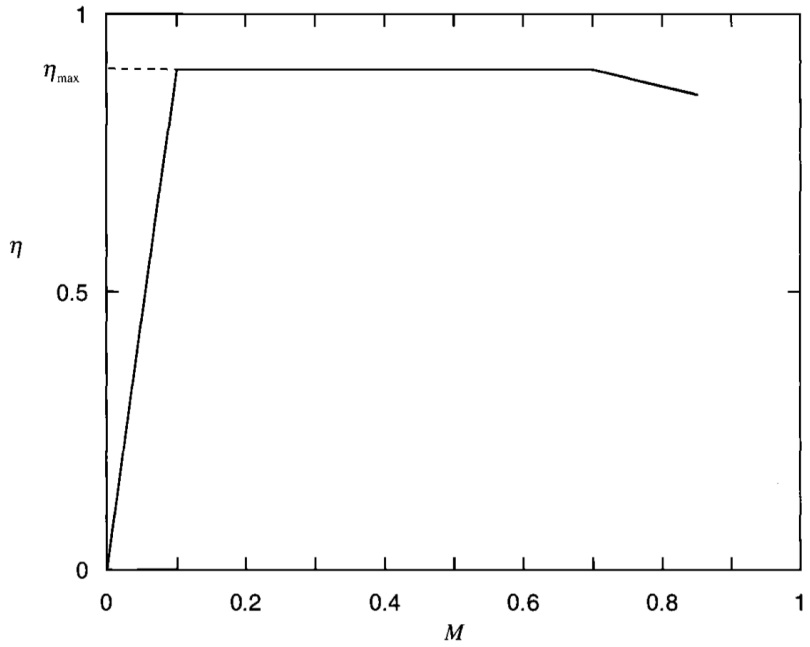

Figure 4.10: Simple model of the propulsive efficiency of the propeller of a turboprop engine as a function of flight Mach number after Mattingly et al. (2002, p.602)

In order to assess the accuracy of the predicted characteristic as shown in Figure 4.9, it is compared to a simpler propeller efficiency model proposed by Mattingly et al. (2002, p.602) and depicted in Figure 4.10. This model neglects the altitude-dependency of the propeller efficiency. However, it features three similar areas as the prediction employed

in this work: A continuous increase of the efficiency in the first section up to a constant value in the second section and then a continuous decrease at high Mach numbers. Thus, the predicted characteristic in Figure 4.9 can be considered reasonable, while the differences between the two models result from the varying degree of detail.

4.3.4 Thrust

The thrust of a turboprop engine is calculated with the previous results as the product of engine power and propeller efficiency divided by the flight velocity, cf. Equation (3.64). The resulting thrust characteristic is shown in Figure 4.11. From a maximum value of 177.4 kN at MSL and a Mach number of 0.1, thrust decreases rapidly with higher flight speeds and altitudes. As mentioned in Section 3.5.4, for Mach numbers below 0.1, the thrust value at Mach 0.1 is employed, i.e., 177.4 kN is also the static thrust. Comparison to Figure 3.5 after Mattingly et al. verifies that the predicted characteristic is realistic.

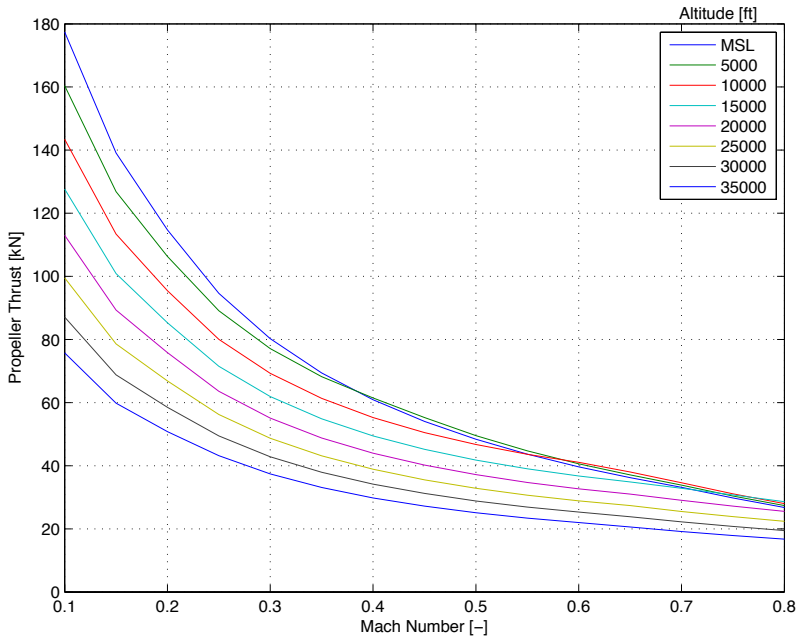

Figure 4.11: Predicted thrust of a single engine of the baseline Propcraft P-420/A concept as a function of flight Mach number and altitude

4.4 Aircraft Concept Performance Calculation

Combining the results of the three described modules, i.e., aerodynamics, masses, and propulsion, performance aspects of the investigated aircraft concept are evaluated in a final step of the IDT. In the following subsections, both the applied calculation methods and the results for the baseline Propcraft P-420/A concept are presented. A crosscheck with corresponding design requirements and constraints reveals critical aspects of the configuration and enables the identification of design drivers for performance.

4.4.1 Initial Estimation of Mission Segment Weight Fractions

It is a requirement of most of the performance calculations to provide an estimate of the mass of the aircraft in the considered flight condition. Specific knowledge of the fuel burn in different flight segments, however, is only available after a detailed mission calculation has been carried out. Initially, statistically derived mission-segment weight fractions W_i/W_{i-1} are employed instead that resemble the aircraft mass after a segment divided by the mass before it. Table 4.9 lists the values of these weight fractions as they are implemented in the IDT. (Raymer 2012, p.151)

Table 4.9: Statistical mission-segment weight fractions for initial estimates of the aircraft mass in different flight stages (Raymer 2012, p.151)

Statistical mission-segment weight fractions W_i/W_{i-1}	
Engine start, taxi and take-off	0.98
Climb and acceleration	$1.0065 - 0.0325M_{final}$
Descent for landing	0.99
Landing and taxi	0.995

4.4.2 Steady Level Flight Considerations

Steady level flight refers to the unaccelerated flight conditions, in which lift balances weight and thrust equals drag. Under this constraint and assuming flight at the design cruise altitude of 29,000 ft, several conclusions regarding the aircraft performance can be drawn.

4.4.2.1 Minimum Required Thrust in Design Cruise Altitude

The flight with minimum required thrust at a given altitude is reached at a combination of velocity and lift coefficient that yields minimal total drag. This occurs at maximum L/D, which is also the condition for maximum range of a propeller-driven aircraft. (Raymer 2012, p.656).

The thrust characteristics of the baseline Propcraft P-420/A concept are visualized in Figure 4.12 for the flight condition at the top of climb (TOC), i.e., the initial design cruise. The calculation is thus based on an aircraft mass estimated as the maximum take-off mass multiplied with the statistical mission-segment weight fractions for taxi / take-off and climb / acceleration. Available thrust and produced drag force are shown for steady level flight with varying Mach number at the design cruise altitude.

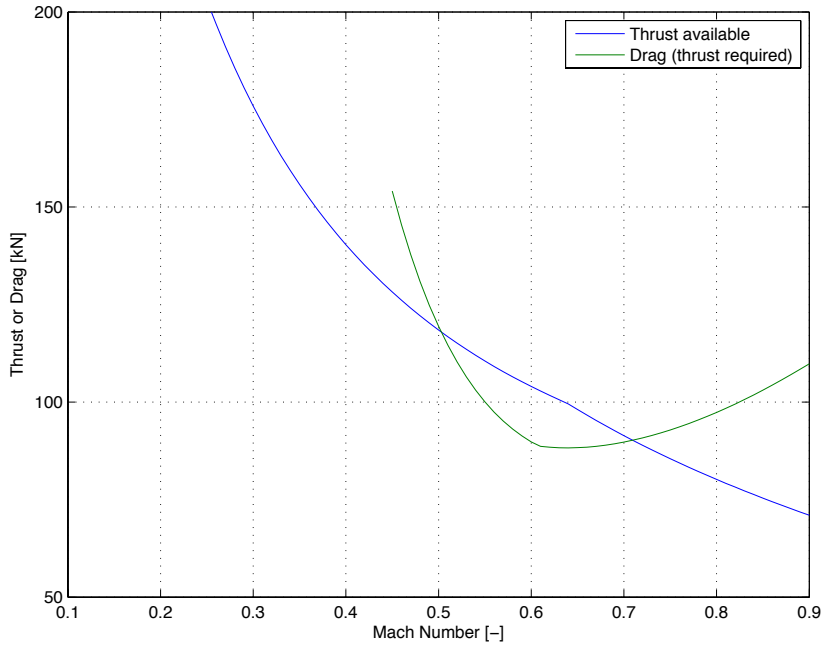

Figure 4.12: Available thrust and drag characteristics of the baseline Propcraft P-420/A concept with estimated initial cruise weight at the TOC

The range of steady aircraft operation, in which thrust is greater than drag, can be identified as well as the flight condition with minimum drag, i.e., with minimum required thrust. Table 4.10 lists the characteristic numbers of the minimum-thrust flight condition. Obviously, the previously specified combination of design cruise altitude and design cruise Mach number 0.64 (cf. Section 2.2.3) is appropriately chosen as the flight condition with minimum thrust so as to enable maximum range operation.

Table 4.10: Characteristics of level flight with minimum required thrust at the TOC of the baseline Propcraft P-420/A concept with estimated initial cruise weight

Flight with minimum thrust at the TOC	
Airspeed	195 m/s
Mach number	0.64
Lift coefficient	0.723
Drag coefficient	0.039
Lift to drag ratio	18.483
Total required thrust	88.3 kN
Theoretically attainable cruise range	3,664 km

Based on the statistical weight fractions and the design mission fuel specification, a maximum cruise range can be calculated with the Breguet range equation (Equation (4.1), cited after Raymer (2012, p.659)) for a flight with minimum required thrust.

$$R = \frac{\eta}{ESFC}\frac{L}{D}\ln\left(\frac{W_{start\,cruise}}{W_{end\,cruise}}\right) \tag{4.1}$$

This range is theoretical, however, as it does not account for reserves or a diversion flight, which is generally required. The evaluation of Equation (4.1) for the baseline Propcraft P-420/A concept yields a theoretical range of 3,664 km, cf. Table 4.10.

4.4.2.2 Minimum Required Power in Design Cruise Altitude

Similar to the flight condition with minimum thrust, a different condition can be identified that is the one with minimum power. The required power is defined as thrust force multiplied with the flight velocity. (Raymer 2012, p.657) The corresponding characteristic is depicted in Figure 4.13 for the baseline Propcraft P-420A concept with the estimated initial cruise weight at the design cruise altitude. Additionally, the total available engine power at this altitude is shown.

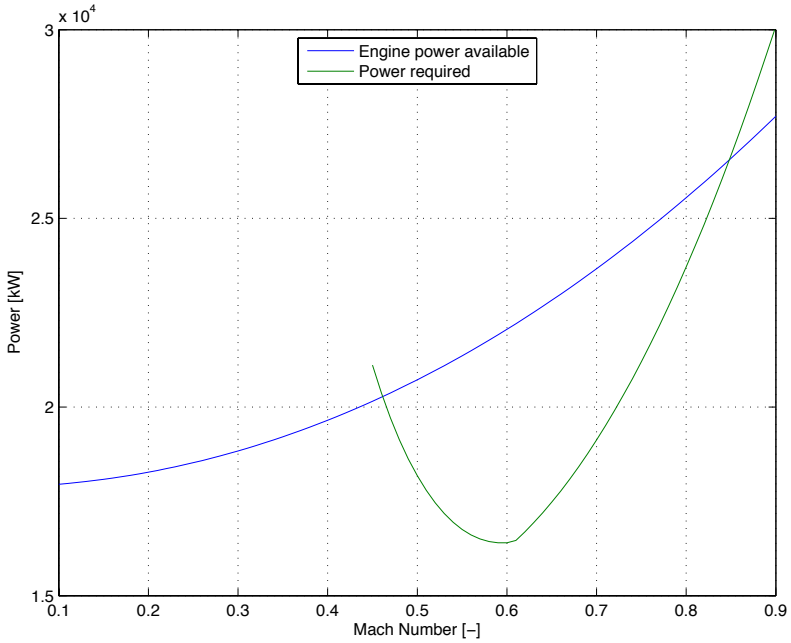

Figure 4.13: Engine and drag power characteristics of the baseline Propcraft P-420/A concept with estimated initial cruise weight at the TOC

The flight condition with minimum required power, i.e., with minimum drag power, can be evaluated, which is the flight condition that yields the maximum loiter endurance of a propeller-powered aircraft. In Table 4.11, the corresponding parameters for a minimum-power flight at design cruise altitude are listed.

$$E = \frac{\eta}{ESFC}\frac{1}{V}\frac{L}{D}\ln\left(\frac{W_{start\,loiter}}{W_{end\,loiter}}\right) \tag{4.2}$$

Like the theoretical range in the previous section, a theoretical endurance can be calculated with these parameters according to Equation (4.2). For the baseline Propcraft P-420/A concept, it results in a theoretical loiter endurance of 5.48 h, cf. Table 4.11.

Table 4.11: Characteristics of steady level flight with minimum required power at the TOC of the baseline Propcraft P-420/A concept with estimated initial cruise weight

Flight with minimum power at the TOC	
Airspeed	180 m/s
Mach number	0.59
Lift coefficient	0.851
Drag coefficient	0.048
Lift to drag ratio	17.868
Total required thrust	91.3 kN
Theoretical maximum endurance	5.48 h

4.4.2.3 Specific Excess Power Aspects

Besides the flight mechanic considerations presented in the previous sections, specific excess power (SEP) calculations are commonly used in aircraft performance prediction. At a given flight condition, the total energy of an aircraft consists of potential and kinetic energy, which are principally interchangeable. Dividing the total energy by the aircraft weight yields the specific energy or energy height. The change of specific energy over time is given by the specific power. An increase in specific power can only be driven by the propulsion system of the aircraft, which leads to the concept of excess power. This is the difference of thrust and drag multiplied with the flight velocity. The specific excess power is thus defined according to Equation (4.3), the derivation of which can be found in Raymer (2012, p.678). It is a measure for the momentary capability of the aircraft to climb or accelerate.

$$SEP = \frac{V\left(T - D\right)}{W} = \frac{dh}{dt} + \frac{V}{g}\frac{dV}{dt} \tag{4.3}$$

SEP calculation can be used to evaluate the operating limitations of an aircraft, i.e., the flight conditions, in which the SEP approaches zero or a predefined threshold value. In Figure 4.14, the SEP of the baseline Propcraft P-420/A concept with estimated initial cruise weight is plotted over the flight Mach number for different altitudes. All of the curves begin in the stall condition with the lowest possible Mach number for the respective altitude. From there, the SEP values increase with rising Mach numbers to distinctive maximums. The Mach numbers, at which these maximums are reached, rise with the flight altitude. Further increases in the Mach number lead to rapid decreases of the

SEP values, as thrust diminishes and drag rises. Note that the SEP curve for an altitude of 35,000 ft features only negative values, i.e., the aircraft cannot steadily operate at this altitude.

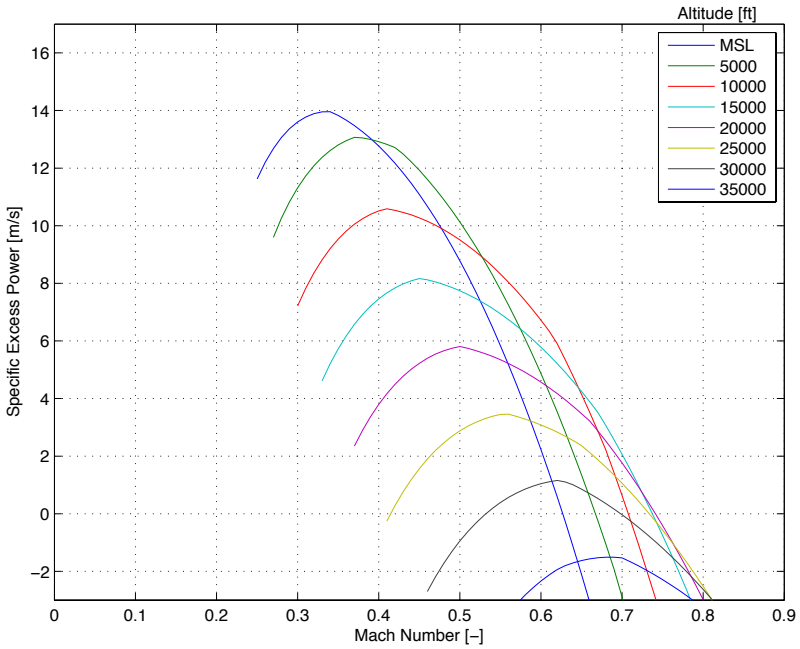

Figure 4.14: Specific excess power of the baseline Propcraft P-420/A concept with estimated initial cruise weight plotted over the flight Mach number for several altitudes

Another visualization of the SEP data of the baseline Propcraft P-420/A concept with estimated initial cruise weight is shown in Figure 4.15. Here, the range of occurring SEP values is categorized in domains of 1 m/s and the contours of the flight Mach numbers and altitudes are plotted that yield SEP values in the respective domain. This plot reveals the aircraft's ceiling and the maximum Mach number. Table 4.12 tabulates these values, of which the service ceiling is defined according to FAR requirements as the altitude in which a rate-of-climb capability of 100 fpm (equal to a 0.5 m/s SEP) remains. (Raymer 2012, p.687) Maximum operating altitude and Mach number, however, imply zero SEP.

Table 4.12: Operating limitations for steady level flight of the baseline Propcraft P-420/A concept with estimated initial cruise weight

Operating limitations	
Service ceiling (100 ft/min climb rate remaining)	31,300 ft
Maximum operating altitude	32,200 ft
Maximum operating Mach number	0.74

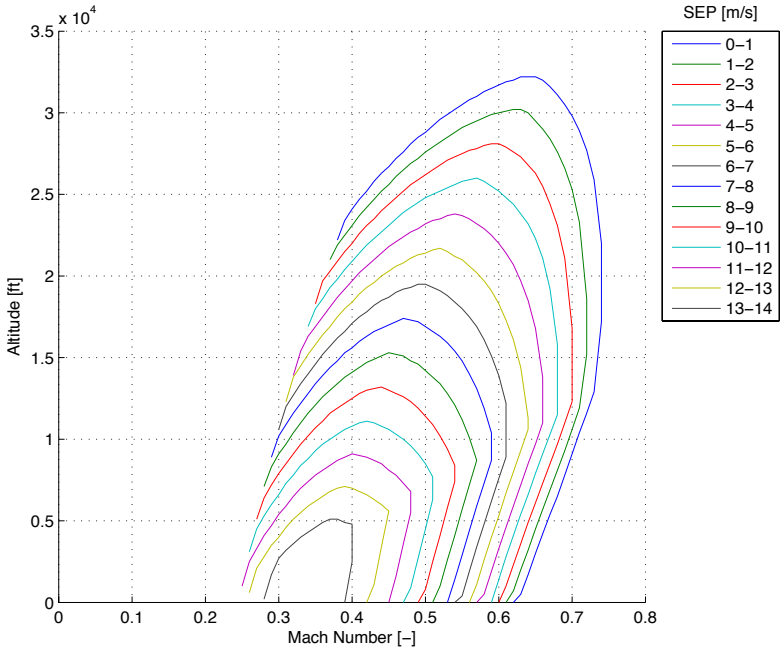

Figure 4.15: Specific excess power contours over the operating ranges of flight Mach number and altitude of the baseline Propcraft P-420/A concept with estimated initial cruise weight

4.4.3 Take-off

For the evaluation of the take-off performance, a distinction is made between the normal case with all engines operating and the one-engine-inoperative (OEI) case, which is especially relevant for certification regulations. As pictured in Figure 4.16, the take-off analysis is broken down into different segments.

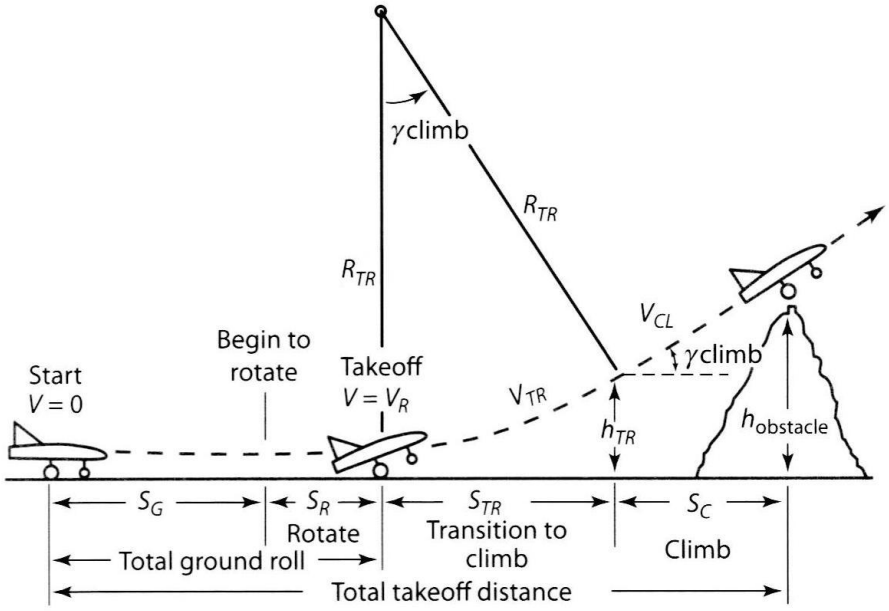

Figure 4.16: Schematic diagram of the different segments considered in take-off analysis after Raymer (2012, p.688)

Ground roll covers the level roll on the ground, during which the aircraft accelerates, as well as the ground roll while rotating the aircraft up to the liftoff angle of attack. After liftoff, the aircraft follows an approximately circular transition arc until the desired climb angle is reached and it commences the so-called second-segment climb. The total take-off distance is defined from the beginning of ground roll until an obstacle clearance height is reached, which is specified with 35 ft in the FAR Part 25 certification specifications for commercial aircraft. (cited after Raymer 2012, p.988)

To enable comparisons, take-off calculations after different authors are implemented in the IDT and presented in the following. As mentioned in Section 4.1.2.3, for the baseline Propcraft P-420/A concept, a high-lift device configuration with leading-edge slats and single-slotted Fowler flaps in take-off setting is considered.

4.4.3.1 All engines operating – Take-off Distance

Raymer (2012, p.688) presents a comprehensive set of equations for calculating the different segments of take-off. The acceleration phase of ground roll is calculated with Equation (4.4).

$$S_G = \frac{1}{2gK_A} \ln\left(\frac{K_T + K_A V_R^{\,2}}{K_T + K_A V_i^{\,2}} \right) \tag{4.4}$$

with

$$K_T = \frac{T}{W} - \mu \tag{4.5}$$

$$K_A = \frac{2}{\rho\left(W/S_{ref}\right)} \left(\mu C_L - C_{D0} - K_{in\,ground\,effect} C_L^{\,2} \right) \tag{4.6}$$

where V_R is the velocity of rotation, taken as 1.1 times the stall speed in take-off configuration (FAR Part 25), V_i is any initial velocity at the beginning of acceleration, here zero. Because the thrust T varies during acceleration, it is evaluated at about 70% of V_R. The aircraft weight is the maximum take-off weight. μ is the ground rolling resistance coefficient, which is 0.03 on a dry concrete or asphalt runway. The lift coefficient is evaluated during level ground roll. As described in Section 3.3.2.2, the drag-due-to-lift factor K is reduced by the ground effect. In the drag parameters of Equation (4.6), the additional contributions of deployed high-lift devices and landing gear are considered.

The time for rotating the aircraft is assumed with three seconds at constant speed V_R. The distance travelled is hence given by Equation (4.7).

$$S_R = 3s \times V_R \tag{4.7}$$

During the transition arc, the aircraft accelerates from the take-off velocity V_R (1.1 times stall speed) to the nominative climb speed V_2, which is 1.2 times the velocity of stall (FAR Part 25). For passenger comfort, the average vertical acceleration in this maneuver is set to 1.2*g*. With this, the radius of the transition arc R_{TR} can be determined according to Equation (4.8):

$$R_{TR} = \frac{V_2^{\,2}}{0.2g} \tag{4.8}$$

The climb angle γ_2 at the end of the transition arc and in the second segment is then found with Equation (4.9), which yields the distance traveled during transition S_{TR} and the height h_{TR} at the end of the transition arc (Equation (4.10) and (4.11), respectively).

$$\sin\gamma_2 = \frac{T - D}{W} \tag{4.9}$$

$$S_{TR} = R_{TR} = \sin\gamma_2 = R_{TR}\left(\frac{T - D}{W}\right) \tag{4.10}$$

$$h_{TR} = R_{TR}\left(1 - \cos\gamma_2\right) \tag{4.11}$$

If the obstacle height is cleared before the end of the transition arc, S_{TR} is given by Equation (4.12). Otherwise, an additional climb segment is included (Equation (4.13)).

$$S_{TR} = \sqrt{R_{TR} - \left(R_{TR} - 35ft\right)^2} \tag{4.12}$$

$$S_C = \frac{35\,\mathrm{ft} - h_{TR}}{\tan\gamma_2} \tag{4.13}$$

The results of these calculations for the baseline Propcraft P-420/A concept are grouped in Table 4.13.

Table 4.13: Take-off performance of the baseline Propcraft P-420/A concept at MTOM with all engines operating, estimated after Raymer (2012, p.688)

Take-off performance with all engines operating	
Rotation and take-off velocity	85 m/s
Total ground roll distance	1,864 m
Total take-off distance over 35 ft obstacle	2,157 m
Climb angle in second segment	4.3°

A simplified approach for evaluating take-off performance is proposed by Howe (2000, p.174). It is partly statistics-based and therefore features coefficients specific to turbo-

prop aircraft. The distances of ground roll, rotation and climb to obstacle clearance are calculated with Equations (4.14) to (4.16) and added up to the total take-off length. The result for the baseline Propcraft P-420/A concept is a total ground roll distance of 1,780 m and a total take-off distance over a 35 ft obstacle of 1,850 m.

$$S_G = \frac{0.12}{C_{L,liftoff}} \left(\frac{T_S}{W} \right)^{-1.35} \frac{W}{S_{ref}} \tag{4.14}$$

$$S_R = 6 \left(\frac{W}{S_{ref} C_{L,liftoff}} \right)^{1/2} \tag{4.15}$$

$$S_C = 120 \left(1 - \frac{T_S}{W} \right) \tag{4.16}$$

where T_S is the static thrust.

A third calculation method for take-off analysis is applied after Torenbeek (1982, p.167). Equation (4.17) is also semi-empirical and gives the total take-off distance.

$$S_{TO} = 35\,\text{ft} \times \left[\left(\frac{V_2}{V_S} \right)^2 \frac{W / S_{ref} \left\{ \left(T/W - \mu' \right)^{-1} + \sqrt{2} \right\}}{35\,\text{ft} \times \rho g C_{L\max} \left(1 + \gamma_{TO} \sqrt{2} \right)} + \frac{1}{\gamma_{TO}} \right] \tag{4.17}$$

where V_2 is the velocity during climb and V_S the stall speed. The thrust T is evaluated at about 70% of the liftoff speed, as in Raymer's approach. μ' is a corrected ground rolling resistance coefficient, calculated with Equation (4.18). $C_{L\,max}$ is the maximum lift coefficient in take-off configuration and γ_{TO} the climb angle after liftoff, which is calculated with Equation (4.9).

$$\mu' = \mu + 0.72 C_{D0} / C_{L\max} \tag{4.18}$$

Torenbeek's method results in a take-off distance of 2,329 m for the baseline Propcraft P-420/A concept.

Comparison of the results of the three methods shows considerable differences between the estimated total take-off distances. However, the level of detail varies greatly among the approaches. Raymer's method is the most detailed and the least empirical and thus considered the most accurate.

4.4.3.2 One Engine Inoperative – Balanced Field Length

For aircraft certification, the take-off performance with one engine inoperative has to be evaluated in terms of the balanced field length (BFL). This is the total take-off distance

to the obstacle clearance height when an engine fails at the decision speed V_1, the speed, at which the aircraft can either brake to a halt or continue take-off with one engine failed in the same total distance.

An empirical method for the calculation of the BFL was developed by Torenbeek (1982, p.168) with Equation (4.19), and is adopted by Raymer (2012, p.692).

$$BFL = \frac{0.863}{1+2.3\Delta\gamma_2}\left(\frac{W/S_{ref}}{\rho g C_{L,2}} + 35\,\text{ft}\right)\left(\frac{1}{T/W-\mu'} + 2.7\right) + \frac{\Delta S_{TO}}{\sqrt{\sigma}} \tag{4.19}$$

with

$$\Delta\gamma_2 = \gamma_2 - \gamma_{min} \tag{4.20}$$

where γ_{min} is 0.03 rad for four-engined aircraft, 0.027 rad for three- or 0.024 rad for two-engined configurations. These values are minimum climb rates required by the FAR Part 25 certification specifications. Thrust is again evaluated at about 70% of the liftoff speed, which is assumed here as 1.2 times the stall speed. (Raymer 2012, p.693) The corrected ground rolling resistance coefficient is calculated with Equation (4.21).

$$\mu' = 0.01 C_{L\,max} + 0.02 \tag{4.21}$$

The evaluation of this method for the baseline Propcraft P-420/A concept at MTOM yields no result. With one engine inoperative in the second segment only a climb angle of 0.021 rad is reached, i.e., the certification requirement of 0.03 rad is not met and, hence, a BFL cannot be calculated.

Instead of evaluating take-off performance with one engine inoperative, Howe (2000, p.175) suggests calculating the accelerate-stop distance (Equation (4.22)) on the ground for a rejected take-off with an engine failure at the decision speed V_1, which is assumed as 0.94 times the liftoff speed. Furthermore, the equation implies a braking coefficient on the runway of 0.4. The result of this equation is 1,955 m for the baseline Propcraft P-420/A concept.

$$S_{AS} = \frac{0.0984}{C_{L,liftoff}}\frac{W}{S}\left[\left(\frac{T_S}{W}\right)^{-1.35} + 2.2\right] \tag{4.22}$$

4.4.4 Landing

Similar to the take-off analysis, landing performance is evaluated. Here, the ‘worst case’ scenario of a landing at maximum take-off mass is analyzed with the IDT, which cannot occur in reality, however, as fuel is consumed during take-off. Still, this analysis can be used to appraise the landing performance of the investigated concept and to

assess, whether a restriction has to be imposed on the maximum permissible landing mass.

For the calculation of the total landing distance as suggested by Raymer (2012, p.693), approach begins when the aircraft descends below an obstacle clearance height of 50 ft, see Figure 4.17. (Raymer 2012, p.988) This approach is flown with a descent angle γ_a of three degrees and an approach speed V_a of 1.3 times the stall speed in landing configuration (FAR Part 25). When the flare height h_f is reached, the aircraft starts to increase its incidence and to reduce speed on an approximately circular path until it touches down with a touchdown speed V_{TD} of 1.15 times the stall speed (FAR Part 25). Similar to the take-off transition arc, an average vertical acceleration of 1.2g is assumed. Hence, the flare height can be calculated with Equation (4.11). Approach and flare distance are then evaluated with Equations (4.13) and (4.10), respectively.

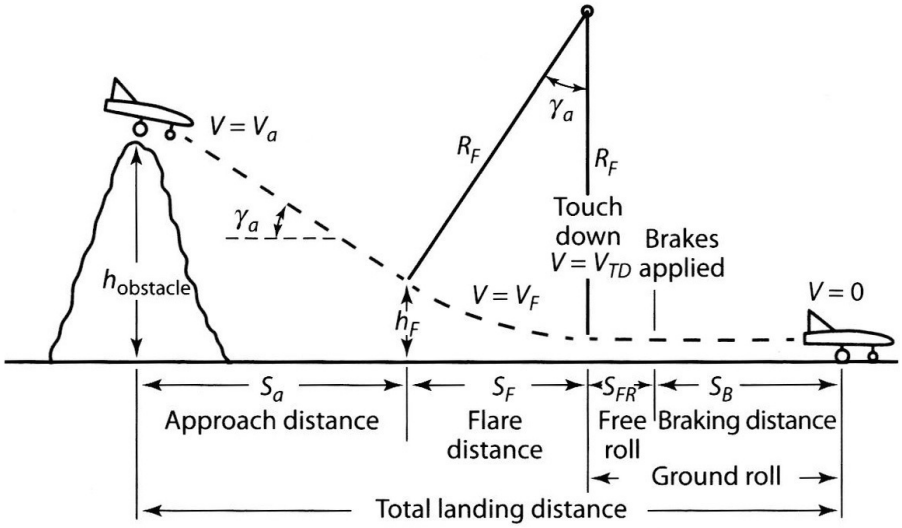

Figure 4.17: Schematic diagram of the different segments considered in landing analysis after Raymer (2012, p.694)

After touchdown, three seconds of free roll with V_{TD} are assumed before the brakes of the aircraft are applied, cf. Equation (4.7). The following deceleration can be calculated with Equations (4.4) to (4.6), where the initial velocity is V_{TD} and the final velocity is zero. Thrust is idle, reverse thrust is not considered due to specification regulations. Additional drag of deployed speed brakes is taken into account and the braking coefficient μ is taken as 0.4 for a dry concrete or asphalt runway. The sum of these distances yields the total landing distance, however, certification specification requires adding an additional two-thirds of this distance to allow for pilot technique. The resulting FAR landing distance for the baseline Propcraft P-420/A concept is 2,022 m.

Again, Howe (2000, p.179) provides a simplified landing analysis with Equation (4.23) that presumes a 50 ft obstacle clearance, a descent angle of three degrees, and a braking coefficient of 0.38. For the investigated aircraft concept, it yields an FAR landing distance of 1,977 m.

$$S_{LDG,FAR} = 488 + 4.5V_a + 0.0255\left[\frac{1}{\frac{\mu}{0.38}} + \frac{5.59}{\frac{\mu}{0.38} + 1.2\frac{T_S}{W_{TO}}\frac{W_{TO}}{W_{LDG}}} + 1.08\right] \quad (4.23)$$

The landing distance calculation after Torenbeek (1982, p.170) is stated in Equation (4.24), where $\overline{\gamma}$ is the mean descent angle between approach and touchdown. The descent angle at touchdown is approximated by the lift to drag ratio at touchdown. The average deceleration $\overline{a}$ during ground roll is approximately 0.45 for turboprop-powered aircraft. The resulting FAR landing distance of the baseline Propcraft P-420/A concept is 2,328 m.

$$S_{LDG,FAR} = 50\,\text{ft} \times \frac{5}{3}\left[\frac{1}{\overline{\gamma}} + \frac{W_{LDG}/S_{ref}}{50\,\text{ft} \times \rho g C_{L\max}}\left\{\left(\frac{V_{TD}}{V_a}\right)^2\left(\frac{1}{\overline{a}/g} - \frac{1}{\overline{\gamma}}\right) + \frac{1}{\overline{\gamma}}\right\}1.3^2\right] \quad (4.24)$$

As with the take-off distance, also the predicted landing distance differs slightly among the methods. Raymer's calculation is again the most detailed and therefore considered here as the most accurate.

4.4.5 Design Mission and Payload-Range

The IDT performs a comprehensive analysis of the aircraft performance on the design mission as specified in Section 2.2.3. Each mission segment is evaluated separately with regard to speed, duration, distance covered, and fuel burned. The following list provides details on the calculation of each segment, starting with the SPP mission.

- Taxi out: Taxiing is assumed to occur at a power setting of 60%, which resembles a typical "ground idle." (Bräunling 2009, p.300) Fuel burn is directly calculated with the specified taxi time and the power specific fuel consumption.
- Take-off: A common assumption for the take-off calculation of transport aircraft is a time of one minute at maximum power. (Raymer 2012, p.729) However, as the specific fuel consumption varies during the acceleration of take-off (cf. Figure 4.8), a mean value is employed.
- Climb: The climb to cruise altitude is performed first with constant CAS up to a transition altitude and then with constant Mach number, cf. Figure 2.5. (Ittel 2014, p.12) Due to the decreasing ambient air density, a climb with constant

CAS implies an increasing TAS and thus a simultaneous acceleration. The transition altitude is the altitude, in which the predefined CAS and Mach number yield the same TAS value. A climb power setting of 95% is assumed. For the calculation, the IDT subdivides the climb into 100 ft-segments. For each segment, climb performance and fuel consumption are evaluated. Adding up all segments yields the total climb time, distance covered and fuel burned. Through the segment-wise calculation, an accurate estimation is provided, as both the changing airspeed and the decreasing aircraft weight during the climb are considered. For comparison, an optimum climb to cruise altitude is calculated with airspeeds that yield the best climb rate for each segment.

- Cruise: A similar approach is taken for the evaluation of cruise flight. Based on the specified design range, the distance covered during climb and an estimation of the distance flown during descent, the required distance for the steady level cruise flight is calculated. It is then subdivided into 1 km-segments that are individually evaluated. Again, adding up these segments yields the total cruise time and fuel burn.
- Descent: Similar to the climb evaluation, descent is subdivided into 100 ft-segments. A constant descent angle is assumed, which has to be preset. Above a transition altitude, descent is flown with a constant Mach number, then with a constant CAS. Again, the segments are added up for the total descent figures.
- Approach and landing: Due to its low contribution to fuel burn, approach and landing are not calculated in detail. The corresponding fuel consumption is statistically estimated with the statistical weight fraction as in Table 4.9.
- Taxi in: As taxi out.

In addition to the described SPP mission segments, diversion flight and reserves are evaluated as required by certification regulations and depicted in Figure 2.5.

- Diversion climb: The climb to the diversion cruise altitude is treated identical to the SPP-mission climb, however, it is assumed that this climb is flown with the airspeed for a best rate of climb.
- Diversion cruise: Similar to the calculation procedure of the design mission cruise, the distance to cover in the diversion cruise is estimated from the specified diversion range requirement.
- Diversion descent: It is assumed that the diversion descent is flown with the diversion cruise Mach number to the transition altitude and then with constant CAS.

- Loiter: For the analysis, loiter time is subdivided into 1 min-segments, which are calculated separately. Loitering is evaluated for flight with constant CAS as specified and additionally for flight with the optimum loiter speed, i.e., the one with minimum required power, for comparison purposes.
- Reserve: In addition to the diversion and loiter profile, certification regulations require a reserve fuel allowance of 10% of the enroute flight time of the SPP mission design cruise. (Torenbeek 2013, p.387)

In conclusion, the durations, distances, and masses of burned fuel of the different mission segments are added up to total values. With these, the total required fuel for the design mission and the efficiency of the aircraft concept are evaluated. For the baseline Propcraft P-420/A concept, the results of the analysis are tabulated in Table 4.14. It can be seen that a considerable amount of fuel is consumed during taxiing, which is mainly due to the specification of extensive taxi times. Furthermore, climb performance is not satisfactory with a time to cruise altitude of 52 min. The result for an optimized climb, however, proves that the climb capability of the aircraft is sufficient in principle.

Table 4.14: Analysis of the performance of the baseline Propcraft P-420/A concept on its design mission including diversion and loiter

Mission segment	Duration h:min	Distance NM (km)	Fuel burn kg	Remark
Taxi out	0:40	–	3,626	
Take-off	0:01	–	149	
Climb	0:52	251 (465)	3,896	Trans. alt.: 26,400 ft
Optimized climb	0:30	154 (286)	2,479	
Cruise	4:02	1,526 (2,826)	14,059	
Descent	0:16	89 (164)	775	Trans. alt.: 24,500 ft
Approach and landing	–	–	749	
Taxi in	0:30	–	2,719	
Diversion climb	0:19	92 (170)	1,656	
Diversion cruise	0:11	67 (124)	587	
Diversion descent	0:16	87 (161)	750	Trans. alt.: 25,300 ft
Loiter	0:30	79 (146)	1,726	
Optimized loiter	0:30	102 (189)	1,093	
Reserve	0:24	153 (283)	1,483	10% of cruise flight
Total SPP mission	6:20	1,866 (3,455)	25,972	
Total diversion	1:16	325 (601)	4,718	
Total overall	8:00	2,343 (4,339)	32,173	

The reason for the deficient performance on the design climb is an inappropriate specification of the Mach number for the second part it. The value of 0.52 is too low and takes the aircraft close to its operating limitation (maximum lift coefficient), when the cruise altitude of 29,000 ft is approached, cf. Figure 4.15. Therefore, drag increases and climb performance deteriorates. A similar observation can be made for the loiter segment. The preset CAS is not well chosen and leads to an increased fuel burn compared to an optimized loiter. In summary, a required mission fuel of 32,173 kg including reserves is determined, which is 4,273 kg more than the projected 27,900 kg.

Based on the known fuel burn for the different segments of the design mission, a payload-range diagram is derived (Figure 4.18). It incorporates the reserves and the diversion and loiter profile as specified for the design mission. The analysis is based on the design fuel mass of 27,900 kg and with this yields a design mission range of 1,423 NM (2,635 km), which is 445 NM (825 km) less than the projected range of 1,868 NM (3,460 km). With maximum payload a range of 932 NM (1,726 km) remains, while maximum fuel yields 5,077 NM (9,403 km). The ferry range without payload is 6,506 NM (12,050 km).

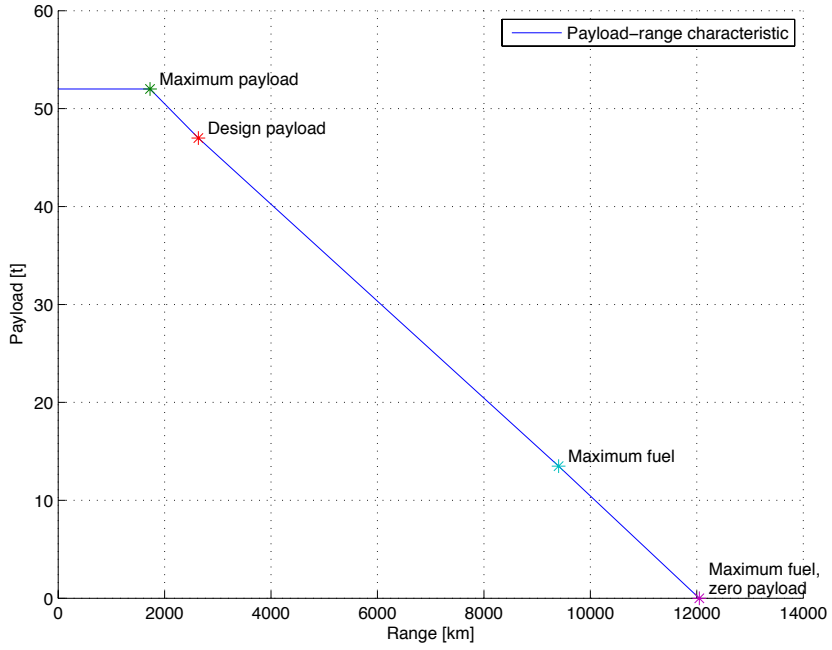

Figure 4.18: Payload-range diagram of the baseline Propcraft P-420/A concept, based on the design mission profile and allowing for reserves of 10% of the enroute time, a 250 NM diversion and a 30 min loiter

4.5 Comparison of the Results to the Requirements and the previous Data Status

Comparing the results of the analysis of the baseline Propcraft P-420/A concept with the design requirements shows differing accomplishment, as not all requirements are met.

The most critical aspect is the take-off performance in the second-segment climb. In this situation, thrust has already diminished significantly due to the aircraft's velocity. On the other hand, drag is high, as a relatively high lift coefficient is necessary and high-lift devices are deployed. The criticality is increased even further, as certification requires considering the one-engine-inoperative case, which yields only 75% thrust for the four-engined concept. As explained in Section 4.4.3.2, the baseline Propcraft P-420/A is not certifiable, because it fails the second-segment climb requirement. Hence, the second-segment climb is a major driver for the installed thrust-to-weight ratio and adjustments need to be made here. (cf. Howe 2000, p.176)

A second aspect regarding take-off performance is the field length. The analysis of the all-engines take-off yields a total take-off distance that is about 20% greater than the projected 1,800 m of the ICAO ARC 3. Moreover, the ICAO ARC requirement is actually based on the BFL, i.e., the one-engine-inoperative performance, which could not be evaluated for the baseline Propcraft P-420/A concept due to the failed climb performance requirement. Still the OEI performance is obviously worse than with all engines operating and, hence, it has to be acknowledged that the projected ARC category 3 cannot be met. Instead, ARC category 4 applies, which implies a balanced field length greater than 1,800 m. The goal of ARC 3 was very ambitious anyway, as can be seen when comparing the Propcraft concept to existing aircraft of the Airbus product fleet, all models of which are categorized under ARC 4, except for the A318, which is significantly lighter. (AIRBUS S.A.S. 2013c)

The second part of the ICAO ARC concerning the dimensions of the concept remains category D. The complete ARC of 4D is appraised reasonable, as comparison shows that the Airbus models A300 and A310 fall under the same category. (AIRBUS S.A.S. 2013c) Both have a similar maximum take-off weight as the baseline Propcraft P-420/A concept.

Besides the certification and reference code considerations, the analysis of the design mission revealed that the range requirement of a minimum of 3,000 km cannot be met with the projected amount of fuel. It is appraised, though, that this is mainly caused by

an inappropriate definition of the climb procedure and by the specification of extensive taxi times. Either with modifications to these specifications or with a slightly reduced passenger payload in favor of more mission fuel, the required range is achievable.

Similar to the take-off distance, also the predicted total landing distance exceeds the initial goal of 1,800 m. As the concept has to be categorized in a less restrictive ICAO ARC due to the balanced field length anyway, this is not severe though. Nonetheless, it can be stated that the landing distance could be reduced by restricting the maximum permissible landing mass, which is considered equal to the maximum take-off mass in the calculation carried out.

The described constraints to the baseline Propcraft P-420/A concept are visualized in a constraint diagram shown in Figure 4.19. The corresponding analysis is implemented in the IDT after Brandt et al. (2004, p.246). As the assumptions and empirical derivation of the equations after Brandt et al. are not exactly similar to the ones of the other calculations implemented in the IDT, the constraint diagram does not necessarily always match the other results. Nonetheless, for the analysis of the aircraft concept, the important aspects can be seen: Take-off and landing distances of 1,800 m cannot be acquired by the concept, yet, 2,400 m would be sufficient. The second-segment climb requirement is not met and the initial design cruise condition is also depicted.

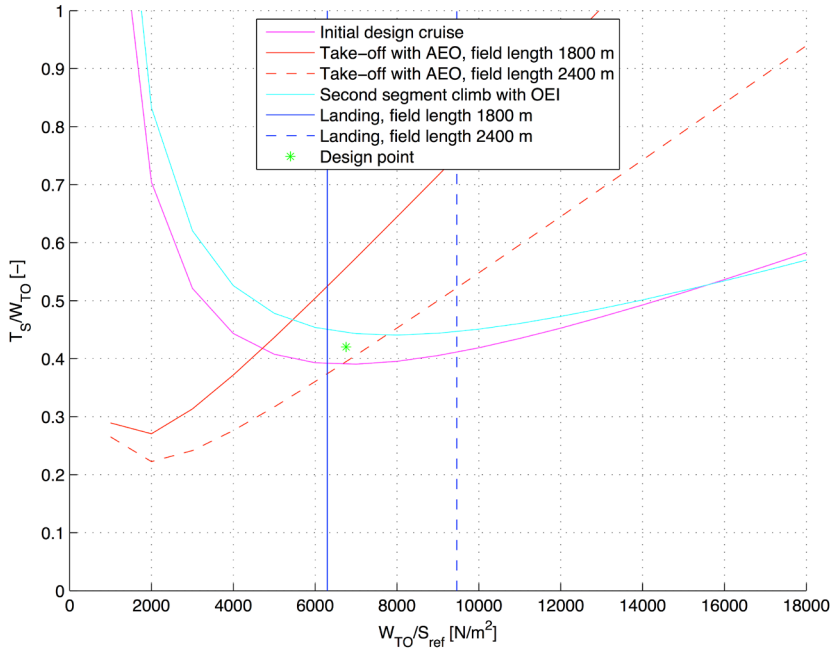

Figure 4.19: Constraint diagram of the baseline Propcraft P-420/A concept, based on the design mission configuration, take-off and landing constraints for field lengths of 1,800 m (solid lines) and 2,400 m (dashed lines)

In addition to checking the accomplishment of requirements and constraints, the results of the analysis of the baseline Propcraft P-420/A concept can be compared to the previous conceptual-phase data status elaborated by Iwanizki (2013) and Iwanizki et al. (2014). Some key differences are given below.

- Aerodynamics: In general, the methodology of lift prediction is similar to the one of Iwanizki. The influence of the Mach number on aerodynamics, however, is implemented more thoroughly in the IDT, i.e., distinguishing between slow, low, and cruise flight condition. The estimated values of maximum lift as well as the high-lift device considerations differ slightly from the previous data, cf. Iwanizki (2013, p.148). Furthermore, Iwanizki incorporated the propeller slipstream effect on lift in his calculations as described in Section 3.3.1.3. Due to a computation error, he obtained reasonable results that could not be reproduced within the scope of this work, cf. Section 4.1.1.4. The zero-lift drag prediction of this work is comparable to the previous one and yields a similar value. Considerable discrepancy occurs, though, in drag due to lift. Iwanizki does not allow for the variation of the drag-due-to-lift factor with lift coefficient. Hence, in this work, a slightly lower drag due to lift at low and moderate lift coefficients is predicted, a considerably higher drag, however, at high lift coefficients. The aerodynamic efficiency L/D in cruise flight of 18.47 is thus about 5% higher than the previously estimated value. Moreover, Iwanizki's prediction of an aerodynamic efficiency of about 18 at the take-off lift coefficient is unrealistic and corrected to a value of 9.22 with the calculations of this work, cf. Section 4.1.3.
- Masses: With 97.3 tons instead of 90.9 tons the operating mass empty of the aircraft concept is assessed 7% heavier in this work compared to the previous value. For his mass prediction, Iwanizki combined several mass estimation methods (Iwanizki 2013, p.137), which can produce inaccuracies due to component breakdown discrepancies. In general, the assessment of the predicted mass remains difficult, as a reference aircraft that is comparable to the Propcraft P-420/A concept does not exist.
- Propulsion: The general methodology of propulsion modeling is similar to the previous work. However, Iwanizki chose too high a rotational speed of the propeller of 16.7 rev/s, what deteriorates the propeller efficiency. In this work, 12 rev/s are employed instead, through which the propeller efficiency in cruise flight is increased from about 0.77 to 0.856, i.e., by about 11%. This has a direct influence on thrust, so that the static value is 177.4 kN compared to 157.3 kN previously. Furthermore, the developed fuel consumption model did not exist in

the previous analysis, where only a constant value was employed. (Iwanizki 2013, p.112) As the specific fuel consumption varies by some 20% depending on the operating condition (cf. Figure 4.8), a more accurate prediction of fuel burn is enabled through the model.

- Performance: Most of the aspects regarding the aircraft performance have been dealt with already in the context of requirement checking. The prediction presented in this work differs significantly from previous data as Iwanizki assessed all requirements and constraints to be accomplished. Both required take-off and landing field lengths are corrected to values greater than the projected 1,800 m. The predicted SPP mission fuel requirement is about 24% higher than previously or respectively the mission range only 2,635 km instead of 3,460 km. On the other hand, the predicted operating limitations of maximum Mach number and altitude are similar to Iwanizki's data.

In summary, the aircraft properties as predicted within the scope of this thesis are not as ambitious as Iwanizki estimated them. However, as described in the previous sections, the calculation methodologies applied and results obtained with the IDT are considered more realistic than the previous data. Critical aspects of the concept have been identified and although some design requirements are not met, improvement can be reached with feasible changes to the configuration.

5 Concept Revision and Design for Performance

The baseline Propcraft P-420/A concept, as it is investigated in Chapter 4, is not certifiable due to low second-segment climb performance, and does not meet the projected design mission range. In order to overcome these problems, modifications to the concept are introduced in this chapter and the refined P-420/B is recalculated with the IDT.

Regarding the ICAO ARC category of the concept, it is appraised not feasible to reduce the required take-off field length below 1,800 m and obtain ARC 3, cf. Section 4.5. However, the aircraft dimensions comply with ARC category D and thus remain unchanged in the revision process so that ICAO ARC 4D is maintained.

Both second-segment climb performance and the mission range of the aircraft concept are directly linked to the characteristics of aerodynamic drag and engine thrust. The aerodynamic efficiency of the concept is relatively high, cf. Section 4.1.3. In order to increase it even further, modifications to the geometrical layout of the concept would be necessary, e.g., an increased wingspan. This is refrained from, however, with respect to the intended ICAO ARC. Instead, the main focus of the concept revision lies on the engine characteristics.
Furthermore, the design mission specifications are reviewed and adapted to gain optimum performance of the aircraft concept.

The key results of the employed modifications and an updated verification of the design requirements and constraints conclude the chapter.

5.1 Propulsion Modifications

Take-off analysis revealed that in the second-segment climb, the difference between thrust and drag of the baseline Propcraft P-420/A concept is not sufficient to maintain a minimum climb rate in the one-engine-inoperative case. A simple solution would be to increase the power rating of the engines, but this implies extended part-load operation in other flight conditions, which generally deteriorates efficiency. More problem-oriented is the approach to allow the engine power to be increased by ram effects not only in high flight altitudes, but also already during the climb. (Mair and Birdsall 1992, p.103)

5.1.1 Torque Limit

As described in Section 3.5.1, Iwanizki's engine model restricts power to the value of the static MSL power rating due to a supposed engine torque limit. This represents a maximum acceptable stress level in the power train of the engine, i.e., spools, gearboxes, propeller drive. The value of this limit can be considered as a technological parameter that has to be determined during the engine development phase in a tradeoff between achievable engine power and structural component weights. The engine data presented by Nicolai and Carichner (2010, p.803) show a torque limit at about 110% of the static MSL power rating. This characteristic is transferred to the power model of the Propcraft P-420/B concept, which yields a torque limit at 10,670 kW, cf. Figure 5.1. With this higher torque limit, the available power in the second-segment climb with one-engine inoperative at a Mach number of 0.27 is increased by about 5%.

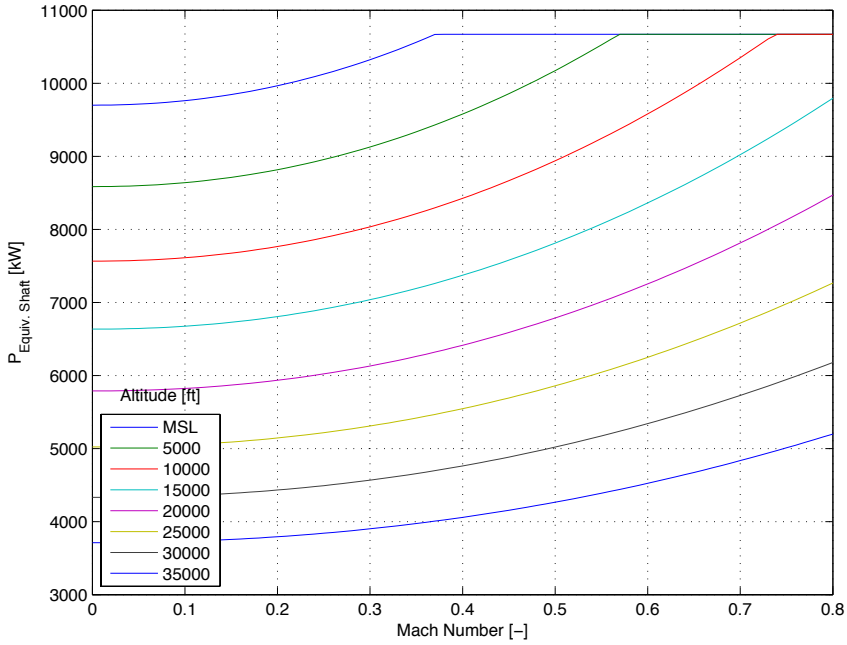

Figure 5.1: Modified equivalent power characteristic of a single engine of the Propcraft P-420/B concept, torque limit at 110% of the static MSL power rating

5.1.2 Propeller Efficiency Adjustment

The value of 0.856 of the propeller efficiency in cruise flight obtained with the estimation method as described in Section 3.5.3 seems fairly moderate when it is compared to references stating that typical efficiencies of modern propellers range from 0.85 to 0.92, cf. Torenbeek (1982, p.191) and Bräunling (2009, p.502).

Additionally, the Propcraft P-420 concept is intended to be equipped with dual counter-rotating propellers that increase efficiency even further. Measurements on the counter-rotating CRP-X1 propeller have proven an efficiency of 0.9 in cruise flight conditions feasible. (Zimmer 1994, p.162, 189) Aerosila, the manufacturer of the Antonov An-70's counter-rotating propeller SV-27, also claims a cruising efficiency of 0.9, cf. AEROSILA (2005).

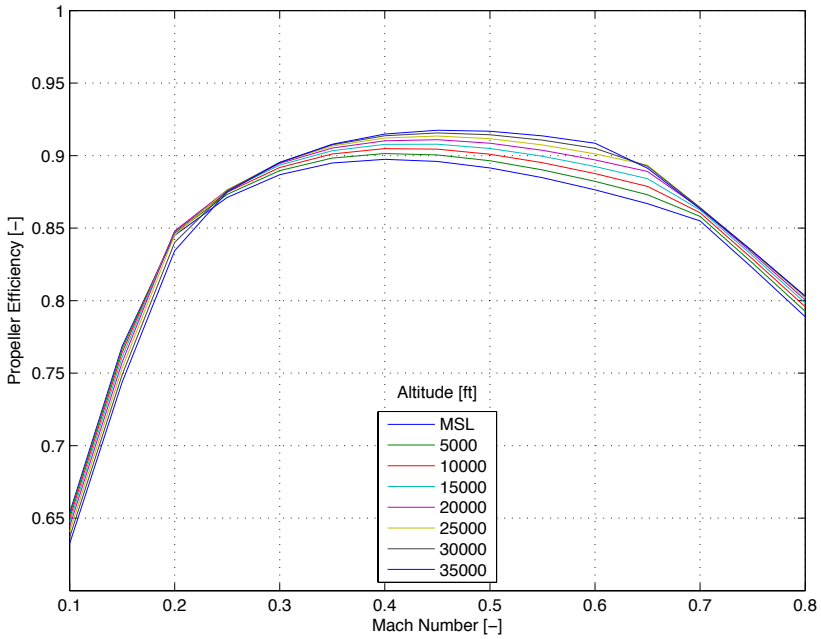

Figure 5.2: Propulsive efficiency characteristic of the propeller of the Propcraft P-420/B concept with an additional fudge factor to meet an efficiency of approximately 0.9 in the design cruise flight condition

In order to align the propeller efficiency estimation of the Propcraft P-420/B concept with these reference values, a fudge factor is introduced to the prediction method. This factor is tuned to yield a propeller efficiency of approximately 0.9 in the design cruise condition of the concept. In the applicable aircraft operating range the predicted values of the propeller efficiency vary then from about 0.845 to about 0.915 (cf. Figure 5.2), which accords well with the efficiency span stated by Torenbeek and Bräunling.

5.1.3 Referencing of the Engine Fuel Consumption

Besides engine power and propeller efficiency, the assumed specific fuel consumption is reviewed. After Iwanizki (2013, p.112), a reference value of an equivalent power-specific fuel consumption of 1.7956 N/kW/h in the design cruise flight condition is employed, cf. Section 3.5.2. In combination with the fuel consumption model developed in this work, this yields a take-off fuel consumption of 2.291 N/kW/h. Bräunling (2009, p.327, 329) states that modern turboprop engines feature equivalent power-specific fuel consumptions in take-off condition ranging from about 2.45 N/kW/h to about 2.94 N/kW/h. Hence, the value after Iwanizki is appraised quite ambitious, as it is well below the lower limit of the interval indicated by Bräunling.

According to in-house data of the Technische Universität München, Institute for Flight Propulsion, the Europrop International TP400 engine of the Airbus A400M has a shaft power-specific fuel consumption of 2.2359 N/kW/h in cruise flight. (Hupfer 2012, p.63) As the TP400 is a powerful modern Western turboprop engine, this value is regarded as a good reference for the current level of technology. With an assumed difference of 5% between shaft and equivalent power (cf. Section 3.5.1), the value is converted to an equivalent power-specific fuel consumption of 2.1294 N/kW/h, which is employed to calibrate the fuel consumption model of the Propcraft P-420/B concept, cf. Figure 5.3. For take-off conditions, the model yields a specific fuel consumption of 2.625 N/kW/h, which is in good agreement with the value range specified by Bräunling.

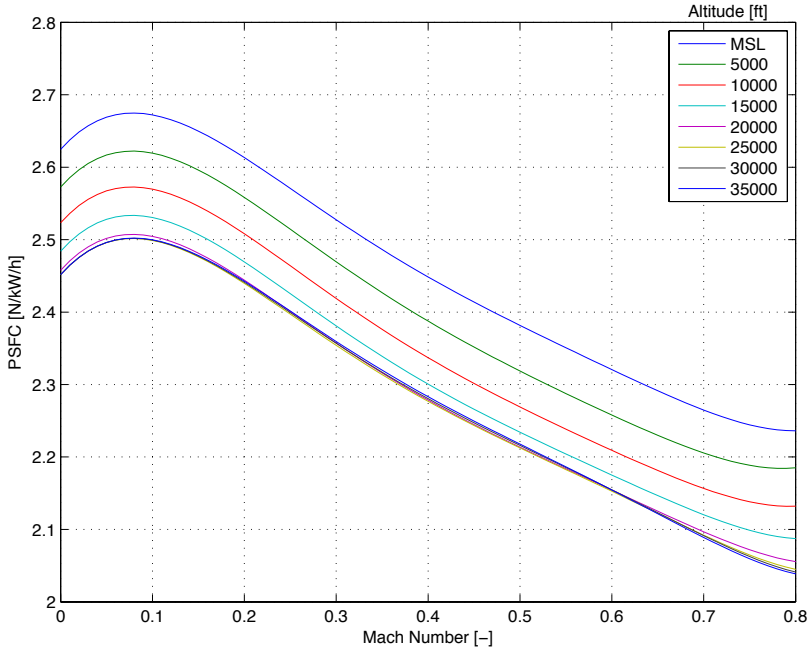

Figure 5.3: Equivalent power-specific fuel consumption characteristic of a single engine of the Propcraft P-420/B concept, calibrated with a reference value of the TP400 engine

5.2 Optimized Design Mission Specification

The analysis of the design mission performance of the baseline Propcraft P-420/A concept revealed some unfavorable specifications, which are corrected in this section. Firstly, the extensive taxi times are reduced to reasonable values as suggested by Raymer (2012, p.729). Both taxi-out and taxi-in times are specified with 15 minutes, respectively.

Furthermore, the airspeed for the climb to cruise altitude with constant CAS was set too low at a value of 210 kts, which results in a long climbing time with an increased fuel burn. Based on the carried-out calculation of an optimum climb with the airspeed for the best climb rate, a constant CAS of 231 kts is identified as an optimum value. This speed is confirmed by the SEP analysis, as shown in Figure 4.14 and Figure 4.15, where the maximum specific excess power is reached at Mach numbers corresponding to 231 kts. For best overall climb performance, the constant Mach number for the second segment of the climb to cruise altitude is changed from 0.52 to 0.58. Again, this yields maximum SEP, cf. Figure 4.14 and Figure 4.15.

For the reserve requirements, a diversion flight of 250 NM was considered. However, this range is only required for long range aircraft. As the Propcraft P-420 is a short- to medium-range concept, it only needs to provide reserves for a 200 NM diversion. (Torenbeek 2013, p.387)

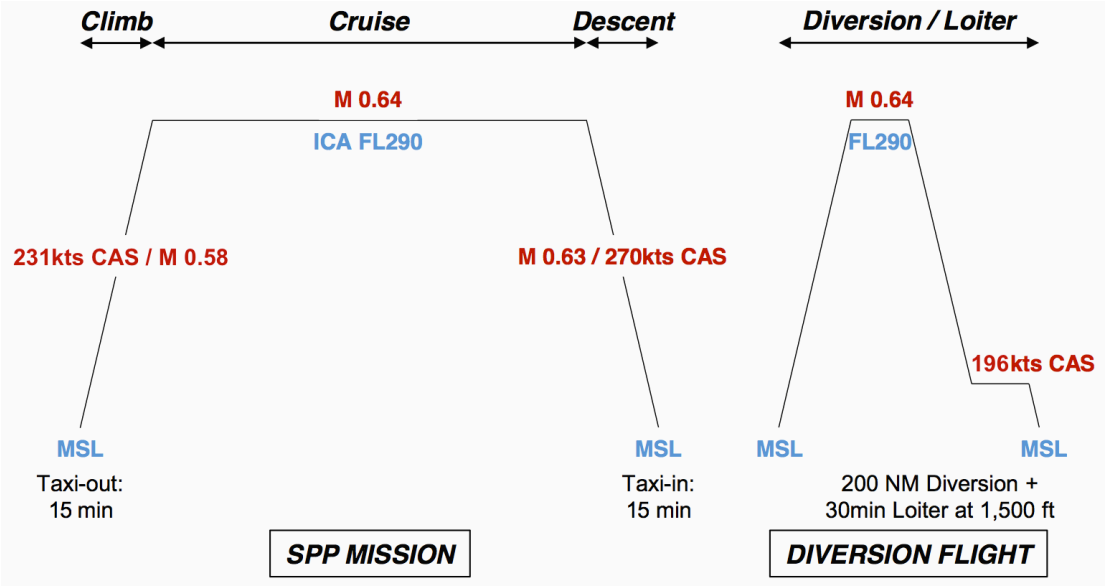

Figure 5.4: Revised design mission specifications of the Propcraft P-420/B concept (modified from Randt 2014b)

Finally, the airspeed during loiter is adjusted. Again, the previously adopted 150 kts were set too low and resulted in an increased fuel burn. Resulting from the evaluation of the airspeed for minimum required power, the optimum loiter CAS is identified as 196 kts and specified in the mission profile accordingly.

The whole design mission with the adapted specifications is visualized in Figure 5.4.

5.3 Results of the Revised Configuration and Efficiency Assessment

With the modified engine characteristics the Propcraft P-420/B concept features more thrust, which improves take-off performance. A drawback, however, is the increased fuel consumption. On the other hand, an optimized specification of the design mission enhances fuel efficiency. The results of the revised aircraft performance calculations are presented in the following and its efficiency is assessed.

The required field length for a take-off with all engines operating is reduced by slightly more than 6% to 2,018 m (calculated with the method after Raymer, cf. Section 4.4.3.1). In the case with one engine inoperative, the second segment climb requirement is now fulfilled. A climb angle of about 0.038 rad is attained that exceeds the needed 0.03 rad and, hence, enables the certification of the modified concept. With this, a balanced field length can be calculated according the method after Torenbeek, cf. Section 4.4.3.2, resulting in 3,452 m.

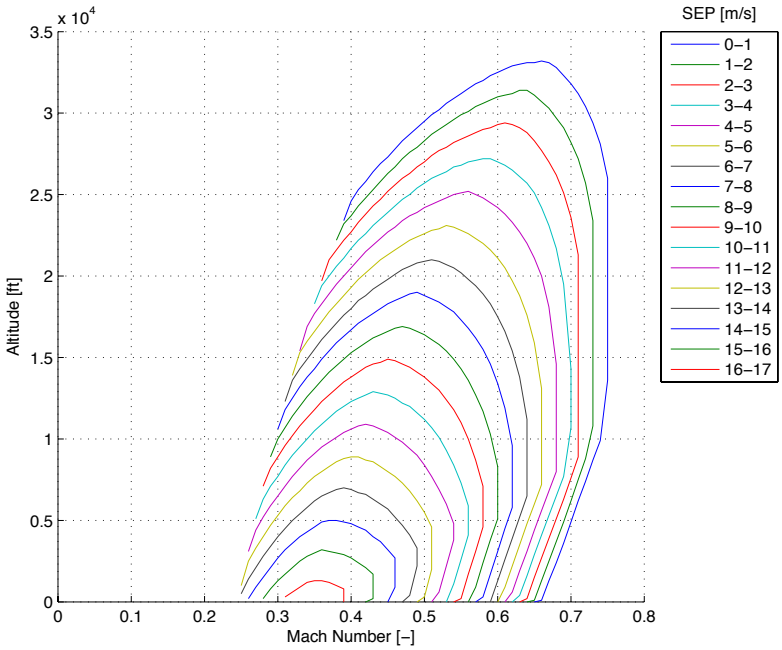

Figure 5.5: Specific excess power contours over the operating ranges of flight Mach number and altitude of the Propcraft P-420/B concept with estimated initial cruise weight

Due to the increased thrust, the operating range of the aircraft is slightly increased. Service ceiling and maximum operating altitude are each increased by 1,000 ft to 32,300 ft and 33,200 ft, respectively. The maximum operating Mach number is 0.75, a plus of 0.01. The revised specific excess power contours are shown in Figure 5.5.

The updated constraint analysis diagram is depicted in Figure 5.6. It can be seen that in this configuration the design point is well chosen. Both the second segment climb requirement with OEI and the initial design cruise condition constraint are met in a configuration with roughly the minimum necessary engine thrust.

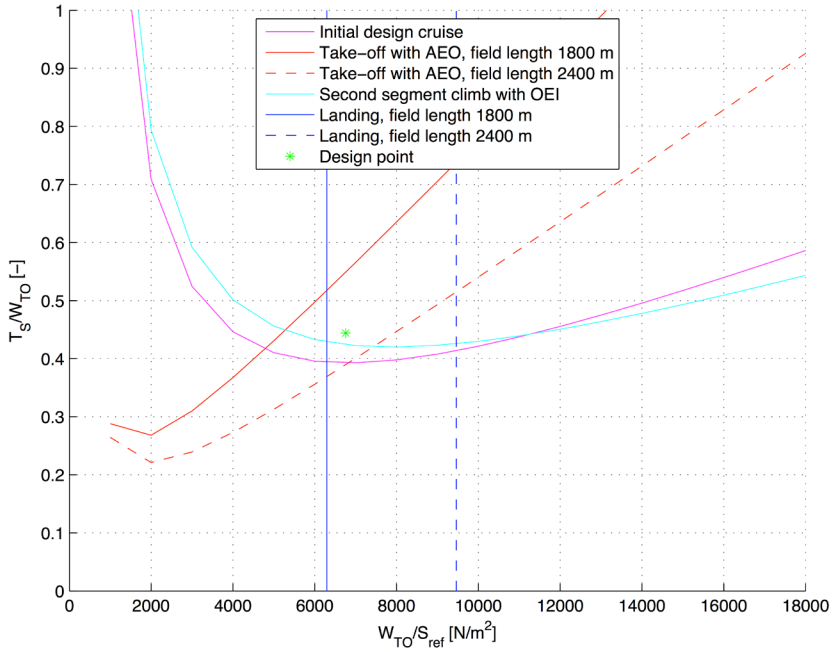

Figure 5.6: Constraint diagram of the Propcraft P-420/B concept, based on the design mission configuration, take-off and landing constraints for field lengths of 1,800 m (solid lines) and 2,400 m (dashed lines)

With respect to the intended application case of the aircraft concept, the payload-range and fuel consumption characteristics are of particular interest. Here, the increased value of the specific fuel consumption of the engines counteracts the performance gains through higher available thrust. With the originally projected design payload of 420 passengers plus 5 tons of cargo and the design fuel mass of 27,900 kg, an SPP mission range of 1,592 NM (2,948 km) is attained. Hence, the originally projected value of 1,868 NM (3,460 km) is missed by far, but the design requirement of a range of at least 1,620 NM (3,000 km) is almost accomplished.

As the design passenger capacity requirement of minimum 300 is well exceeded, it is still possible, however, to extend the range by trading payload for fuel. Reducing the

passenger payload on the design mission from 420 to 416 is enough to yield a design mission range of 1,621 NM (3,003 km) at a total payload of 46.6 tons. This configuration meets all design requirements and is depicted as the design mission point in the payload-range diagram in Figure 5.7. Of course further range extension is possible by reducing the payload. With a typical air transport passenger load factor of 80% (IATA Economics 2014), i.e., here 336 passengers, a mission range of 2,347 NM (4,347 km) is possible with a mission fuel of 36,300 tons.

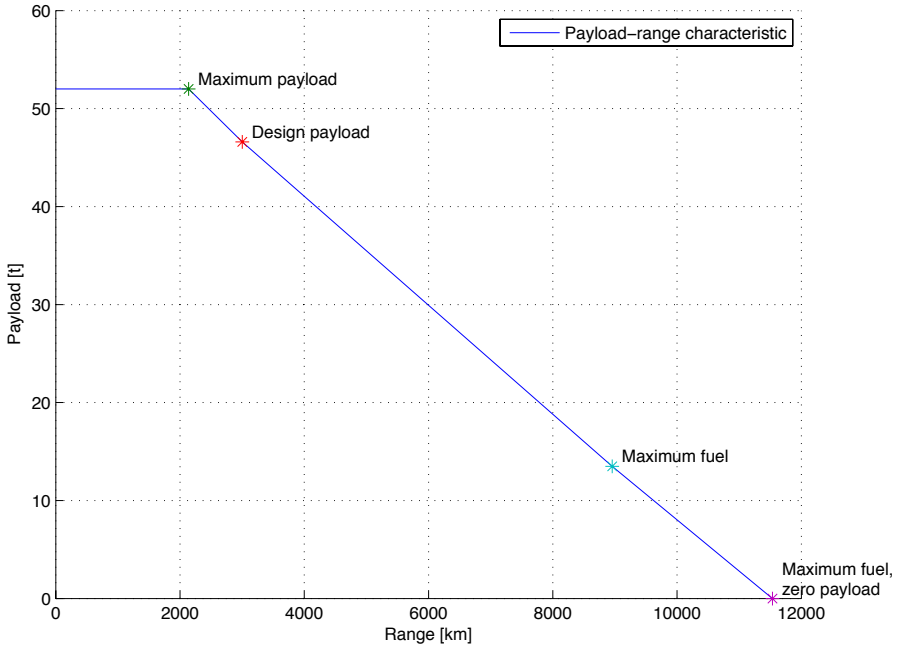

Figure 5.7: Payload-range diagram of the Propcraft P-420/B concept, based on the optimized design mission profile and allowing for reserves of 10% of the enroute time, a 200 NM diversion and a 30 min loiter

The other data points in Figure 5.7 represent the configuration with maximum payload at a range of 1,154 NM (2,138 km), the maximum fuel range of 4,836 NM (8,956 km) and the ferry range of 6,226 NM (11,530 km).

Besides the payload-range characteristics, an important aspect of the Propcraft P-420 concept is its efficiency, as it is conceptualized to reduce the fuel consumption of air transport operations on highly frequented short- to medium-range routes and the corresponding environmental impact. However, it is difficult to find a meaningful quantification of the efficiency of an aircraft, because it is strongly dependent on the specific operational circumstances of an airline. One attempt is the theoretical fuel efficiency at maximum-payload range after Randt (2014b) as defined in Equation (2.1). For the Propcraft P-420/B concept, it yields a value of 0.255 l/t/km. The previous baseline version was assessed at 0.212 l/t/km, cf. Section 2.2.3.

A comparison to the data of other aircraft compiled by Randt (2014a) is given in Table 5.1. It shows that according to the theoretical fuel efficiency, the revised concept is more fuel efficient than the other listed aircraft, especially than the turboprop-driven ones. The only exception is the Airbus A330, which is even more efficient according to these values.

The collection of the theoretical fuel efficiency data of the other aircraft, however, raises doubts on the applicability of this metric to compare aircraft. All of the turboprop-powered aircraft in the list show higher values than the models equipped with turbofan engines. This is contradictory to the fact that turboprop engines can principally attain higher efficiencies. (Howe 2000, p.62) An aspect that possibly corrupts the validity of the theoretical fuel efficiency is that it is evaluated at maximum-payload range. This configuration is hardly comparable, however, as both the structure of the payload and the profile of the respective design mission vary greatly among the different configurations, e.g., civil or military application, short- or long-range operation, and so on. As the aircraft designs are essentially driven by the specific payload and mission requirements, the maximum-payload range, which is not the design mission, is not necessarily a good indicator for efficiency.

Table 5.1: Theoretical fuel efficiency values at maximum-payload range as defined by Randt (2014b) for the Propcraft P-420/B concept and several other transport category aircraft, data from Randt (2014a)

Theoretical fuel efficiency	l/t/km
Propcraft P-420/B	0.255
Antonov An-70	0.296
Airbus A400M	0.276
Lockheed C-130J Hercules	0.367
ATR72-200	0.378
ATR72-500	0.312
Bombardier CRJ200ER	0.267
Airbus A320-200	0.274
Airbus A330-300	0.233

Another value to compare the fuel efficiency of aircraft is the specific fuel consumption in liters of fuel consumed per passenger and per 100 kilometers of flight. This measure is again dependent, however, on the specific operation of the aircraft, especially on the passenger load factor. With its design fuel mass of 27.9 tons, the Propcraft P-420/B concept achieves a value of 2.79 l/PAX/100 km on its design mission with the design

payload of 420 passengers and 5 tons of cargo. With 336 passengers (passenger load factor of 80%) and the corresponding fuel mass of 36.3 tons, a specific fuel consumption of 3.07 l/PAX/100 km remains. To give a reference value for comparison: The fleet of German airlines had an average fuel consumption of 3.68 l/PAX/100 km in the year 2013. (BDL 2014) The Propcraft P-420/B concept is, hence, on the basis of a passenger load factor of 80% about 16.6% more fuel efficient than the German airline fleet, which possesses a similar average load factor of 81%. (BDL 2014) However, one has to consider that the averaged value of the fleet fuel consumption includes both long-range aircraft that generally have lower specific fuel consumptions as well as short- and medium-range models, which usually operate with higher values. According to the BDL (2013), the actual specific fuel consumption on short- and medium-range flights of the German airline fleet in 2013 ranged from 2.6 to 4.2 l/PAX/100 km.

In summary, it has to be acknowledged that the Propcraft P-420 concept promises increased fuel efficiency and with this reduced greenhouse gas emissions on its design mission. This result has to be credited only to the specific design of the concept for its application as a high-capacity transport aircraft on short- to medium-range routes. As the design is based only on currently available technology, future technological innovations may contribute additionally. The quantification of an economic or ecological advantage is difficult, however, because it is strongly dependent on the specific operation of the aircraft.

6 Conclusion and Future Work

The continually rising demand for worldwide air transport in combination with globally observable urbanization processes lead to increasing congestion of air traffic flows, especially between major hub airports. In the three main air transport regions of the world, Asia/Pacific, Europe and North America, further growth of the aviation economy is increasingly constricted by aircraft-handling capacities both on the ground and in the air. In order to meet growing passenger demand, airlines thus operate larger aircraft. Current large aircraft are generally designed for long-range operation. However, the vast majority of performed flights only cover short- to medium-range distances.
At the Institute of Aircraft Design of the Technische Universität München, possibilities are investigated to overcome the aviation growth constraints and to increase economic and ecological efficiency of aircraft operations. In this context, starting from a thorough market analysis, a turboprop-powered high-capacity aircraft concept has been developed that is designed specifically for short- to medium-range operation.

Within the scope of this work a comprehensive analysis of the baseline version of this aircraft concept, named Propcraft P-420/A, has been performed with special regard to its operational performance. For this, an integrated aircraft design tool (IDT) has been developed and implemented in the MATLAB environment. Based on a parametric definition of the aircraft concept, the IDT performs various analyses in order to predict characteristics in aerodynamics, masses, and propulsion. Combining these results, performance calculations are carried out that allow sophisticated statements on operational characteristics and efficiency. The calculation methods employed in the IDT are based on common aircraft design practice, yet extended by own models and calibration data.

The following key methods were employed for the aerodynamic investigation of the baseline Propcraft P-420/A concept. Based on a two-dimensional airfoil and a three-

dimensional wing analysis, lift characteristics were evaluated for slow, low, and for cruise flight. The effects of high-lift device configurations with leading-edge slats and trailing-edge single- or double-slotted Fowler flaps were calculated and compared for a take-off and an approach setting. Drag analysis was subdivided into zero-lift drag, drag due to lift and high-lift device drag increments. Several calculation methods are implemented in the IDT, of which a component buildup method was selected for zero-lift drag prediction and a leading-edge-suction approach for drag due to lift.
In design cruise flight the drag polar shows a lift-to-drag ratio of 18.47. A high-lift system with slats and single-slotted Fowler flaps was selected for the concept. At a take-off angle of rotation of 8°, a lift-coefficient of 1.84 is reached at an aerodynamic efficiency L/D of 9.22. During approach and landing, a lift-coefficient of up to 2.32 would be required in the theoretical case of a landing at MTOM, which accords to an angle of attack of 9°, and is feasible without restriction.

The prediction of the operating mass empty of the investigated aircraft concept was performed with several methods to allow for comparisons. All of them are based on a component breakdown and separate estimation of the component weights. For some structural items, fudge factors were introduced to allow for weight reductions due to the application of advanced composite materials. Of the applied mass prediction methods, the one was selected that best represents the characteristics of the investigated concept, e.g., the turboprop engines and the double-deck cabin layout. The result is an operating mass empty of 97.3 tons and a corresponding maximum take-off mass of 172.2 tons.

Predicting the propulsion characteristics of the turboprop engines of the Propcraft P-420 concept consists of the aspects of available engine power, propulsive efficiency of the propeller, attainable thrust, and specific fuel consumption. For each of these, a model is employed that describes the dependency of the corresponding value on flight Mach number and altitude. The model of the available engine power was derived from published data of an Allison turboprop engine. Propeller efficiency was obtained in a multi-stage process according to published aircraft design practice. Thrust is then given as a function of power, propeller efficiency, and flight velocity. A model for the engine fuel consumption was developed on the basis of published data of the Allison engine.
Important results are that in cruise flight, the engine power drops down to about 58% of its static MSL rating of 9,700 kW, while a propeller efficiency of 0.856 is reached. Specific fuel consumption is found to vary by some 20% with decreasing values at higher Mach numbers and in greater altitudes.

With these results, performance calculations were carried out covering operating limitations, take-off, landing, and the analysis of a design mission profile with diversion and loiter. Besides other results, take-off performance and mission fuel consumption were identified as critical aspects of the configuration. Certification specifications require a minimum climb rate in the second-segment climb of take-off with one engine inoperative. This requirement is not met by the baseline Propcraft P-420/A concept. Additionally, the predicted field length – even with all engines operating – considerably exceeds the projected 1,800 m, which would have allowed the aircraft to be categorized in ICAO ARC 3D. This requirement cannot be met by the concept and the ICAO ARC is thus adjusted to 4D. Furthermore, increased fuel consumption on the design mission is caused by unfavorable specifications of operational parameters. This reduces the design mission range from originally projected 1,868 NM (3,460 km) to 1,423 NM (2,635 km), which fails the design requirement of a minimum range of 1,620 NM (3,000 km).

In order to overcome the performance problems, the baseline Propcraft P-420/A concept was revised, at which a main focus lay on the propulsion characteristics. In accordance with reference data of the Allison engine, the torque limit that restricts the maximum engine power was raised. This allows power to increase through ram effects to values greater than the static rating. The propeller of the Propcraft P-420 is conceptualized as a dual counter-rotating configuration. However, the propeller efficiency calculation is based on conventional propellers. Therefore, a fudge factor was introduced that raises the propulsive efficiency of the propeller to 0.9 in cruise flight, a realistic value for counter-rotating configurations according to the consulted references. A third aspect of the revisions was the specific fuel consumption of the engine. The reference value that was adopted during the concept development is assessed too ambitious, as it is well below the fuel consumption range of modern turboprop engines reported in references. The calibration of the employed fuel consumption model was thus updated to about 15% higher values. This new reference was specified on the basis of in-house data of the Technische Universität München on the Europrop International TP400 engine.
Besides, the design mission specifications were revised with regard to realistic taxi times, optimized climb performance, and fuel-efficient loiter flight.

Resulting from the modifications, the revised Propcraft P-420/B concept is certifiable, as it matches the take-off climb requirement. The take-off field length with all engines operating is 2,018 m, while the one-engine-inoperative case yields 3,452 m. For landing, a field length of 2,022 m is necessary. The evaluation of operating limitations resulted in a service ceiling of 32,300 ft and a maximum operating Mach number of 0.75.

In terms of mission performance, the increased engine power and higher propeller efficiency are compensated by the increased fuel consumption. With the design payload of 420 passengers plus 5 tons of cargo, and the design mission fuel mass, a range of 1,592 NM (2,948 km) is attained. To meet the design requirement of a minimum range of 1,620 NM (3,000 km), the payload has to be reduced to 416 passengers, which yields a mission range of 1,621 NM (3,003 km). As the original requirement specified a minimum passenger number of only 300, the reduction from 420 to 416 is acceptable. With a typical passenger load factor of 80% the mission range can be extended to 2,347 NM (4,347 km). In this case, the Propcraft P-420/B achieves a specific fuel consumption of 3.07 l/PAX/100 km. This is about 16.6% more fuel efficient than the average value of the German airline fleet in 2013.
Hence, the Propcraft P-420 concept promises to ease congestion on highly frequented short- to medium-range air traffic routes, while increasing fuel efficiency and reducing environmental impact. The advantages of the aircraft result only from the specific design as a high-capacity aircraft for short- to medium-range operations. Novel technologies were not considered in the concept and remain complementary.

On the basis of this result, some suggestions for future work are given in the following. Through its parametric approach, the IDT provides the opportunity to perform further design studies on the Propcraft P-420 concept. A starting point could be the question, whether it is beneficial for the aircraft to abolish the ICAO ARC 4D requirement and accept 4E instead. This would allow the selection of a wingspan greater than 52 m and could thus increase the aerodynamic efficiency, possibly in combination with a higher aspect ratio. In order to appraise the relevance of the ICAO ARC category for the operational flexibility of the aircraft, an evaluation of the available airport infrastructure in relevant regions, especially the growing markets in Asia, could provide new insights.

In order to enable a more substantiated assessment of the efficiency of the Propcraft P-420 concept, the performance and fuel burn of a currently available reference aircraft on the design mission of the concept could be of interest. With regard to the passenger capacity, possible reference aircraft could be an Airbus A330 or two Airbus A320. Comparison of the fuel consumption of the Propcraft P-420 concept to the one of the reference aircraft allows a meaningful appraisal of the fuel-saving potential. A corresponding approach is taken and described by Kenway et al. (2010).

Another important topic that has not yet been investigated in detail is aircraft noise. The Propcraft P-420/B propellers are conceptualized with rotational speed so low that the tip Mach number remains below 0.9 throughout the operating range, which yields an “ac-

ceptable" noise level according to Torenbeek (1982). But despite such noise mitigation measures, one has to suppose that due to its high-power turboprop engines the concept is significantly louder than comparable turbofan-powered aircraft. Depending on local governmental and airport regulations, this could either increase the operating costs or even prohibit the operation of the aircraft completely.
A radical approach to solve the noise problem of the Propcraft P-420 concept could be a complete redesign with turbofan engines instead of the turboprops, possibly with modern fuel-efficient geared turbofans (GTF). However, this requires extensive enhancements to the IDT, which is currently only capable of modeling turboprop engines.

Independent of the investigation of a specific concept, the IDT could be further developed towards an aircraft design tool with comprehensive functionality. Also from this point of view, the already-mentioned capability to model turbofan engines is of interest. Furthermore, a reasonable extension to the mass estimation module would be a center of gravity calculation that determines the center of gravity of the aircraft from its geometry and the predicted component masses. In combination with the aerodynamic analysis, this would allow the assessment of longitudinal and lateral stability. These are only few ideas, however, as the IDT principally offers many possibilities for ongoing development.

References

AEROSILA. 2005. *The SV-27 feathering-reversible puller coaxial hydromechanic propfan* [Online]. Stupino, Moscow, Russia. Available: http://en.aerosila.ru/index.php?actions=main_content&id=32 [Accessed 26th August 2014].

AIR CANADA 2014. Flight Timetable and Schedule. Dorval, Canada.

AIRBUS S.A.S. 2013a. *Airbus' newest A330 version: "The right aircraft, right now" for domestic and regional operations* [Online]. Blagnac Cedex, France. Available: http://www.airbus.com/newsevents/news-events-single/detail/airbus-newest-a330-version-the-right-aircraft-right-now-for-domestic-and-regional-operati/ [Accessed 27th July 2014].

AIRBUS S.A.S. 2013b. *Future Journeys: Global Market Forecast 2013-2032* [Online]. Blagnac Cedex, France. Available: http://www.airbus.com/company/market/forecast/?eID=dam_frontend_push&docID=33755 [Accessed 27th July 2014].

AIRBUS S.A.S. 2013c. ICAO Aerodrome Reference Code, FAA Airplane Design Group and Aircraft Approach Category for Airbus Aircraft. Blagnac Cedex, France.

AIRBUS S.A.S. PRESS DEPARTMENT 2013. Airbus announces lower weight A330 for regional & domestic operations. Blagnac Cedex, France.

BDL. 2013. *Berechnung des durchschnittlichen Treibstoffverbrauchs der deutschen Luftfahrt* [Online]. Berlin, Germany: Bundesverband der Deutschen Luftverkehrswirtschaft BDL. Available: http://www.die-vier-liter-flieger.de/de/die-berechnung/ [Accessed 12th September 2014].

BDL 2014. Energieeffizienz und Klimaschutz Report 2014. Berlin, Germany: Bundesverband der Deutschen Luftverkehrswirtschaft BDL.

BOEING COMMERCIAL AIRPLANES. 2013. *Current Market Outlook 2013–2032* [Online]. Seattle, WA, USA. Available: http://www.boeing.com/assets/pdf/commercial/cmo/pdf/Boeing_Current_Market_Outlook_2013.pdf [Accessed 27th July 2014].

BRANDT, S. A., STILES, R. J., BERTIN, J. J. & WHITFORD, R. 2004. *Introduction to Aeronautics: A Design Perspective*, Second Edition, Reston, VA, USA, American Institute of Aeronautics and Astronautics AIAA.

BRÄUNLING, W. J. G. 2009. *Flugzeugtriebwerke: Grundlagen, Aero-Thermodynamik, ideale und reale Kreisprozesse, Thermische Turbomaschinen, Komponenten, Emissionen und Systeme*, 3., vollst. überarb. u. erw. Aufl., Berlin, Heidelberg, Germany, Springer-Verlag.

CAVALLO, B. 1966. Subsonic Drag Estimation Methods. NADC-AW-6604. U.S. Naval Air Development Center.

CHAPELON, R. 2006. Indien-Special: Indiens Luftverkehr boomt. *Planet Aerospace.* EADS.

DRELA, M. & YOUNGREN, H. 2013. *XFOIL Subsonic Airfoil Development System* [Online]. Boston, MA, USA: Massachusetts Institute of Technology (MIT). Available: http://web.mit.edu/drela/Public/web/xfoil/ [Accessed 9th August 2014].

EASA 2013. Type-Certificate Ratier-Figeac FH385/FH386 Series Propeller. Cologne, Germany: European Aviation Safety Agency EASA.

EUROPEAN COMMISSION HIGH LEVEL GROUP ON AVIATION RESEARCH 2011. Flightpath 2050 Europe's Vision for Aviation. Luxembourg: Publications Office of the European Union.

FEDERAL AVIATION ADMINISTRATION 2011. Guide Specification for Aircraft Rescue and Fire Fighting (ARFF) Vehicles. Washington, DC, USA: U.S. Department of Transportation.

FINCK, R. D., ELLISON, D. E. & MALTHAN, L. V. 1978. USAF Stability and Control DATCOM. Wright-Patterson Air Force Base, OH, USA: Flight Dynamics Laboratory, Air Force Wright Aeronautical Laboratories, Air Force Systems Command.

GILMAN JR., J. 1953. Propeller-Performance Charts for Transport Airplanes. Washington, D.C., USA: National Advisory Committee for Aeronautics NACA Langley Aeronautical Laboratory.

HOERNER, S. & BORST, H. 1975. *Fluid Dynamic Lift*, Bricktown, NJ, USA, Hoerner Fluid Dynamics.

HOWE, D. 2000. *Aircraft Conceptual Design Synthesis*, London and Bury St Edmunds, UK, Professional Engineering Publishing.

HUPFER, A. 2012. Konstruktionsaspekte bei Flugantrieben. Garching bei München, Germany: Institute for Flight Propulsion, Technische Universität München.

IATA ECONOMICS 2014. Air Passenger Market Analysis July 2014. Montreal, Canada: International Air Transport Association IATA.

ICAO 2013. Aerodromes. *Annex 14 to the Convention on International Civil Aviation.* 6th ed. Montréal, Quebec, Canada: International Civil Aviation Organization ICAO.

ICAO ECONOMIC AND POLICY SECTION 2014. 2013: Air Transport Yearly Monitor (Preliminary). *Economic Development of Air Transport.* International Civil Aviation Organization ICAO.

ITTEL, J. 2014. *Developing a software tool for comprehensive flight performance and mission analyses in the context of the assessment of a novel turboprop transport aircraft concept.* Master's Thesis, Technische Universität München.

IWANIZKI, M. 2013. *Vorentwurf einer schweren, Propellerturbinen-getriebenen Verkehrsflugzeugkonfiguration für den Einsatz auf hochfrequentierten Kurz- und Mittelstrecken.* Master's Thesis, Technische Universität München.

IWANIZKI, M., RANDT, N. P. & SARTORIUS, S. 2014. Preliminary Design of a Heavy Short- and Medium-Haul Turboprop-Powered Passenger Aircraft. *52nd Aerospace Sciences Meeting.* American Institute of Aeronautics and Astronautics AIAA.

KENWAY, G. K. W., HENDERSON, R., HICKEN, J. E., KUNTAWALA, N. B., ZINGG, D. W., MARTINS, J. R. R. A. & MCKEAND, R. G. Reducing Aviation's Environmental Impact Through Large Aircraft For Short Ranges. 48th AIAA Aerospace Sciences Meeting and Exhibit, 2010 Orlando, Florida, USA.

KOREAN AIR 2014. Domestic Flight Timetable. Seoul, South Korea.

LOWRY, J. G. & POLHAMUS, E. C. 1957. A Method for Predicting Lift Increments due to Flap Deflection at Low Angles of Attack in Incompressible Flow. NACA Technical Note 3911. Langley Field, VA, USA: National Advisory Committee for Aeronautics (NACA).

MAIR, W. A. & BIRDSALL, D. L. 1992. *Aircraft Performance*, Cambridge, UK, Press Syndicate of the University of Cambridge.

MATTINGLY, J. D., HEISER, W. H. & PRATT, D. T. 2002. *Aircraft Engine Design*, 2nd ed., Reston, VA, USA, American Institute of Aeronautics and Astronautics AIAA.

NG, J. 2014. *Boeing Considering 787-Size Medium-Range Jetliners* [Online]. The Wall Street Journal. Available: http://online.wsj.com/news/article_email/SB10001424052702303874504579376150480867812-lMyQjAxMTA0MDEwMTExNDEyWj [Accessed 27th July 2014].

NICOLAI, L. M. & CARICHNER, G. E. 2010. *Fundamentals of Aircraft and Airship Design*, Rev. and expanded ed., Reston, VA, USA, American Institute of Aeronautics and Astronautics AIAA.

NITA, M. & SCHOLZ, D. 2012. Estimating the Oswald Factor from Basic Aircraft Geometrical Parameters. *Deutscher Luft- und Raumfahrtkongress 2012.* Berlin, Germany: German Society for Aeronautics and Astronautics (DGLR).

OAG. 2014. *Worldwide Direct Flights Comprehensive Schedule Data* [Online]. Luton, Bedfordshire, UK. Available: http://www.oag.com/Aviation-Data/Flight-Schedules/OAG-WDF-Data-File [Accessed 27th July 2014].

OSWALD, W. B. 1931. General Formulas and Charts for the Calculation of Airplane Performance. Pasadena, CA, USA: California Institute of Technology.

RANDT, N. P. 2014a. Fuel Burn Comparison of Transport Aircraft. Garching bei München, Germany: Institute of Aircraft Design, Technische Universität München.

RANDT, N. P. 2014b. Propcraft P-420/A Baseline Technical Report. Garching bei München, Germany: Institute of Aircraft Design, Technische Universität München.

RAYMER, D. P. 2012. *Aircraft Design: A Conceptual Approach*, 5th ed., Reston, VA, USA, American Institute of Aeronautics and Astronautics AIAA.

ROSKAM, J. 1990. *Airplane Design Part VI: Preliminary Calculation of Aerodynamic, Thrust and Power Characteristics*, Lawrence, KS, USA, The University of Kansas.

RUDOLPH, P. K. C. 1996. High-Lift Systems on Commercial Subsonic Airliners. Moffett Field, California, USA: National Aeronautics and Space Administration NASA Ames Research Center.

SEITZ, A. 2011. *Advanced Methods for Propulsion System Integration in Aircraft Conceptual Design.* Dissertation, Technische Universität München.

STERZENBACH, R., CONRADY, R. & FICHERT, F. 2009. *Luftverkehr betriebswirtschaftliches Lehr- und Handbuch*, 4., grundlegend überarb. und erw. Aufl., München, Oldenbourg.

THE MATHWORKS INC. 2014. *MATLAB - The language of technical computing* [Online]. Natick, MA, USA. Available: http://www.mathworks.de/products/matlab/ [Accessed 5th August 2014].

TORENBEEK, E. 1982. *Synthesis of Subsonic Airplane Design*, Delft, The Hague, The Netherlands, Delft University Press, Martinus Nijhoff Publishers.

TORENBEEK, E. 2013. *Advanced Aircraft Design*, Chichester, West Sussex, UK, John Wiley & Sons Ltd.

WOLF, W. 2007. *Verkehr - Umwelt - Klima: Die Globalisierung des Tempowahns*, Wien, Austria, Promedia.

ZIMMER, H. 1994. *Luftfahrttechnisches Handbuch: Triebwerkstechnologie*, Ausgabe A, Dornier Luftfahrt GmbH.

Eidesstattliche Versicherung

„Ich versichere, dass ich diese Masterarbeit selbstständig und nur unter Verwendung der angegebenen Hilfsmittel angefertigt und die den benutzten Quellen wörtlich oder inhaltlich entnommenen Stellen als solche kenntlich gemacht habe. Die Arbeit hat in gleicher oder ähnlicher Form noch keiner anderen Prüfungsbehörde vorgelegen."

_____ _____

Ort und Datum Unterschrift

Appendix

A Technical Data of the Baseline Propcraft P-420/A Concept

This appendix contains technical data of the baseline Propcraft P-420/A concept, which are needed as input for the analyses performed in this work.

Table A.1: Geometrical data of the baseline high-capacity short-/medium-range aircraft concept Propcraft P-420/A (Randt 2014b)

Geometry	
Wing area	250 m^2
Wingspan	51.65 m
Wing aspect ratio	10.7
Wing taper ratio	0.24
Wing leading edge sweep	18°
Wing dihedral angle	5°
Wing airfoil	NASA SC(2)-0714
Fuselage length	47.7 m
Fuselage horizontal diameter	5.91 m
Fuselage vertical diameter	6.6 m
Horizontal tail area	70 m^2
Horizontal tail taper ratio	0.46
Horizontal tail leading edge sweep	24°
Horizontal tail airfoil	NACA 0009
Vertical tail area	57.9 m^2
Vertical tail taper ratio	0.24
Vertical tail leading edge sweep	40°
Vertical tail airfoil	NACA 0009

Geometrical data of the aircraft concept are given in Table A.1. The following sections contain further parameters that were estimated by Iwanizki et al. concerning aerodynamics, masses, and propulsion. These data are recalculated and thus updated by this work.

A.1 Aerodynamic Characteristics

Important aspects of the aerodynamics of the aircraft are the lift and drag characteristics in all relevant flight attitudes. Figure A.1 depicts the drag polars of the concept in clean, take-off, and landing configurations. A double-slotted Fowler high-lift-system is considered for take-off and landing settings. Additionally, drag polars with deployed landing gear are shown. Further aerodynamic data that are valid for cruise flight conditions are given in Table A.2.

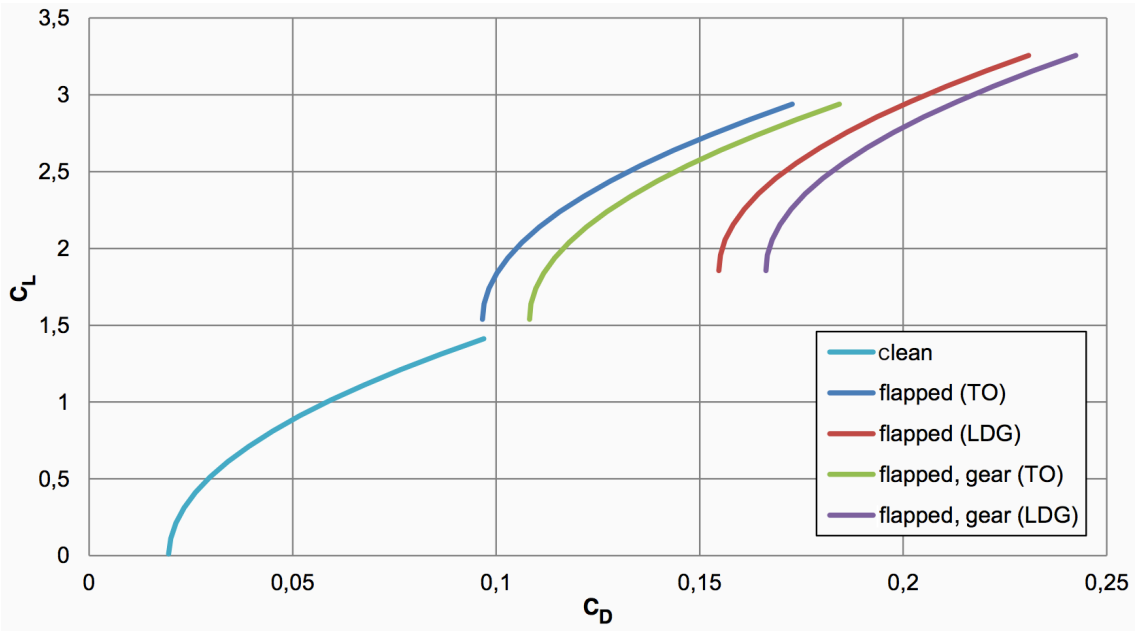

Figure A.1: Drag polars of the baseline high-capacity short-/medium-range aircraft concept Propcraft P-420/A for clean, take-off and landing configurations with landing gear retracted or deployed (Randt 2014b)

Table A.2: Aerodynamics data of the baseline high-capacity short-/medium-range aircraft concept Propcraft P-420/A (Randt 2014b)

Aerodynamics in cruise flight	
Lift-curve slope	5.5778 1/rad
Zero-lift drag	0.01964
Drag due to lift factor	0.03884
Lift to drag ratio	17.54

A.2 Masses and Capacities

Based on a detailed component mass estimation, an operating mass empty of approximately 91 tons was determined. The passengers' mass is accounted for with 100 kg per passenger including luggage. With a capacity of 420 passengers and a maximum of ten tons of cargo, this yields a maximum overall payload mass of 52 tons. Yet, on the design mission only five tons of additional cargo are considered. Together with an estimated mission fuel mass of 27.9 tons (incl. reserves), this sums up to a maximum take-off mass of almost 166 tons that is required to fulfill the design mission. Table A.3 gives an overview of the masses and capacities. A detailed mass breakdown of the aircraft concept's components can be found in Randt (2014b, p.10).

Table A.3: Masses and capacities of the baseline high-capacity short-/medium-range aircraft concept Propcraft P-420/A (Randt 2014b)

Masses and capacities	
Maximum take-off mass	165,840 kg
Operating mass empty	90,940 kg
Maximum fuel capacity incl. reserves	61,417 kg
Design mission fuel	27,900 kg
Maximum and design mission passenger capacity	420 (economy class)
Design mission cargo capacity	5,000 kg
Maximum cargo capacity	10,000 kg
Maximum overall payload capacity	52,000 kg

A.3 Propulsion Characteristics

The propulsion system of the aircraft concept is based on the one of the Antonov An-70. Four turboprop engines with an equivalent shaft power of 9.7 MW each are used. They feature two-rowed counter-rotating propellers of five meters in diameter. Important data of the propulsion system are summarized in Table A.4.

Table A.4: Propulsion data of the baseline high-capacity short-/medium-range aircraft concept Propcraft P-420/A (Randt 2014b)

Propulsion	
Number of engines	4
Equivalent shaft power per engine (static, at MSL)	9,700 kW
Power specific fuel consumption	1.7956 N/kW/h
Propeller diameter	5 m
Number of propeller blades	8 + 6 counter-rotating

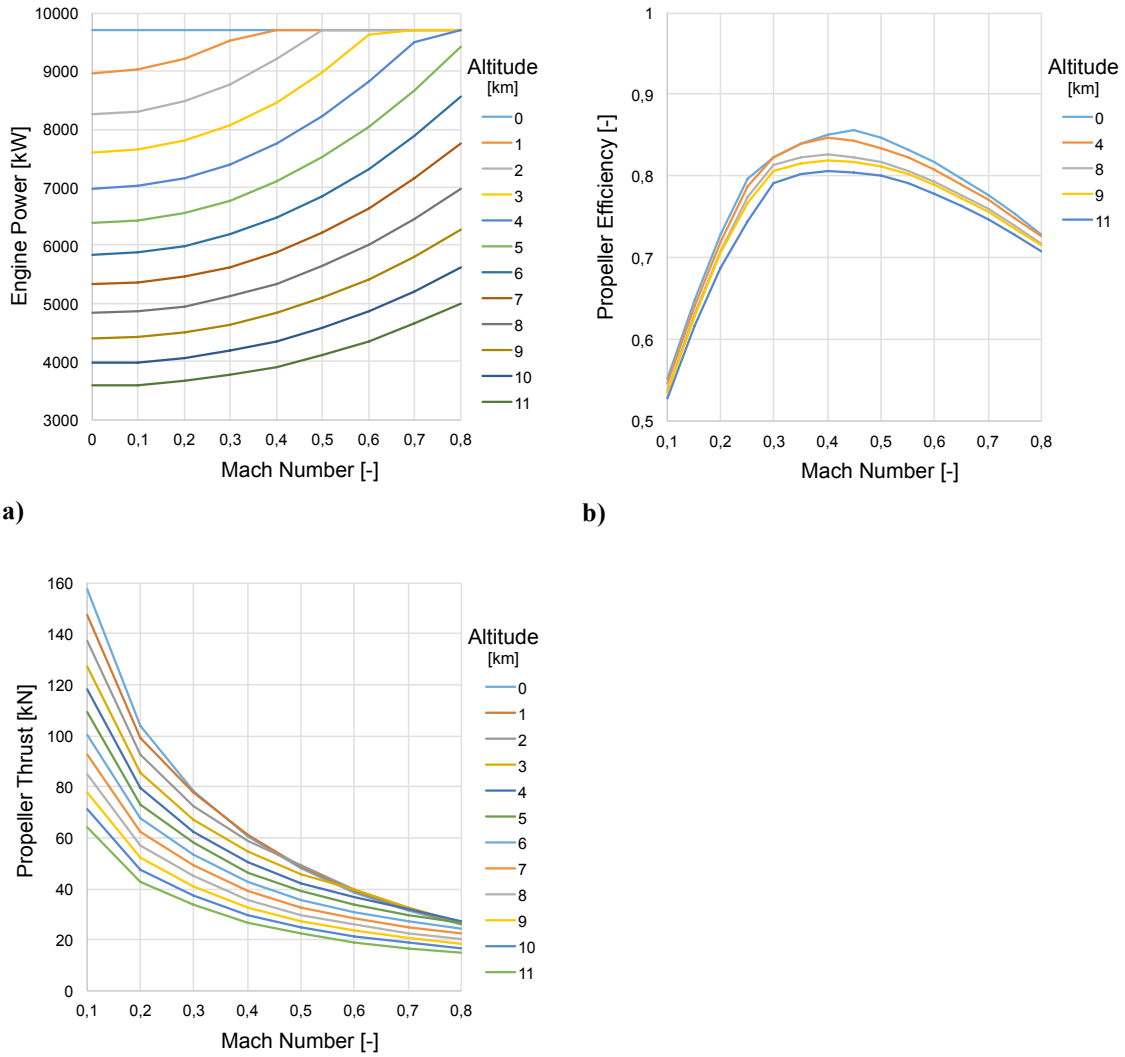

Figure A.2: Propulsion model of the baseline high-capacity short-/medium-range aircraft concept Propcraft P-420/A as a function of flight Mach number and altitude (Randt 2014b), a) model of power per engine, b) propeller efficiency model, c) model of thrust per propeller

In addition to these general data, it is necessary to determine the available thrust throughout the entire operating range of the aircraft. In a three-stage process, the available engine power, the achievable propulsive efficiency of the propeller, and finally the produced thrust have to be estimated. Based on available data of the Allison 501-M7 (T56-A-15) turboprop engine of the Lockheed C-130H Hercules (Nicolai and Carichner 2010, p.803), a model for the equivalent shaft engine power as a function of flight Mach number and altitude was derived as shown in Figure A.2 a). A model for the efficiency of the propeller to convert the engine power into thrust was applied as suggested by Howe (2000, p.68) with corrections after Raymer (2012, p.500). The result is depicted in Figure A.2 b). According to Equation (A.1) the propeller thrust can be calculated

from the available engine power, propeller efficiency and aircraft velocity, see Figure A.2 c).

$$T = \frac{P \cdot \eta}{V} \tag{A.1}$$

Furthermore, fuel consumption of the engines has to be estimated. Based on a data source of the Iwtschenko Progress D-27 engine of the Antonov An-70, the power specific fuel consumption was set to roughly 1.8 N/kW/h, cf. Table A.4. Variation of fuel consumption with flight Mach number and altitude was not considered.

B Required Input Parameters of the Integrated Design Tool

This appendix lists all input parameters required to run the IDT and gives short descriptions where necessary. With this set of parameters a comprehensive definition of the aircraft concept to be investigated is provided.

B.1 General Aircraft Configuration Parameters

The first group of input parameters contains general aircraft parameters as listed in Table B.1. Mainly these are needed for the statistical mass estimation methods and the performance calculation. Operational parameters such as speeds or altitudes of the design mission can also be entered in this section.

Table B.1: General aircraft configuration input parameters of the integrated design tool

General		
Maximum take-off mass	[kg]	Initial estimate, iterative adjustment to desired mass estimation method suggested, cf. Section 3.4
Limit load factor	[-]	In multiples of the gravitational acceleration, standard value for transport category aircraft 2.5 (Howe 2000, p.5)
Maximum passenger capacity	[-]	
Number of passengers on design mission	[-]	
Mass per passenger	[kg]	Mass of one passenger with luggage, typical value 100 kg
Number of crew	[-]	
Maximum cargo capacity	[kg]	
Cargo mass on design mission	[kg]	
Maximum fuel capacity	[kg]	
Mission fuel payload on design mission	[kg]	
Design dive speed	[m/s]	In equivalent airspeed EAS
Estimated maximum range	[km]	With maximum fuel
Maximum working cabin pressure differential	[bar]	Maximum pressure difference between cabin and ambient pressure, based on estimated maximum operating altitude
Design flight Mach number in slow and low flight	[-]	Value is used as reference for aerodynamic analysis of flight shortly after take-off and before landing
Design cruise Mach number	[-]	

Table B.1 – continued

Design cruise altitude		[ft]	
Take-off maximum angle of rotation on runway		[°]	Commonly limited by landing gear length / tail strike
Field length requirement		[m]	Limit for constraint analysis
SEP requirement in cruise flight		[m/s]	Limit for constraint analysis
Design mission parameters	Taxi out time	[min]	
	Airspeed in first part of climb	[m/s]	In calibrated airspeed CAS
	Mach number in second part of climb	[-]	
	Range	[km]	
	Mach number in first part of descent	[-]	
	Airspeed in second part of descent	[m/s]	In calibrated airspeed CAS
	Descent angle	[°]	
	Taxi-in time	[min]	
	Diversion cruise altitude	[ft]	
	Diversion cruise Mach number	[-]	
	Diversion range	[NM]	
	Loiter altitude	[ft]	
	Loiter time	[min]	
	Loiter airspeed	[m/s]	In calibrated airspeed CAS

B.2 Airfoil and Wing Geometric Parameters

The wing geometry is defined through various two-dimensional and three-dimensional parameters, cf. Table B.2. Furthermore, two-dimensional aerodynamic properties of the airfoil are required, as the IDT does not contain a module that can derive airfoil aerodynamics. If these data are not available, it can be determined from an existing airfoil geometry for example with the tool XFOIL (Drela and Youngren 2013).

B.3 Horizontal and Vertical Tail Geometric Parameters

The geometries of horizontal and vertical tail are defined similarly. Hence, the parameters in Table B.3 are needed for both.

Table B.2: Wing geometry input parameters of the integrated design tool

Wing geometry			
Reference area		[m^2]	
Wingspan		[m]	
Relative spanwise position of inner kink (‘kink1’)		[-]	Inner kink represents separation of inner and outer flap segment
Relative spanwise position of outer kink (‘kink2’)		[-]	Outer kink represents separation of outer flap segment and aileron
Taper ratio at inner kink		[-]	
Taper ratio at outer kink		[-]	
Taper ratio at wing tip		[-]	
Leading-edge wing sweep on inboard wing segment		[°]	Inboard wing segment from root to inner king
Leading-edge wing sweep on mid-board wing segment		[°]	Midboard wing segment from inner to outer king
Leading-edge wing sweep on out-board wing segment		[°]	Outboard wing segment from outer kink to wing tip
Dihedral angle		[°]	
Longitudinal position of wing apex		[m]	Referenced to aircraft nose
Relative chord length of aileron		[-]	Ailerons with const. relative chord length from outer kink to wing tip
Relative chord length of flaps at wing root, inner and outer kink		[-]	Flaps from root to outer kink
Relative chord length of slats		[-]	Slats with constant relative chord length over entire wingspan
Airfoil parameters	Relative chordwise position of maximum thickness	[-]	
	Thickness to chord length ratio	[-]	
	Design lift coefficient	[-]	
	Lift-curve slope in slow and low flight	[1/rad]	E.g., determinable with XFOIL
	Lift-curve slope in cruise flight	[1/rad]	E.g., determinable with XFOIL
	Maximum lift at slow and low flight	[-]	E.g., determinable with XFOIL
	Zero-lift angle of attack in slow and low flight	[-]	E.g., determinable with XFOIL
	Zero-lift angle of attack in cruise flight	[-]	E.g., determinable with XFOIL
	Subsonic maximum lift ratio for high-aspect-ratio wings	[-]	Graphically derivable from Raymer (2012, p.419) Fig. 12.9

Table B.2 – continued

Airfoil parameters	Mach correction for subsonic maximum lift of high-aspect-ratio wings in slow and low flight	[-]	Graphically derivable from Raymer (2012, p.420) Fig. 12.10
	Mach correction for subsonic maximum lift of high-aspect-ratio wings in cruise flight	[-]	Graphically derivable from Raymer (2012, p.420) Fig. 12.10
	Angle-of-attack increment for subsonic maximum lift of high-aspect-ratio wings	[°]	Graphically derivable from Raymer (2012, p.421) Fig. 12.11

Table B.3: Empennage geometry input parameters of the integrated design tool

Empennage geometry		
Tailplane reference area	[m^2]	
Span	[m]	
Taper ratio	[-]	
Leading edge sweep	[°]	
Longitudinal position of wing apex	[m]	Referenced to aircraft nose
Thickness to chord length ratio	[-]	
Relative chordwise position of maximum thickness	[-]	
Relative chord length of elevator or rudder respectively	[-]	With constant relative chord length over entire span

B.4 Fuselage Geometric Parameters

As only the basic shape of the fuselage is modeled, just a few parameters are required to describe it. They are listed in Table B.4.

Table B.4: Fuselage geometry input parameters of the integrated design tool

Fuselage geometry		
Horizontal diameter	[m]	
Vertical diameter	[m]	
Length	[m]	
Nose length	[m]	From nose to position where full fuselage diameter is reached
Tail length	[m]	From most rearward position with full fuselage diameter to rear
Tail upsweep of fuselage centerline	[°]	

B.5 Landing Gear Parameters

A detailed design of the landing gear is usually not yet available in the conceptual or preliminary design phase. However, the landing gear contributes a significant part to the aircraft's operating mass empty and causes a considerable increase in aircraft drag if it is deployed. (Torenbeek 1982, p.342; Raymer 2012, p.442) Hence, a rudimentary sizing is needed for reasonably accurate estimations of mass and drag, cf. Table B.5.

Table B.5: Landing gear input parameters of the integrated design tool

Landing gear	
Nose gear length	[m]
Number of wheels on nose gear	[-]
Main gear length	[m]
Number of struts of main gear	[-]
Number of wheels per strut of main gear	[-]

B.6 Cabin Parameters

In order to enable a rough estimation of the masses of cabin furnishings and equipment, an approximate cabin sizing should be provided. Required parameters are assembled in Table B.6.

B.7 Propulsion System Parameters

The last group of input parameters addresses the propulsion. As mentioned in Section 3.1.2, the IDT comprises a turboprop engine model. Table B.7 contains the corresponding parameters.

Table B.6: Cabin configuration input parameters of the integrated design tool

Cabin configuration		
Horizontal diameter	[m]	
Vertical diameter	[m]	
Length	[m]	
Nose length	[m]	From nose to position where full fuselage diameter is reached
Tail length	[m]	From most rearward position with full fuselage diameter to rear
Tail upsweep of fuselage centerline	[°]	

Table B.7: Propulsion system input parameters of the integrated design tool

Propulsion system		
Equivalent shaft power rating	[kW]	Per engine, static, at MSL
Maximum static thrust	[kN]	Initial estimate, iterative adjustment suggested, per engine
Nacelle length	[m]	
Nacelle horizontal width	[m]	
Uninstalled engine mass	[kg]	
Number of engines	[-]	
Number of engines mounted over the wing	[-]	
Fuel density	[kg/l]	
Number of fuel tanks	[-]	
Number of propellers	[-]	If applicable higher than number of engines because of counter-rotating configuration
Propeller diameter	[m]	
Number of blades per propeller	[-]	If applicable average value of first and second row of counter-rotating propellers
Relative spanwise position of inner engines	[-]	
Relative spanwise position of outer engines	[-]	

C Group Weight Statements of the Baseline Propcraft P-420/A Concept as predicted with the different Mass Estimation Methods

In this appendix, the detailed results of the component mass predictions of the baseline Propcraft P-420/A concept are tabulated as group weight statements.

C.1 Mass Prediction after Raymer

Table C.1: Group weight statement of the baseline Propcraft P-420/A concept as predicted with the method after Raymer

Component or group	Fudge factor advanced composites – where applicable –	Predicted mass in kg
Structures:		**35,396**
Wing	0.85	11,674
Horizontal tail	0.83	1,360
Vertical tail	0.83	1,311
Fuselage	0.9	10,550
Main landing gear	0.95	7,413
Nose landing gear	0.95	742
Nacelle group (all engines)	0.9	2,346
Propulsion:		**11,395**
Engines		10,862
Engine controls		89
Starter		103
Fuel system		342
Systems:		**11,225**
Flight controls		936
APU		440
Instruments		407
Hydraulics		165
Electrical system		607
Avionics		971
Furnishings		5,613
Air conditioning		1,771
Anti-icing		274
Load and handling gear		41
Empty weight allowance		**2,901**
Operating mass empty:		**60,917**

C.2 Detailed Mass Prediction after Torenbeek (1982)

Table C.2: Group weight statement of the baseline Propcraft P-420/A concept as predicted with the 'detailed' method after Torenbeek (1982)

Component or group	Fudge factor advanced composites – where applicable –	Predicted mass in kg
Structures:		**44,148**
Wing	0.85	13,486
Horizontal tail	0.83	1,229
Vertical tail	0.83	917
Fuselage	0.9	16,027
Main landing gear	0.95	5,691
Nose landing gear	0.95	869
Surface controls	0.85	1,785
Nacelle group (all engines)	0.9	4,144
Propulsion:		**22,373**
Engines		7,600
Gear boxes, controls, starter		1,416
Oil system and cooler		532
Fuel system		537
Propeller installation		12,288
Systems:		**24,289**
APU		376
Instruments, nav, electronics		2,084
Hydraulics and pneumatics		1,717
Electrical system		2,174
Furnishings		16,709
Fligh deck accommodations		240
Passenger and attendants seats		4,252
Galleys		227
Toilets		1,088
Floor covering		743
Wall covering, ceiling etc.		8,665
Cargo restraints, handling		313
Oxygen system		476
Fire detection, extinguishing		517
Escape provisions		190
Air condition and anti-ice		1,230

Table C.2 – continued

Miscellaneous (e.g., paint)	**963**
Operational items:	**5,531**
Crew and provisions	730
Passenger cabin supplies	2,667
Water and toilet chemicals	435
Safety equipment	1,428
Residual fuel and oil	271
Operating mass empty:	**97,305**

C.3 Detailed Mass Prediction after Howe

Table C.3: Group weight statement of the baseline Propcraft P-420/A concept as predicted with the 'detailed' method after Howe

Component or group	Fudge factor advanced composites – where applicable –	Predicted mass in kg
Structures:		**34,316**
Wing	0.85	10,153
Horizontal empennage	0.83	1,115
Vertical empennage	0.83	846
Fuselage	0.9	10,550
Landing gear	0.95	5,763
Propulsion:		**21,196**
Installed (single) powerplant		5,299
Systems:		**22,542**
Flight controls and hydraulics		3,193
Electrical system, instruments, avionics		3,991
Air conditioning, pressurization, oxygen		1,800
De-icing system		958
Furnishings		12,600
Miscellaneous (e.g., paint)		**798**
Operational items (e.g., crew)		**5,890**
Operating mass empty:		**60,917**